

In-source laser spectroscopy of At isotopes and decay studies of ^{178}Au

James Gerald Cubiss

Doctor of Philosophy

University of York
Physics

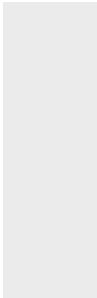
May 2017

Abstract

The region surrounding the $Z = 82$ major-shell closure has exhibited the strongest known manifestation of shape coexistence, to date. Due to this, the nuclides that inhabit this region have been subject to extensive decay- and laser-spectroscopy studies. In this work, the results from two investigations performed at the CERN, ISOLDE facility will be presented: the first, an α -decay study of two states in ^{178}Au , and the second, an in-source laser-spectroscopy experiment performed on a long chain of At isotopes.

Two states, a low-spin ground state, and a high-spin isomer, were directly identified in ^{178}Au ($Z = 79$, $N = 99$) for the first time. Due to the highly selective resonant laser-ionisation method, it was possible to produce isomerically pure beams of the ground and isomeric states. These beams were then utilised in order to perform dedicated α -decay studies upon the two states. Successful measurements were made for the half-lives, branching ratios, and decay patterns of $^{178g,m}\text{Au}$.

The first ever laser-spectroscopy measurements were performed on a long chain of At isotopes, using the in-source resonant ionisation technique. The isotope shifts and hyperfine structures of long-lived states in $^{195-211,217-219}\text{At}$ were measured. From these, values for the corresponding changes in mean-squared charge radius, and magnetic dipole moments were extracted. The charge-radii of the neutron-deficient At isotopes display a strong onset of deformation, as the neutron number approaches the $N = 104$ midshell. The observed onset is more pronounced than the one seen in the Po isotopes, which is noted to be exceptionally strong. Based on the extracted charge-radii and magnetic moments, cases for shape coexistence were identified in $^{195,197,199}\text{At}$. In the case of the neutron-rich At isotopes, an inversion of the normal odd-even-staggering has given evidence for the presence of octupole collectivity.



Contents

Abstract	2
Contents	3
List of Figures	6
List of Tables	9
Acknowledgements	11
Author Declaration	13
1 Introduction	14
1.1 Previous work for decay study of ^{178}Au	18
1.2 Previous work for charge-radii study of At isotopes	19
2 Theoretical considerations	22
2.1 Nuclear models	22
2.1.1 The spherical liquid drop model	22
2.1.2 The spherical shell model	25
2.1.3 The deformed shell model	29
2.2 Low-energy shape coexistence	33
2.2.1 Intruder states	36
2.3 Probing the structure of the nucleus	38
2.3.1 Alpha decay	38
2.3.2 Beta decay	41
2.3.3 Gamma decay	42
3 Laser spectroscopy	45
3.1 Isotope and isomer shifts	45

3.2	The hyperfine structure	47
3.2.1	Magnetic dipole moment	48
3.2.2	Electric quadrupole	48
4	Experimental method	49
4.1	ISOLDE facility	50
4.2	Radioactive beam production	51
4.2.1	RILIS	53
4.2.2	Mass Separation	55
4.3	The windmill decay station	56
4.3.1	Electronics and data acquisition	57
4.4	Scanning the hyperfine structure	58
4.4.1	The ISOLTRAP MR-ToF device	60
5	Decay studies of ^{178}Au	61
5.1	Identification and separation of different isomers	61
5.2	Calibration of detectors	62
5.2.1	Silicon detectors	62
5.2.2	Germanium detectors	64
5.2.3	Prompt timing gates	64
5.3	Decay analysis	66
5.3.1	Singles alpha decay	66
5.3.2	Alpha-decay intensities	76
5.4	Decay branching ratios	81
5.5	Half-lives	82
5.5.1	Reduced widths and hindrance factors for alpha decays	84
5.6	The 5521 keV and 5571 keV alpha decays of the isomeric state	84
5.7	Spin assignments for $^{178g,m}\text{Au}$	87
5.8	Configuration assignments for the ground and isomeric states in ^{178}Au and ^{174}Ir	88
6	Laser spectroscopy studies of At isotopes	92
6.1	Nuclear structure of At isotopes	93
6.2	Extraction of hyperfine structure from windmill data	96
6.3	Fitting of HFS data	99
6.4	Changes in charge-radii and deformation across the At isotopic chain	102
6.4.1	The ground states of the neutron-deficient ($N \leq 126$) At isotopes	105
6.4.2	Cases for shape coexistence in the light At isotopes	106
6.4.3	Odd-even staggering	107

6.5	Magnetic dipole moments	109
6.5.1	Even- N isotopes	112
6.5.2	Odd- N isotopes	114
7	Conclusion	117
7.1	Future work	118
	References	120

List of Figures

1.1	Ground-state quadrupole deformations for nuclei with $N < 200$	14
1.3	Level scheme for ^{16}O	16
1.2	The region of the nuclear Segrè chart surrounding the $Z = 82$ shell closure	17
1.4	Change in mean-squared charge radii of Au isotopes	19
1.5	Change in mean-squared charge radii for chains of isotopes in the lead region	20
2.1	Binding energy per nucleon as a function of mass number	23
2.2	Density distribution of nuclear matter as a function of radius	24
2.3	The forms of the Woods-Saxon, spin-orbit, Coulomb and centrifugal (pink) terms of Equation 2.1.2, and their combined effects	27
2.4	Single-particle state energy levels for neutrons in a ^{208}Pb nucleus	28
2.5	Schematic representation of spheroidal geometries as a function of the quadrupole deformation parameter, β_2	29
2.6	Nilsson model single-particle energies for protons in nuclei with $Z > 82$.	31
2.7	Nilsson model single-particle energies for neutrons in nuclei with $82 < N < 126$	32
2.8	Binding energy of the ammonia molecule	33
2.9	Change in mean-square charge radii of the Hg isotopic chain	34
2.10	Potential energy surface of the ground-state energies of $^{184,185,186}\text{Hg}$. . .	35
2.11	A schematic drawing of the impact of the individual terms upon the unperturbed energy of an intruder state	37
2.12	A schematic of an α particle in a one-dimensional square well potential .	40
4.1	A schematic representation of the CERN accelerator complex	49
4.2	A three-dimensional computer model of the ISOLDE facility	50
4.3	Schematic overview of the in-source resonance ionisation spectroscopy setup for the experiment on At beams	51

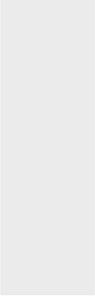
4.4	Schematic of the spallation, fragmentation and fission reactions	52
4.5	The three-step resonant ionisation schemes used to produce the Au and At beams	54
4.6	Three-dimensional model of the detectors used in the Windmill decay station	56
4.7	Surface plot of the α -decay energy measured in the Windmill system, versus the laser wavenumber	59
4.8	Surface plot of the α -decay energy measured in the Windmill system, versus the laser wavenumber	60
5.1	The measured HFS of the ground and isomeric states of ^{178}Au	62
5.2	Energy calibration for the Si1 and Si2 detectors	63
5.3	The solid angle coverage of Si1 and Si2	63
5.4	The difference between the time of detection for an α particle and a γ ray belonging to the 5291-158.6 keV fine-structure decay of ^{178}Pt	64
5.5	Calibration of the germanium detector	65
5.6	Singles α -decay and α - γ coincidence spectra for ^{178g}Au , and ^{178m}Au . . .	67
5.7	Projections on the E_α axis from the α - γ coincidence matrix of ^{178g}Au . . .	69
5.8	Decay scheme for the ground and isomeric state in ^{178}Au , deduced in this work	71
5.9	The two possible options for placing the 98.2 keV γ -ray transition	72
5.10	Projections on the E_α axis from the α - γ coincidence matrix of ^{178m}Au . .	74
5.11	The ^{178}Au ground and isomeric states singles α -decay spectra, fitted with crystal ball functions	77
5.12	Spatial distribution of 10^7 events initialised in the GEANT4 simulations. .	78
5.13	Geant4 simulations for the α -e summing between the 5925 keV α decay and electrons and/or L x rays, due to the converted 56.8 keV γ transition .	80
5.14	The singles α spectrum of the experimental data overlapped with the results from the GEANT4 simulation	81
5.15	Comparison of the data taken for half life measurements of ^{178g}Au , before and after the dead time correction	83
5.16	The extracted decay curves for the ground and isomeric states in ^{178}Au . .	83
5.17	Spectrum for the results of GEANT4 simulations for α -e summing in the silicon detectors, between a 5521 keV α particle and a 396 keV conversion electron, with $\alpha_c = 2.0$	86
5.18	Background subtracted singles γ -ray spectra for the ground and isomeric states in ^{178}Au	87

5.19	Single-particle energies for neutron and proton Nilsson orbitals, in the regions pertinent to ^{178}Au ($Z = 79, N = 99$)	90
6.1	Energies of the $I = 9/2, 1/2, 7/2$ and $13/2$ states in the odd-mass At isotopes	94
6.2	The three-step photoionisation scheme used to ionise At atoms during the experiment, and the hyperfine splitting of the atomic levels due to the coupling of the nuclear and atomic electron spins	95
6.3	Simulation of the expected HFS measured for the hyperfine splitting shown in Fig. 6.2	96
6.4	The singles α -decay spectra and the HFS for At isotopes measured using the Windmill decay station	98
6.5	The singles γ -ray spectrum and extracted HFS for the $I = 1/2$ state in ^{199}At	100
6.6	Fitting of HFS spectra for the ^{197}At $I = 1/2$ and $I = 9/2$ states using the York routine	101
6.7	Change in mean-square charge radii for At isotopic chain relative to ^{211}At ($N = 126$), as a function of neutron number	104
6.8	Ground and isomeric state quadrupole deformation parameters as a function of neutron number for the light At isotopes	105
6.9	Comparison of the change in mean-squared charge radii relative to that of the $N = 126$ isotopes, for the At, Po and Pb isotopic chains	106
6.10	Comparison of values of the odd-even staggering parameter	108
6.11	The magnetic moments of the different states in the At isotopes, as a function of neutron number.	112
6.12	The values of μ for the $I = 9/2$ states in the At isotopes	113
6.13	Comparison of the magnetic-dipole moment for the $I = 1/2$ states in At, Tl, and Bi isotopic chains.	114
6.14	Magnetic moments for the odd- N At nuclei (red circles) along with their Bi and Fr isotones.	115

List of Tables

2.1	Weisskopf estimates for the single-particle γ -transition half-lives	43
5.1	Energies for α decays (E_α) and γ transitions (E_γ) in coincidence with one another and the calculated total Q-values ($Q_{\alpha,tot}$), for ^{178g}Au	68
5.2	Energies for α decays (E_α) and γ transitions (E_γ) in coincidence with one another and the calculated total Q values ($Q_{\alpha,tot}$), for ^{178m}Au	76
5.3	Average energies (E_{ce}) and conversion coefficients (α_c) for conversion electrons competing with a 56.8 keV, M1 γ transition, calculated using BrIcc	78
5.4	Reduced α -decay widths for the main peaks seen in the singles spectrum; intensities taken from integrating the number of counts underneath the 5521 and 5571 keV peaks (left), or from the integral of the individual components of the crystal ball fits shown in Fig. 5.11 (right).	84
5.5	Theoretical $\alpha_{c,tot}$ values for 421.4 and 471.2 keV γ -ray transitions of different multipolarities in Ir	85
5.6	The possible configurations for the odd proton and neutron states in $^{178g,m}\text{Au}$, in accordance with the Gallagher-Moszkowski (GM) angular-momenta coupling rules, and their corresponding spherical shell model orbitals.	91
6.1	The α -decay energies that were gated on to select specific states of the At isotopes investigated using the Windmill setup. The spin assignment for ^{218}At from the analysis of the decay data taken during this run, the results of which are currently unpublished.	97
6.2	Comparison of the York and the Seliverstov-Barazakh fitting routines for the a and b hyperfine parameters of, and the isomer shift, $\delta\nu$, between the $I = 1/2$ and $9/2$ states in ^{197}At	101

6.3	Tabulated data for the measured isotope shifts, $\delta\nu_{A,211}$ and calculated values for $\delta\langle r^2 \rangle_{A,211}$, and the respective $\langle \beta_2^2 \rangle^{1/2}$ parameters when compared to the droplet model	103
6.4	The hyperfine parameters a , extracted from fitting the HFS, and the respective magnetic moments for the At nuclei	111
6.5	Configuration assignments for the $I = 3, 6, 7$ and 10 states in the odd- N At isotopes.	115
6.6	Possible configurations for $I = 2$ state in ^{218}At	116



Acknowledgements

Over the course of my studies it has been my good fortune to have the pleasure of meeting, and working with a number of people, many of whom I would now count as close friends. There are many to thank, but there are some for whom a special mention is needed.

Andrei, for your guidance, advice and enthusiasm throughout my studies, and for the opportunities you have presented me with. Through the experiments, conference and graduate schools you have sent me on I have managed to see much of the world, make new friends, and learn much. Your work ethic and approach to the job has been an inspiration, and I look forward to working with you into the future – that is if you don't mind me hanging round a little longer!

Anatoly and Maxim at PNPI, without the two of you the chapter on the At isotopes would not have been possible. I am especially indebted to you, Anatoly, your feedback and discussions have been most informative, thank you for affording me your time.

Celine, Lars and Victoria, thank you for introducing me to the many glories and idiosyncrasies of the Windmill decay station.

To everyone else at IKS Leuven for their hospitality during my many visits. In particular Mark and Piet, for their guidance on the decay-spectroscopy analysis. A special mention should also go to Thomas, for your lively discussions, and for showing and driving myself and the others around Geneva.

To everyone I have worked with at ISOLDE, in particular Boris, and the RILIS and ISOLTRAP groups. Without all of you the many experiments performed over the past few years would not have been possible. You have been fantastic collaborators – it has been a pleasure working with all of you.

To the members of the nuclear physics group at York, who have been more than happy to help me with any questions I have had, or to share with me a sunny evening in a beer garden. Special mentions need making for Paul and Ale: Paul, for helping me throughout my studies, and for your inspirational quotes such as “Have you tried being better?”. Ale, for always having an open office door and finding the time to

discuss physics with me.

Simon, I think trying to claim that we have worked together would be a lie – there has been far too much fun (and beers)! I hope we can continue this “professional” relationship into the future...and maybe for a few more beers!

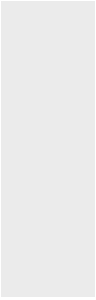
Gemma, for being a great friend, and for helping me out throughout my entire Ph.D. Especially for proofreading the entire thesis in a few days, even though you were moving your life across the U.S.A!

Jos and Ruchi, for being the best office mates. Jess and Adelle, for making me laugh/wince/speechless. Lianne, Jack and Tom, for coffee breaks and the pub.

Natalie, for your seemingly endless patience and understanding. You reminded me there is a world outside of physics. To my family, for your continued support throughout the better part of the past decade.

I fear there will be some names that I have missed, for which I apologise – but I will finish by saying a big thank you to everyone that I have met and worked with over the past few years. It has been a lot of hard work, and a lot of fun!

A handwritten signature in black ink that reads "James". The signature is written in a cursive, flowing style with a large initial 'J'.



Author Declaration

I declare that this thesis is a presentation of original work and I am the sole author. This work has not previously been presented for an award at this, or any other, University. All sources are acknowledged as References.

Introduction

The shape of a nucleus is an important feature of its structure. It defines the potential that binds its constituent nucleons, the states that can exist within such a potential, as well as the half-lives and decay modes of those states. Although the nuclear Hamiltonian is rotationally invariant, the majority of nuclei are non-spherical in their intrinsic frame-of-reference. Nuclei with a magic number of protons or neutrons are spherical, with rare exceptions such as the “island of inversion” surrounding ^{32}Mg [1, 2, 3]. However, most nuclei are non-magic and are deformed spheroids of a quadrupole nature, as shown in Fig. 1.1 [4]. Recently, more exotic shapes have been discovered, with ^{224}Ra observed to possess an octupole, or ‘pear-shaped’ nucleus [5].

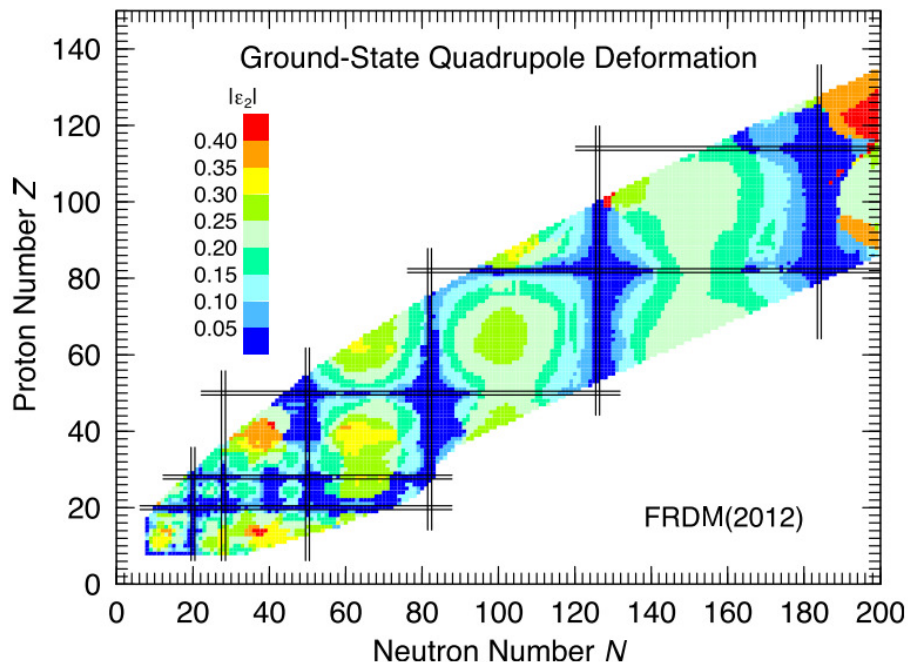


Figure 1.1: Ground-state quadrupole deformations for nuclei with $N < 200$. The black lines show the proton and neutron major-shell closures. Figure taken from [4].

Another key phenomenon related to nuclear deformation is the ability for different states within a single atomic nucleus to exist at low energies, but possess distinctly different shapes. This behaviour, known as shape coexistence, appears to be unique to the atomic nucleus, with no other finite many-body quantum system displaying such a phenomenon.

A pleasing analogy for these shape phenomena can be found in a ‘fruit basket’ of nuclear shapes, as shown in Fig 1.2. The figure shows a section of the Segrè chart in the vicinity of the $Z = 82$ and $N = 126$ major-shell closures. The shapes of nuclei in the different regions of the chart are expected to be similar to the fruits positioned above them. The orange, positioned above the $N = 126$ shell closure, represents nuclei with spherical shapes. The grape and the aptly-named squash represent the quadrupole-deformed prolate and oblate geometries, respectively. The three, differently-shaped tomatoes are representative of shape coexistence, which should be most prolific in midshell regions. The pear, is of course the ‘pear-shaped’, octupole-deformed nuclei, expected to be found in regions just above a double shell closure.

The first observation of shape coexistence was made over 60 years ago by Haruhiko Morinaga [6] in the doubly-magic nucleus ^{16}O . Here, the 0^+ ground state represents a doubly-closed shell configuration and has a spherical shape, on top of which single-particle, single-hole (1p-1h) excitations are built (see Fig. 1.3). The first excited state, also a 0^+ spin-parity state, has a different band structure built on top of it. The states in this band are connected by strong $E2$ γ -ray transitions, and the energy spacings between the states have ratios similar to what would be expected from a rigid-rotor system. This rotational band cannot be produced by a spherical nucleus; a sphere cannot be rotated in the framework of quantum mechanics. Therefore the states in this band must be the product of a deformed system.

Over the past 60 years, shape coexistence has developed from being seen as a rarity that only occurs in a few nuclei, to a phenomenon expected to exist in select islands of the nuclear landscape. Today, the accepted position is that shape coexistence most likely occurs in all but the lightest of atomic nuclei [7]. Over this period the theories that describe this behaviour have become ever more sophisticated, and the wealth of experimental data has increased.

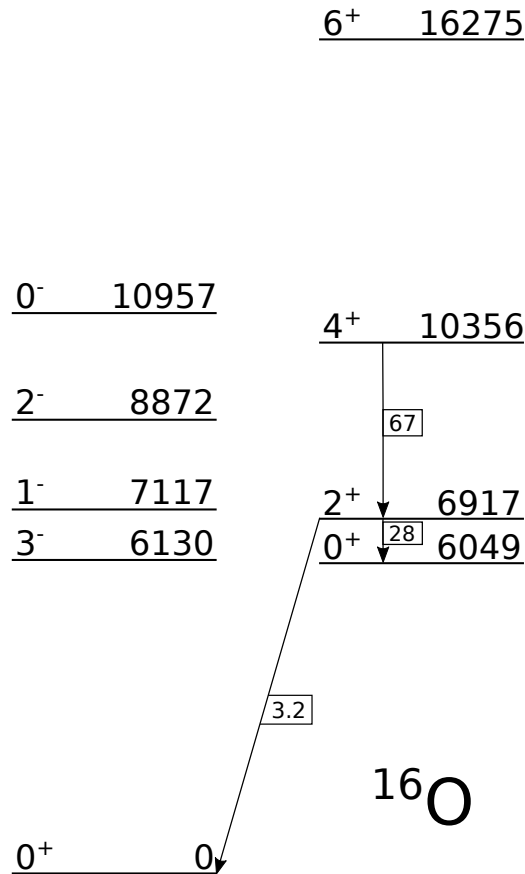


Figure 1.3: Level scheme for ^{16}O . The arrows indicate E2-type γ -ray transitions and the numbers in the square boxes are the respective $B(E2)$ transition strengths, in Weisskopf units. Image adapted from [8], which uses data from [9]. The structure shown on the left is believed to be due to non-deformed, 1p-1h excitations. The structure on the right is the rotational band built on top of the deformed 0_2^+ bandhead.

The work presented in this thesis represents part of a systematic study of nuclear deformation, shape coexistence and decay studies in isotopes surrounding the $Z = 82$ shell closure. To date, this region has displayed the most prolific manifestation of shape coexistence. The IS534 experiment, performed at the ISOLDE facility, began in 2012 and implements the decay-tagged in-source laser spectroscopy technique. The aim of the experiment was to measure the hyperfine structures and the decay properties of ground and isomeric states in the At and Au isotopic chains. This thesis will present the results from the hyperfine structure measurements of At isotopes that took place in 2014, and a dedicated decay study of the ground and isomeric states in ^{178}Au that was performed in 2015.

1.1 Previous work for decay study of ^{178}Au

=Alpha-decay studies have proven a useful tool for probing shape coexistence in the lead region. Alpha decay is sensitive to the overlap between the wavefunctions of initial and final states involved in the process. This results in strong, unhindered decays between states of similar structure and same spin, whereas those between dissimilar states are weak, or in the extreme, impossible. As well as the sensitivity to the underlying structure, α decay has a strong Q -value dependence and often populates low-lying and bandhead states that are often missed in in-beam studies due to out-of-band γ -ray transitions. Therefore, α -decay studies have proven a useful, complementary method to in-beam investigations.

The isotope ^{178}Au lies in an interesting region of evolving nuclear structure. Previous measurements have shown a significant jump in mean-squared charge radius as the neutron number approaches the $N = 104$ midshell (see Fig. 1.4). This jump is believed to be due to a reordering of states, with the ground-state configuration changing from the normal spherical-shell $\pi 2d_{3/2}$ orbital, to that of a $\pi 1h_{9/2}$ intruder configuration. It is predicted that the mean-squared radii of the Au nuclei will return to a spherical trend in the lighter Au isotopes. As shown in Fig. 1.4, ^{178}Au lies where this return to sphericity is predicted to occur.

Previous in-beam and α -decay studies have shown that the return to sphericity could occur in ^{179}Au , which has a $I^\pi = (1/2^+)$ ground state. This indicates a return to a spherical $\pi 2d_{3/2}$ or $\pi 3s_{1/2}$ configuration. This is supported by results from the IS534 experiment, which measured the charge radii for Au isotopes, and showed that the $^{176,177,179}\text{Au}$ nuclei return to a near-spherical shape. However, ^{178}Au was observed to display a second jump in mean-squared charge radius, suggesting that a strong competition exists between deformed and spherical structures in this region.

The first investigation into the decay of ^{178}Au was made by Siivola *et al.* [11], in which the $^{175}\text{Lu}(^{16}\text{O}, xn)^{191-x}\text{Au}$, $^{169}\text{Tm}(^{20}\text{Ne}, xn)^{189-x}\text{Au}$ and $^{168}\text{Yb}(^{19}\text{F}, xn)^{187-x}\text{Au}$ reactions were studied. A single α -decay line with an energy of 5920 keV was attributed to the decay of ^{178}Au . A second study was performed by Keller *et al.* in 1986 [12], which used thin targets of ^{89}Y , $^{90,92,96}\text{Zr}$ and ^{94}Mo , upon which a ^{90}Zr beam was impinged. Here, three α decays of energies $E_\alpha = 5850, 5920$ and 5980 keV were assigned to belong to the α -decay fine structure of a single state. Both studies suffered from contaminants in their singles α -decay spectra due to activity from the products of other, stronger reaction channels.

The first suggestion of the presence of an isomeric state in ^{178}Au came in 1999, when a study of non-yrast states in light Pt isotopes populated by the β decay of Au nuclei was conducted by Davidson *et al.* [13]. The results showed strong feeding

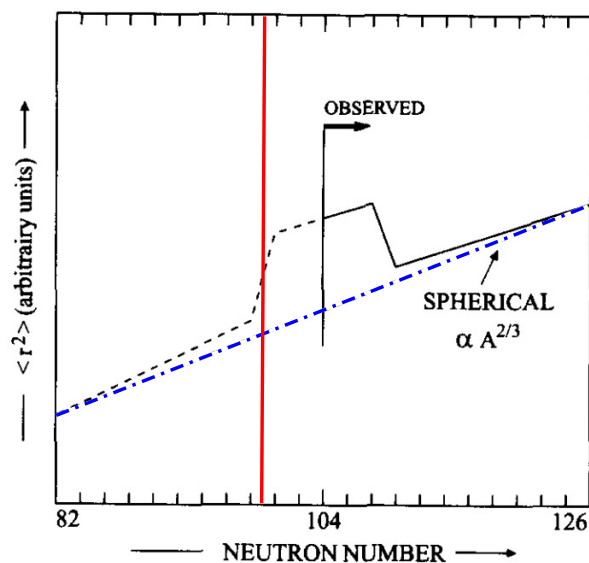


Figure 1.4: Change in mean-squared charge radii of Au isotopes. The blue dot-dashed line indicates the trend that would be taken by spherical, droplet-like nuclei. The solid black line represents the measured radii as of 1999, and the dashed black line is the expected behaviour for the light Au nuclei. The vertical red line indicates where ^{178}Au lies. Figure adapted from [10].

from the β decay of the Au parent to $I = 2$ and 4 states in the Pt daughter nuclei $^{176,178,180,182}\text{Pt}$. In addition, there was considerable side feeding to $I = 8$ states in $^{176,178}\text{Pt}$ (see Figs. 5 and 7 in Ref. [13]). These observations provided the first indication for the presence of two β -decaying states in $^{176,178}\text{Au}$, one with $I \approx 2$ and the other with $I \approx 8$.

The results presented in Chapter 5 are the first instance of the identification and decay study of the two α -decaying states in ^{178}Au . The resonant laser ionisation technique employed at the CERN-ISOLDE facility provides a highly-selective method for producing ion beams. Due to this, it was possible to produce isomerically-pure beams, allowing independent α -decay studies to be made on the ground and isomeric states of ^{178}Au .

1.2 Previous work for charge-radii study of At isotopes

Laser spectroscopy is an effective method for performing systematic studies of nuclear properties across the nuclear chart. Measurements of the hyperfine structures and isotope/isomer shifts are made by varying the light from a laser across a range of frequencies and observing the ionisation efficiency. From the results, one can determine spins and nuclear moments of ground and isomeric states of nuclei

belonging to an isotopic chain, and how the mean-squared charge radii of these states differ between different isotopes and isomers.

Figure 1.5 gives an overview of in-source laser spectroscopy measurements of the changes in mean-squared charge radii, performed in the $Z = 82$ region, as of 2011. Decay-tagged in-source laser spectroscopy combines the high efficiency of in-source laser ionisation with the high sensitivity of decay spectroscopy. This makes it possible to perform measurements on short-lived nuclei far from stability. To date, the highest sensitivity achieved was in the measurement of the hyperfine structure and isotope shift of ^{191}Po ($t_{1/2} < 93$ ms), produced with a minute implantation rate of 0.01 ions/second [14].

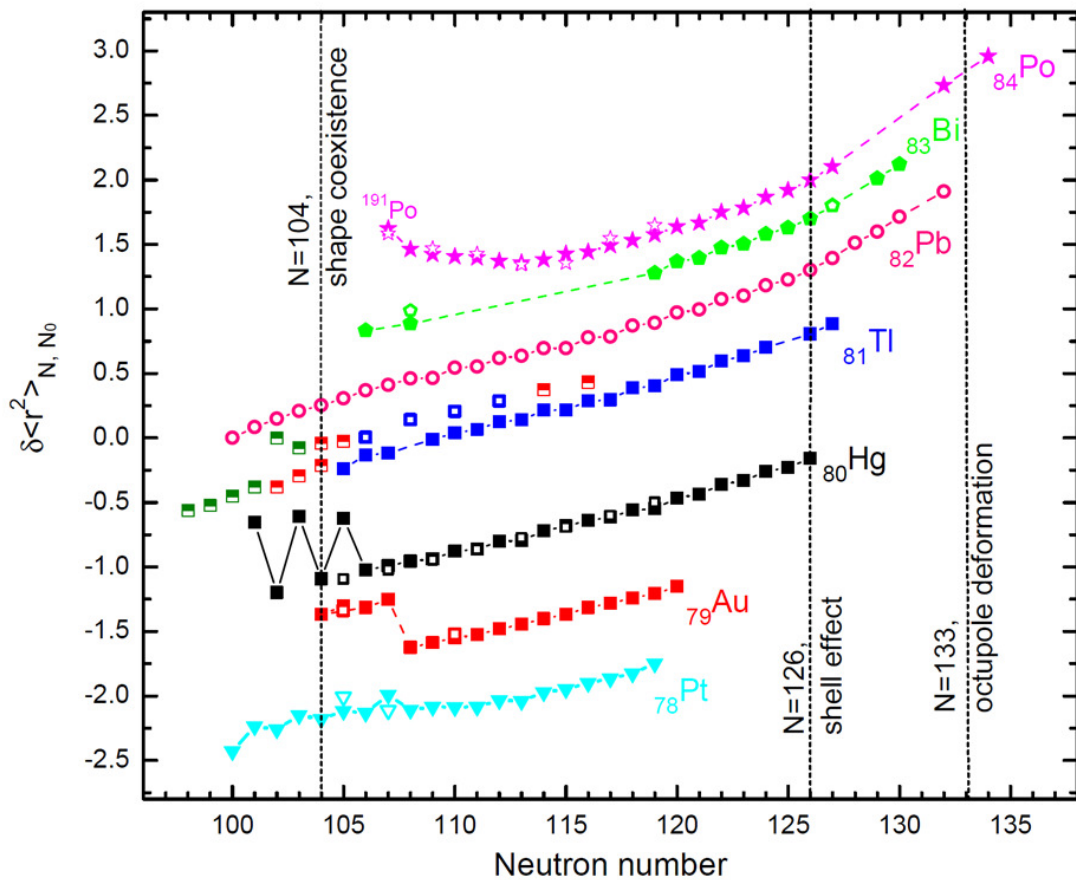


Figure 1.5: Change in mean-squared charge radii for chains of isotopes in the lead region, measured by in-source laser spectroscopy as of 2011.

The famous staggering in the $^{181,183,185}\text{Hg}$ ($Z = 80$) isotopes provided some of the first experimental evidence for the presence of shape coexistence in the lead region [15, 16]. The behaviour was interpreted as two competing structures, one strongly deformed, the other near spherical, coexisting at low energy. This competition results

in the striking transition between the deformed and spherical ground states of the odd- and even-neutron isotopes, respectively.

Between 2003 and 2011 the Windmill collaboration performed in-source laser spectroscopy experiments on the Pb, Po and Tl isotopic chains. The Pb isotopes were shown to remain spherical, even in the region of the $N = 104$ midshell [17, 18]. Above the $Z = 82$ shell closure, a surprisingly rapid onset of deformation was observed in the lightest Po ($Z = 84$) isotopes, when approaching the $N = 104$ midshell [14, 19, 20]. In the Tl chain, the ground states were proven to remain spherical, whereas the intruder isomers were seen to be deformed [21].

During the 2012-2017 period the collaboration completed experimental investigations into the changes in nuclear mean-squared charge radii in the Au, At, Hg and Bi isotopes. Chapter 6 presents the first ever results for optical spectroscopy measurements performed on a chain of At ($Z = 85$) isotopes. It is expected that the At isotopes, which can be considered as a single proton coupled to a Po core, will display a similar behaviour to that of the Po chain. The isotope shifts and hyperfine structures will be presented, along with the extracted values of the change in mean-squared charge radius across the chain, and the values for the nuclear magnetic dipole moments.

Theoretical considerations

2.1 Nuclear models

The atomic nucleus is a complex, many-body quantum system made up of protons and neutrons, collectively known as nucleons. Nucleons interact with each other via all four of the fundamental forces of nature; namely the gravitational force, electromagnetic force, the weak interaction and the nuclear strong force. It is hard to overstate the complexity of the nucleus, especially when it comes to describing it using a theoretical model. For example, ab-initio calculations require an intimate knowledge of the interactions between the fundamental particles that make up the nucleus. To date, only light- to medium-mass nuclei have been modelled using an ab-initio approach [22, 23], with calculations taking months of computing time on some of the world's most powerful computers.

In order to avoid such complexities, many models of the nucleus employ effective theories. These aim to describe the system and its properties by capturing only what is relevant to the energy domain of the nucleus and involve generalised descriptions of the nucleus.

2.1.1 The spherical liquid drop model

The liquid drop model (LDM) provides a macroscopic description of the nucleus. It attempts to describe the saturation properties that nuclei exhibit with increasing mass, for instance, the near-constant binding energy of ~ 8 MeV per nucleon, shown in Fig. 2.1, or the near constant nucleon density of ~ 0.16 fm $^{-3}$ within the interior of the nucleus, as shown in Fig. 2.2.

The model treats the nucleus as a spherical drop of incompressible, dense nuclear fluid with radius,

$$r_{sph} = r_0 A^{\frac{1}{3}}, \quad (2.1)$$

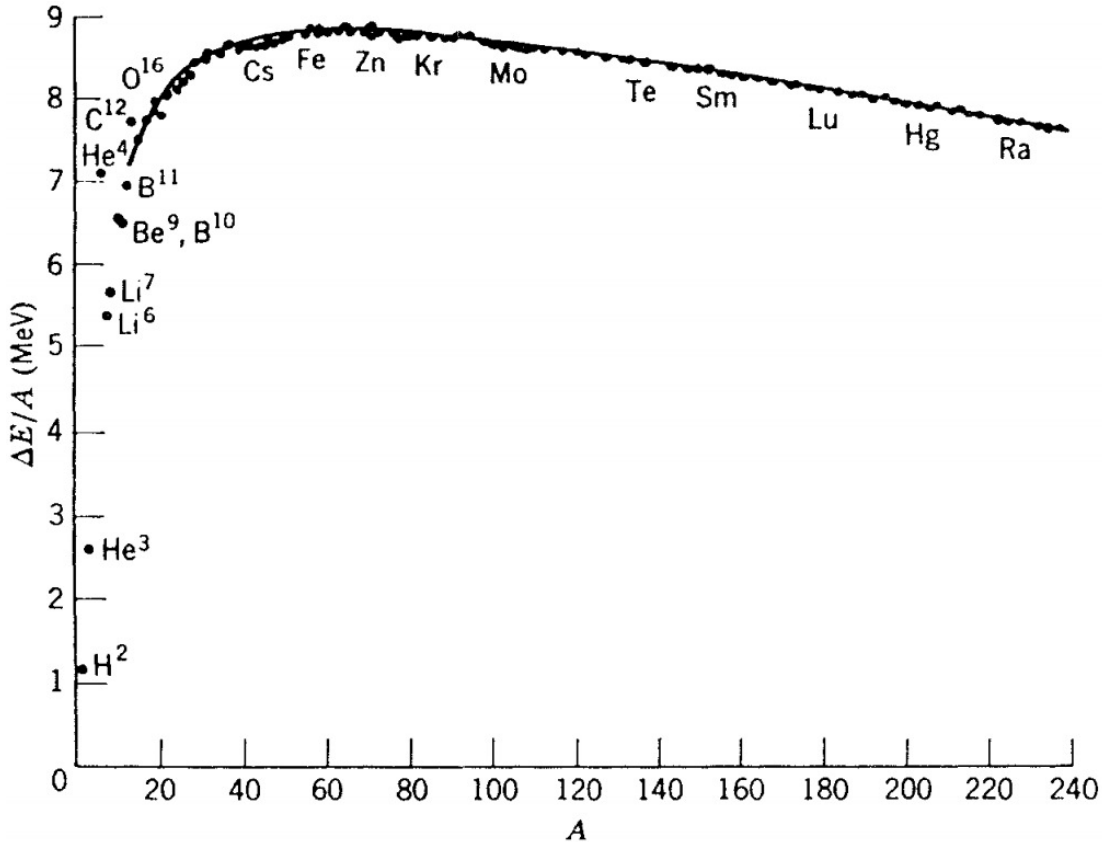


Figure 2.1: Binding energy per nucleon as a function of mass number. The data points represent experimentally-measured values, while the solid line shows the results of the semi-empirical mass formula. Image taken from [24].

where A is the total number of nucleons and r_0 is a constant with a typical value of 1.2 fm.

The LDM led to the development of the Bethe-Weizsäcker formula in 1935. The formula is comprised of five terms used to calculate the binding energy of a nucleus with Z number of protons, N number of neutrons and a mass number, A (where $A = Z + N$).

$$E_B = a_v A - a_s A^{2/3} - a_c \frac{Z(Z-1)}{A^{1/3}} - a_{sym} \frac{(A-2Z)^2}{A} + \delta(A, Z) \quad (2.2)$$

The first term is the volume term which accounts for the increase in binding energy due to the residual strong nuclear force, the attractive interaction between nucleons which binds them together. The second is the surface effect term, a reduction in binding energy due to the nucleons at the nuclear surface not being in contact with as many other nucleons as those in the interior of the nucleus. The third is the Coulomb energy, which reduces the binding energy due to the repulsive

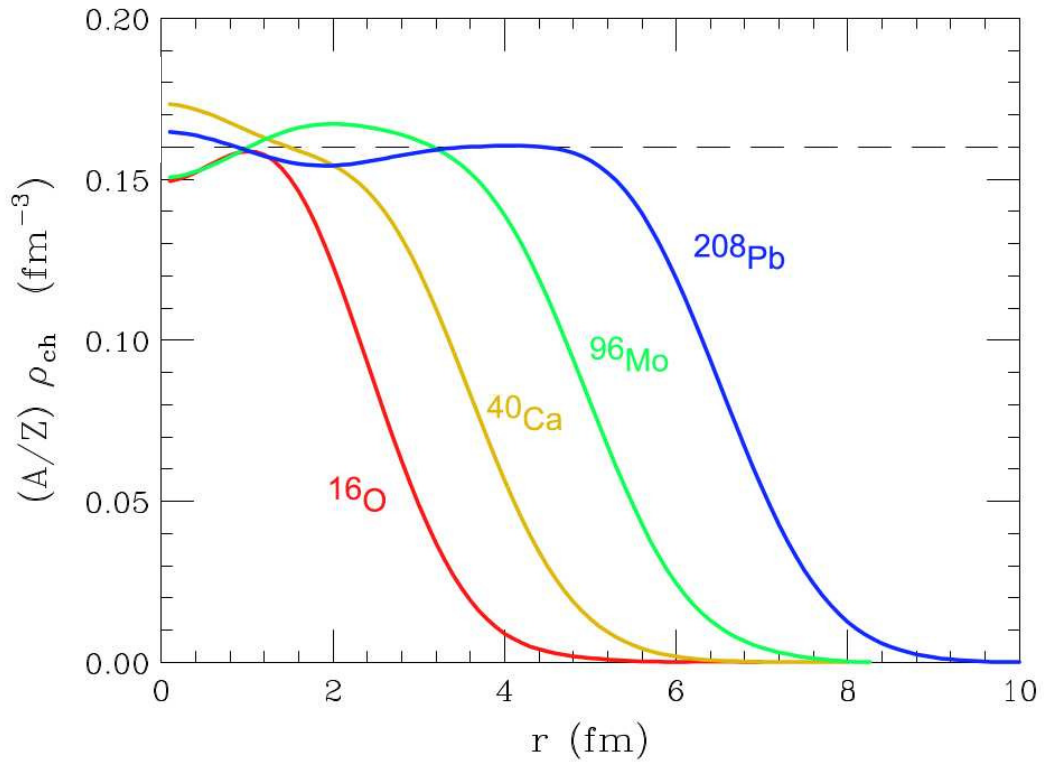


Figure 2.2: Density distribution of nuclear matter as a function of radius. Image taken from [25].

Coulomb interaction between protons within the nucleus. The fourth term is the symmetry term, which represents the effect of the Pauli exclusion principle. As the nucleus is a fermionic system, no two identical fermions can occupy the same state. Thus, nuclei with a large asymmetry in proton and neutron numbers become less energetically favourable. Therefore, this term acts as a correction factor, minimising the energy of $N = Z$ nuclei. The final part of the expression is the pairing term, which represents the gain in binding energy when nucleons couple to pairs of particles in time-reversed orbits. This component is often expressed as $\delta(A, Z) = a_p A^{-3/4}$, with a_p being positive in even-even nuclei, negative in odd-odd systems and zero in nuclei with odd A values.

The values of the parameters a_v , a_s , a_c and a_{sym} are derived from fits of experimental data, which give $a_v = 15.85 \text{ MeV}$, $a_s = 18.34 \text{ MeV}$, $a_c = 0.71 \text{ MeV}$, $a_{sym} = 23.21 \text{ MeV}$ and $a_p = 12 \text{ MeV}$ [26].

The droplet model

The Droplet Model (DM) takes the LDM as a basis, and expands upon it. The original formulation, performed by Myers and Swiatecki [27], was done in order to model the diffuseness of the nuclear surface, which the LDM treats as a sharp cutoff. It also defines proton- and neutron-density distributions separately, which allows for a description of the neutron skins that are observed in some nuclei [28].

Of interest to this work is the systematics of charge radii, extracted from the experimental measurement of isotope shifts (see Section 3.1), for which a new parameterisation of the DM was made specifically [29]. The inclusion of a deformation term to the DM allows a simple comparison to be made between the model and experimental data, from which an estimation of deformation of the nucleus can be made. This provides an insight into the underlying structure that causes the observed trends in the experimental data.

2.1.2 The spherical shell model

Nuclei exhibit a shell structure, similar to that found in atomic electron levels, with shell closures occurring at ‘magic’ proton and neutron numbers of 2, 8, 20, 28, 50 and 82, and also 126 for neutrons. This shell-like behaviour can be seen in the sharp reduction in the neutron (proton) separation energy, S_n (S_p), in nuclei with a single neutron (proton) outside a shell closure. This behaviour is analogous to the low ionisation potentials of Group I elements, which possess a single electron outside of a closed atomic shell. Similarly, the energies of the first excited states of magic nuclei are notably larger than those with non-magic a neutron and/or proton number.

The shell model aims to replicate these observed shell structures using a microscopic approach, whilst still giving a good description of the saturation properties discussed in Section 2.1.1. The shell model describes the nucleus as a many-body fermionic system, bound by a spherically-symmetric, central potential. This potential is created by the motion of all the constituent nucleons, which move independently of one another. The choice of potential used to model the nucleus is important, as it will determine the ordering of states occupied by the nucleons, which in turn defines the properties of the nucleus such as its spin and electromagnetic moments. A good approximation of the nuclear potential is a Woods-Saxon potential, which takes the form

$$V_C(r) = \frac{-V_0}{1 + \exp\left(\frac{r-r_{sph}}{a}\right)}, \quad (2.3)$$

where $V_C(r)$ is the magnitude of the central potential, V_0 is the depth of the well at the centre of the nucleus with a typical value of 50 MeV, r is the distance from the centre of the nucleus, r_{sph} is the radius of the nucleus as given by Equation 2.1, and a is the thickness of the nuclear skin with typical value 0.67 fm.

Nucleons, being fermions, occupy states in accordance with the Pauli exclusion principle; no two identical particles may occupy the same quantal state at any one time. The states nucleons occupy are denoted by the quantum numbers, nl , where n has integer value and is the order of a state with a specific orbital angular momentum, l , which has integer values related to their spectroscopic notation (i.e. $l = 0, 1, 2, 3, \dots$ correspond to orbitals s, p, d, f... etc.). The energy eigenvalues of states with the same n and l quantum numbers are equal, and so levels exist with a degeneracy of $2(2l + 1)$.

The use of a realistic potential gives shell closures at 2, 8 and 20. However, the higher magic numbers are not replicated. In order to reproduce all the observed magic numbers, the inclusion of the spin-orbit interaction is required [30, 31]. This term takes the form

$$V_{so}(r) = V_{ls}(\mathbf{l} \cdot \mathbf{s}) r_0^2 \frac{1}{r} \frac{dV(r)}{dr}, \quad (2.4)$$

where V_{ls} is the strength of the interaction with a typical value of 0.22 MeV, s is the intrinsic spin of the nucleon equal to $\frac{1}{2}$, r_0 is the same as in Equation 2.1 and r is the distance from the centre of the potential. As the spin-orbit interaction is proportional to the derivative, $\frac{dV(r)}{dr}$, it only acts to modify the potential at the surface of the nucleus.

The spin-orbit interaction causes a splitting of states with $l > 0$, into two states labelled with the total spin quantum number j , where $j = l \pm s$. States with $j = l + s$ have their energies reduced, relative to the unperturbed l level, and vice versa for $j = l - s$ states. The magnitudes of the splitting between the $j = l \pm s$ states is dependent on the value of l ; states belonging to higher l orbitals experience larger shifts in energy. These shifts reorder the states, resulting in the reproduction of all the observed shell closures at the correct magic numbers. The new states have a degeneracy of $2j + 1$, and are labelled with a new set of quantum numbers, nlj . Figure 2.4 shows a comparison of results from calculations of single particle energy levels using a Woods-Saxon and a Woods-Saxon plus spin orbit term.

For the total potential of the nucleus, a modification is needed to describe the centrifugal force experienced by nucleons moving within orbits, which is defined as

$$V_{cent}(r) = \frac{l(l+1)\hbar^2}{2mr^2}, \quad (2.5)$$

and in the case of protons, an extra term is required to describe the Coulomb potential they experience, which can be approximated as

$$V_{Coulomb}(r) = \begin{cases} \frac{Ze^2}{2R_p} \left(3 - \left(\frac{r}{R_p} \right)^2 \right), & \text{for } r \leq r_{\text{sph}}, \\ \frac{Ze^2}{r}, & \text{for } r > r_{\text{sph}}, \end{cases} \quad (2.6)$$

where R_p is the proton radius, calculated using Z in the place of A in Equation 2.1.

Thus, the total potentials experienced by protons and neutrons can be defined as:

$$V_{total} = \begin{cases} V_C(r) + V_{so}(r) + V_{cent} + V_{Coulomb}, & \text{for protons,} \\ V_C(r) + V_{so}(r) + V_{cent}, & \text{for neutrons.} \end{cases} \quad (2.7)$$

The forms of these individual components, as well as the sum total potential, are plotted in Fig. 2.3.

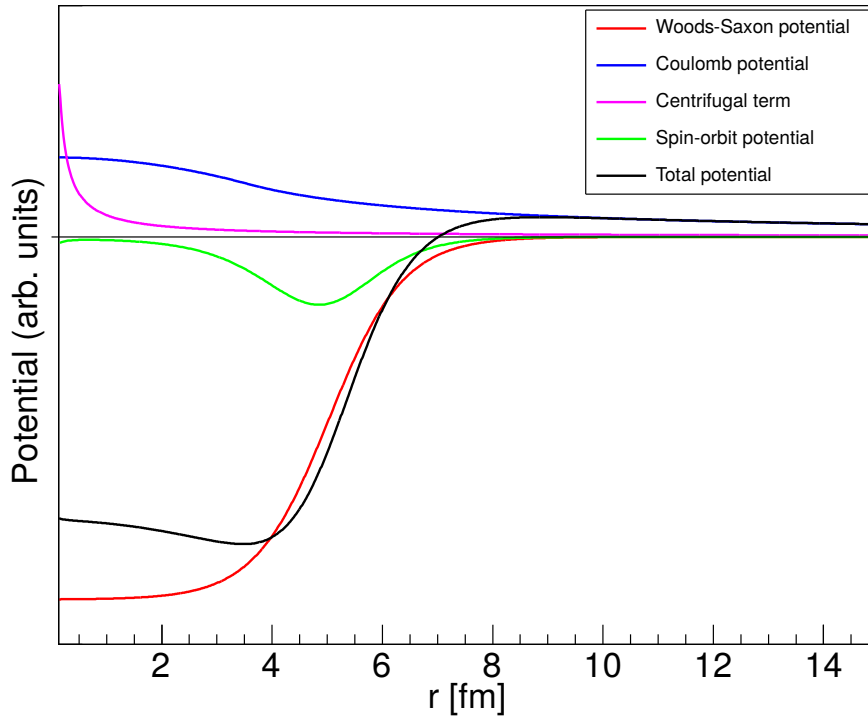


Figure 2.3: The forms of the Woods-Saxon (red), an attractive spin-orbit interaction (green), Coulomb (blue) and centrifugal (pink) terms of Equation 2.1.2, and their combined effects (black). The black horizontal line represents the when the potential is equal to 0. The magnitudes of the potentials are not to scale.

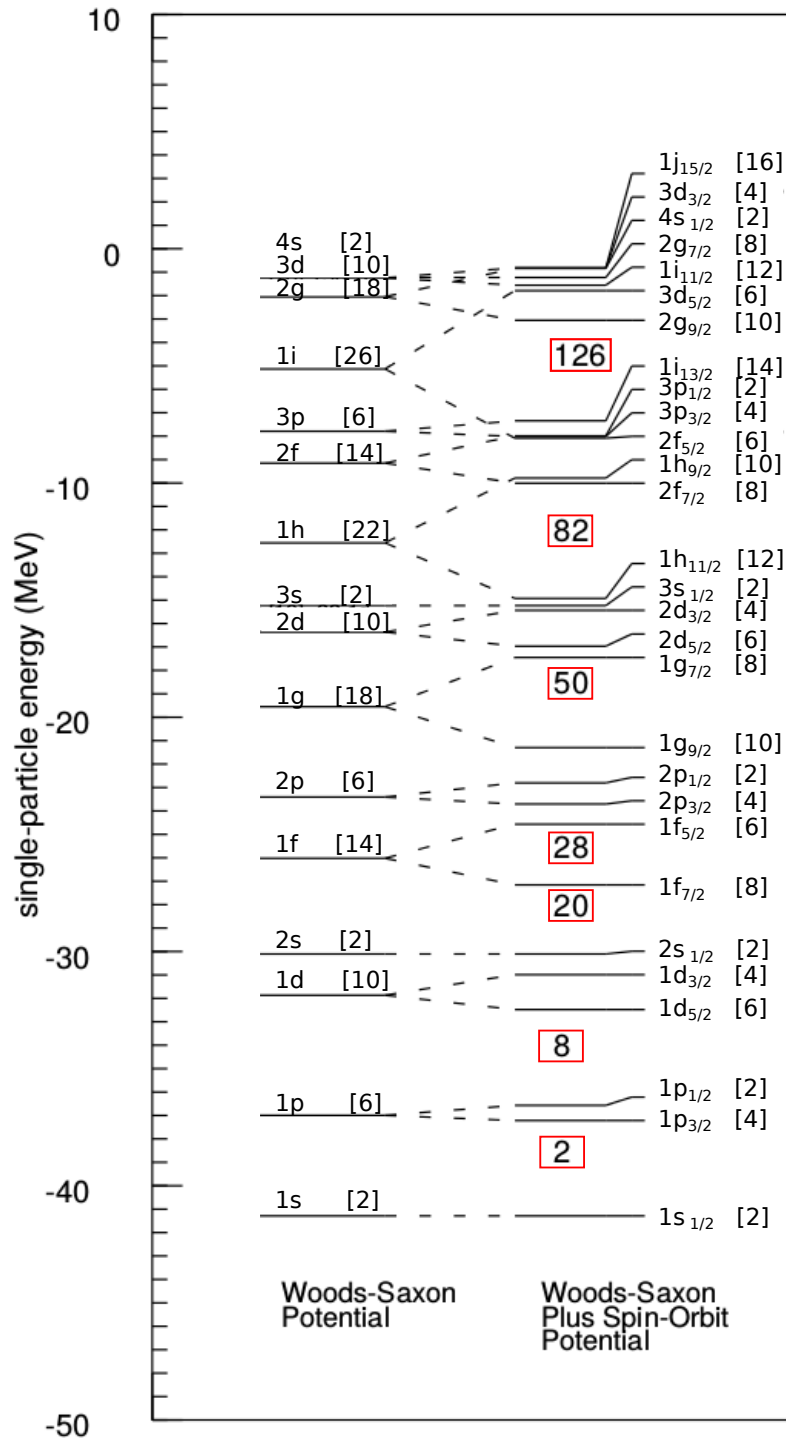


Figure 2.4: Single-particle state energy levels for neutrons in a ^{208}Pb nucleus. The states on the left are solutions for a pure Woods-Saxon potential, and are labelled with the quantum numbers nl . The levels on the right are for a Woods-Saxon plus a spin-orbit term, and are labelled with the nlj numbers. In the square brackets are the degeneracies of each energy level are shown in square brackets, given by $2(2l + 1)$ for the Woods-Saxon, and $2j + 1$ for the Woods-Saxon plus spin-orbit potentials. This figure is adapted from [32].

2.1.3 The deformed shell model

The spherical shell model provides an excellent description of closed-shell, magic nuclei. However, as mentioned in the introduction, the majority of nuclides are non-magic and possess some degree of deformation. The shell model fails to describe the observed properties of these nuclei, such as the spins and masses, or their non-zero electric quadrupole moments, which indicate a non-spherical distribution of charge (i.e. protons) within the nucleus [4]. Many observations have been made of rotational bands of excited states connected by strong E2 γ -ray transitions, built on top of the ground states in even-even nuclei. The energies of the states in these rotational band structures are proportional to $j(j+1)$. Thus, the ratios in energy of the first 2^+ and 4^+ states is $E(4^+)/E(2^+) \approx 3.33$. This suggests many nuclei behave collectively like a rigid ellipsoid rotating around a spin axis.

The most common form of deformation in nuclei is quadrupolar [4], with either prolate or oblate geometries, as shown in Fig. 2.5. The metric for the magnitude of the deformation is the quadrupole deformation parameter, β_2 , given by

$$\beta_2 = \frac{4}{3} \sqrt{\frac{\pi}{5}} \frac{\Delta R}{r_{\text{sph}}}, \quad (2.8)$$

where ΔR is the difference in radius of the semi-major and semi-minor axes of the ellipsoid and r_{sph} is the radius of a spherical liquid drop nucleus, given by Equation 2.1. Prolate geometries have positive values of β_2 , oblate shapes negative, and both retain an axis of rotational symmetry.

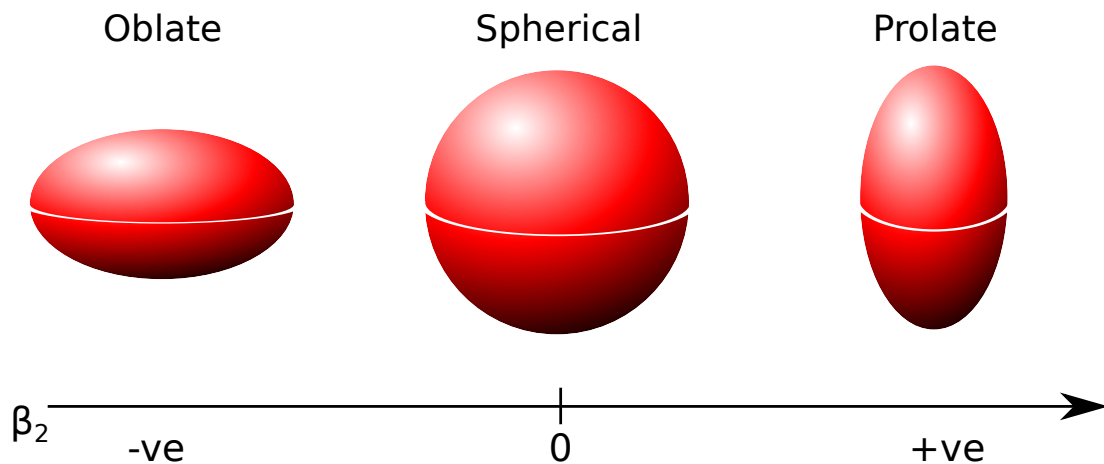


Figure 2.5: Schematic representation of spheroidal geometries as a function of the quadrupole deformation parameter, β_2 .

The deformed shell model, commonly known as the Nilsson model [33], has been successful at describing properties of many deformed nuclei. It is a modification of the spherical shell model that introduces a quadrupole deformation perturbation to the nuclear potential. Unlike in spherical nuclei, an individual nucleon experiences a different potential depending on its orientation relative to the deformed core. Thus, the degeneracies of the spherical shell model states are split in the presence of deformation, and form new Nilsson states. The degeneracies of these Nilsson states change from $2j + 1$ in spherical nuclei, to 2 in deformed systems.

These new Nilsson orbitals are labelled by a new set of quantum numbers, $\Omega^\pi [Nn_z\Lambda]$; Ω is the the projection of j along the axis of symmetry; π is the parity of the state; N is the oscillator shell to which the state belongs; n_z is the number of wavefunction nodes along the axis of symmetry; Λ is the projection of the angular momentum along the axis of symmetry.

The direction and size of the shift in energy of a state is dependent on the spatial orientation of an orbit relative to the deformed core of the nucleus. As the core deforms, some orbits will have a greater overlap with it, giving rise to a stronger interaction. Particles that occupy such orbitals become more tightly bound, which leads to a reduction in their energy level. Conversely, particles that occupy states with a smaller overlap with the core have a weaker interaction and are less tightly bound. This is reflected in the raising of their energy levels.

Figures 2.6 and 2.7 show how the state energy levels are changed as a function of deformation parameter, ϵ_2 , for the region of the nuclear chart that At and Au isotopes occupy. The ϵ_2 parameter indicates the deformation of a rotational ellipsoid and has roughly the same value as β_2 for large deformations. For small deformations, ϵ_2 and β_2 can be related by the approximation

$$\epsilon_2 \approx 0.946\beta_2(1 - 0.1126\beta_2). \quad (2.9)$$

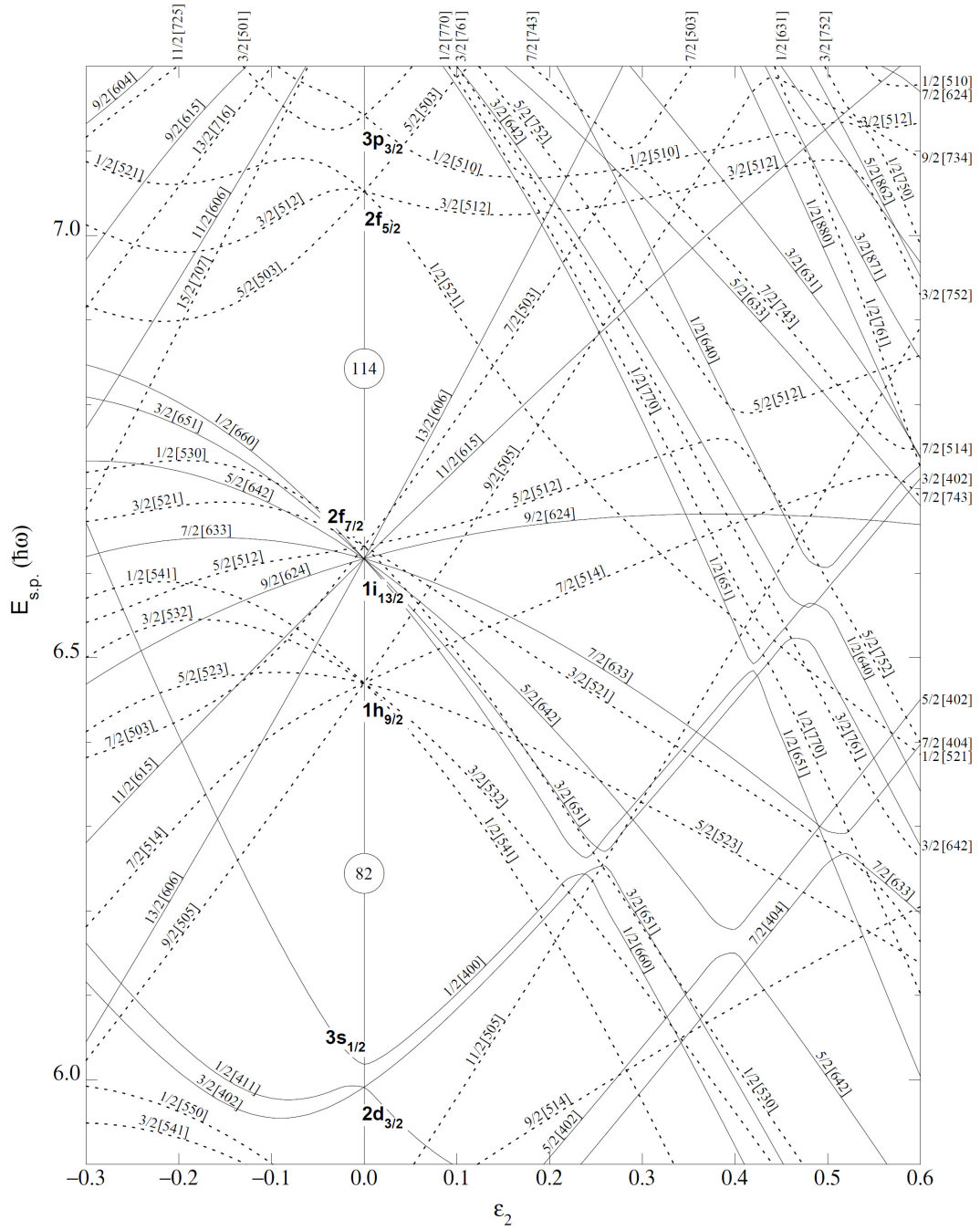


Figure 2.6: Nilsson model single-particle energies for protons in nuclei with $Z > 82$, as a function of the deformation parameter, ϵ_2 [34].

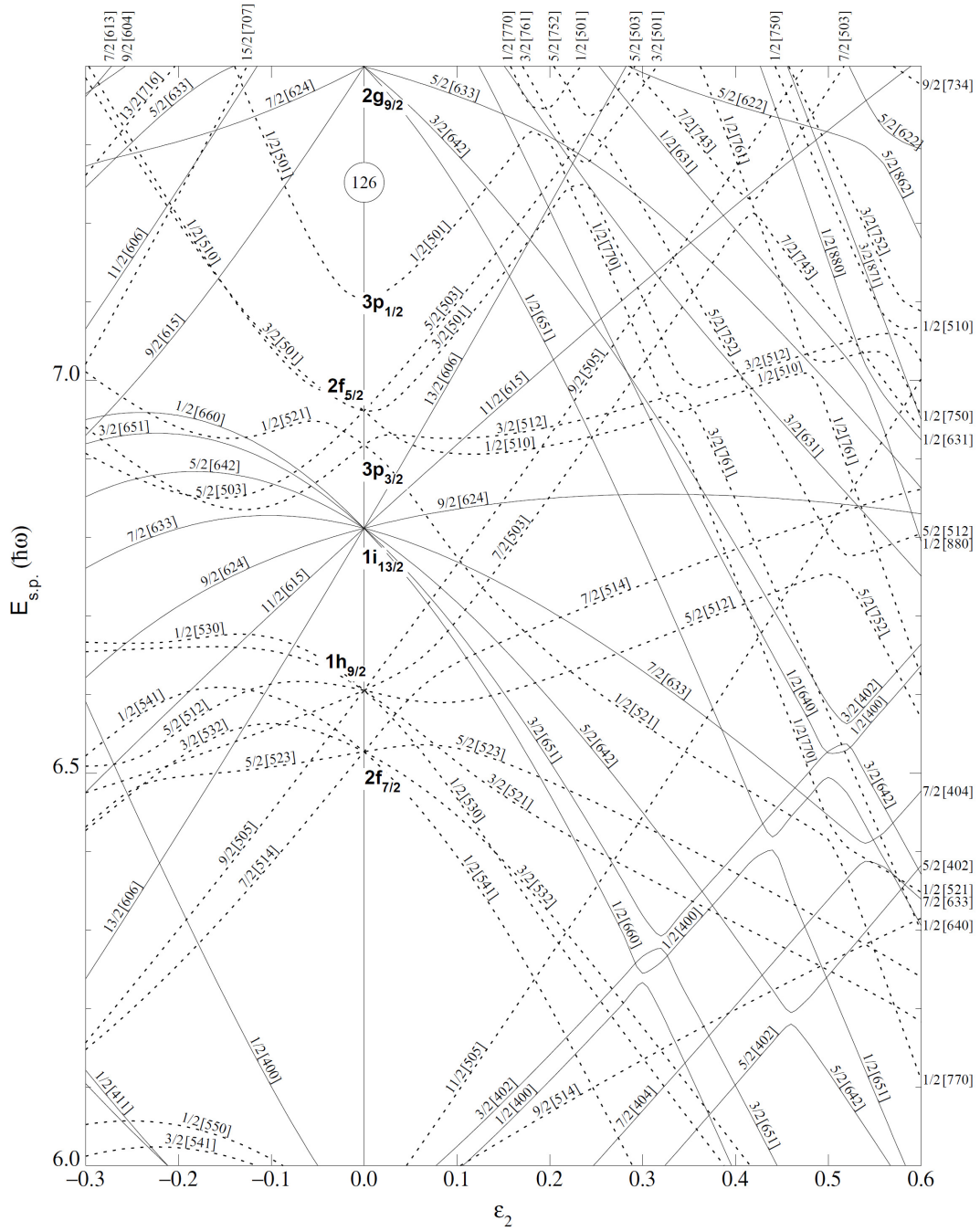


Figure 2.7: Nilsson model single-particle energies for neutrons in nuclei with $82 < N < 126$, as a function of the deformation parameter, ϵ_2 [34].

2.2 Low-energy shape coexistence

Low-energy shape coexistence is the phenomenon by which different configurations of protons and neutrons form low-energy quantal states with distinctly different shapes, within the same nucleus. Incidences of shape coexistence can be found across the nuclear chart, with the most recent review of the field by Kris Heyde and John Wood [7] concluding that it most likely exists in all but the lightest of nuclei.

An analogue to the competing shapes in nuclei can be found within the ground state of the ammonia molecule, albeit on a completely different energy scale. (The molecular potential energy surface in Fig. 2.8 ranges over a few meV, whereas the nuclear potentials in Fig. 2.10 cover tens of MeV.) The ammonia molecule comprises one nitrogen and three hydrogen atoms, arranged in a trigonal pyramid with the nitrogen at the apex. The binding energy of the ammonia molecule as a function of the nitrogen atoms position offset from the hydrogen plane is shown in Fig. 2.8 [35, 36]. Two energy minima exist, with the nitrogen atom either to the left (-ve) or right (+ve) of the plane at ~ 37 pm. These two minima have the same energies and represent two quantum states, of which neither one is preferred as the ground state. They are both equally favourable with respect to minimising the energy of the system, and so the nitrogen atom must “choose” an orientation.

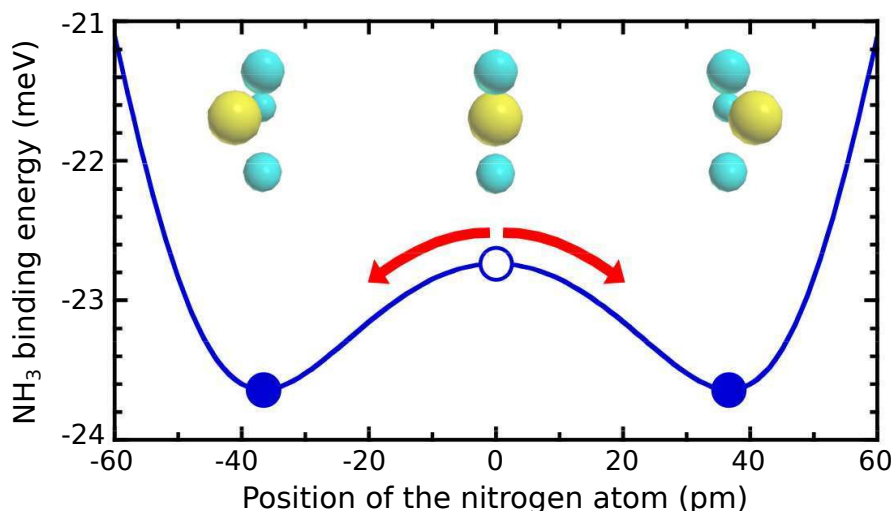


Figure 2.8: Binding energy of the ammonia molecule as a function of distance of the nitrogen atom from the plane of the hydrogen atoms [35, 36].

In nuclei, energy minima of distinctly different geometries compete to become the ground state. The dramatic shape staggering observed in Hg isotopes is a classic example. Figure 2.9 shows the experimental measurements of the ground- (circles) and isomeric-state (crosses) charge-radii by Ulm *et al.* [16]. The solid straight line

indicates where the results would lie in the case of spherical nuclei. The difference in ground-state charge radii becomes pronounced between neighbouring isotopes with $A < 186$. Within this region, the ground states of the even-mass isotopes maintain a ‘normal’, weakly-deformed shape, relative to a strongly-deformed $I^\pi = 1/2$ ground-state configuration adopted by the odd-mass isotopes. This, along with the observation that the $I^\pi = 13/2^+$ isomer in ^{185}Hg adopts the normal deformation, indicates the presence of shape coexistence; two configurations in the same nucleus, with significantly different shapes, coexisting with one another at low energies.

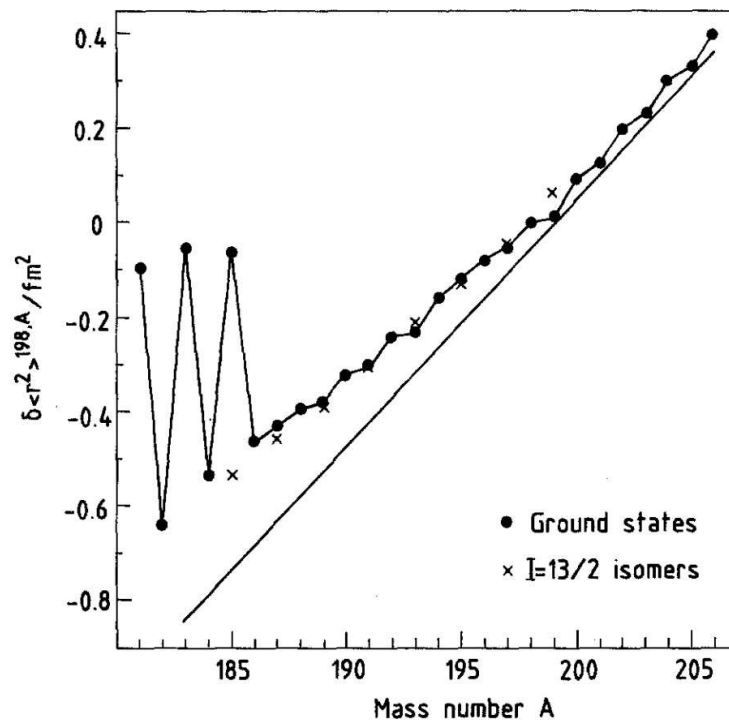


Figure 2.9: Change in mean-square charge radii of the Hg isotopic chain, relative to ^{198}Hg , as a function of mass number, A . The solid, straight line indicates the trend followed by spherical DM Hg isotopes follow. Figure taken from [16].

Modern theoretical calculations, like those in the AMEDEC database [37], aim to describe such experimental observations. The results for the potential energy surfaces of ^{184}Hg , ^{185}Hg and ^{186}Hg as a function of β_2 , from the aforementioned calculations, can be seen in Fig. 2.10. Two minima, an oblate configuration at $\beta_2 \approx -0.17$ and a prolate one at $\beta_2 \approx 0.3$, are seen to compete with one another to become the ground state. The two configurations have almost identical energies in ^{184}Hg , while the prolate configuration becomes the ground state in ^{185}Hg , and the oblate configuration has the lowest excitation in ^{186}Hg . The large barrier in the potential energy surface prevents the two minima from mixing. This results in two states, with distinctly different geometries, as has been experimentally observed.

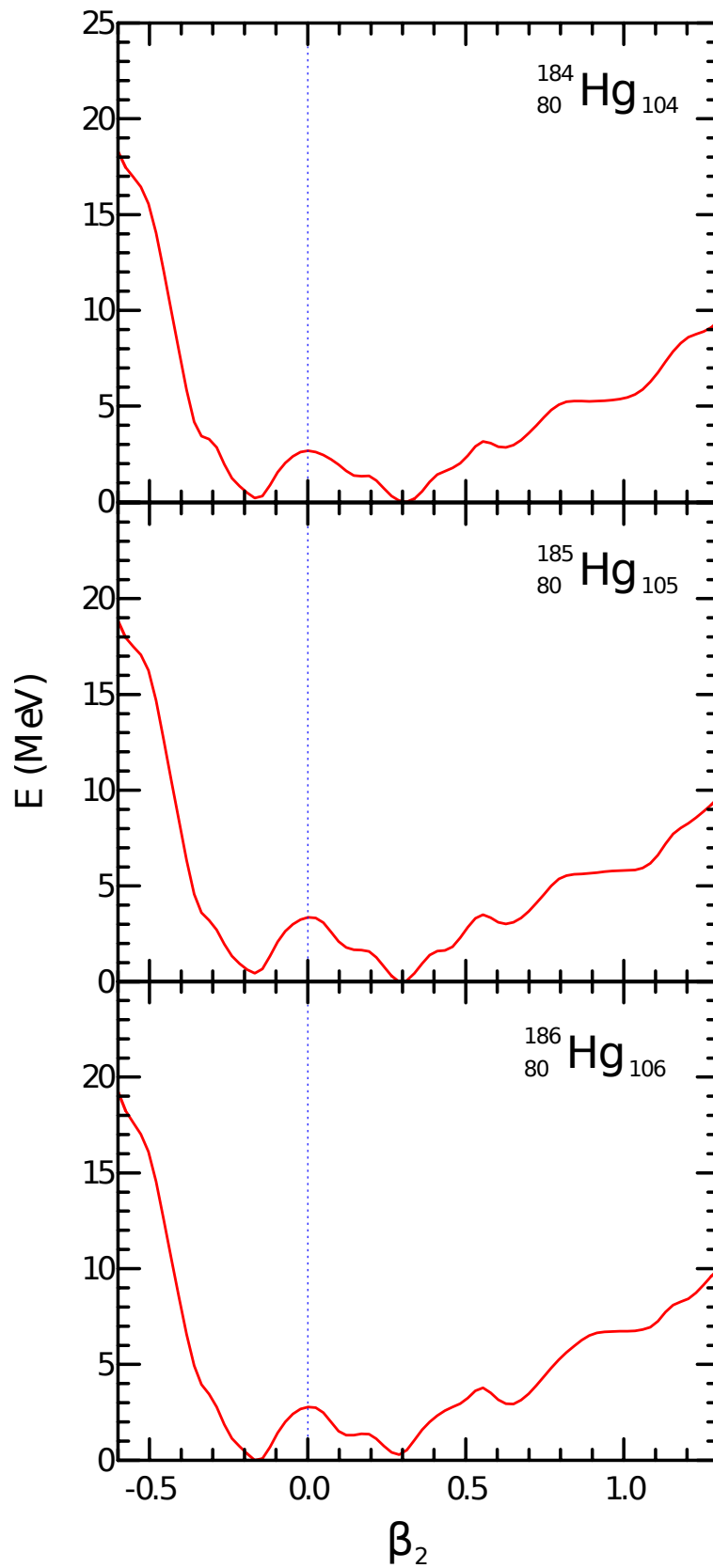


Figure 2.10: Potential energy surface of the ground state energies of $^{184,185,186}\text{Hg}$ as a function of deformation parameter, β_2 [37]. Figures adapted from [38].

2.2.1 Intruder states

One interpretation for the cause of shape coexistence can be found in the Nucleon-Pair Shell Model (NPSM) [39, 40]. In this model, the occupation of so-called intruder states by particle-hole excitations across a major shell gap gives rise to shape coexistence. The energies of intruder states are lower than would be predicted for their configurations, by the spherical shell model. This reduction in energy is due to the combination of three effects: the pairing correlation, ΔE_{pair} , the monopole shift, ΔE_M , and the quadrupole interaction, ΔE_Q . The final energy of an intruder state is given by summing these contributions with the energy of the unperturbed spherical shell model state, such that

$$E_{\text{intr}} = 2(\epsilon_{j_\pi} - \epsilon_{j'_\pi}) - \Delta E_{\text{pair}} + \Delta E_M + \Delta E_Q, \quad (2.10)$$

where $2(\epsilon_{j_\pi} - \epsilon_{j'_\pi})$ is the energy required to excite a pair of protons across the shell gap, to the unperturbed state. Figure 2.11 shows the individual contributions, as well as the combined effect of these three terms for neutron-deficient nuclei around the $Z = 82$ shell closure.

The pairing correlation is the energy gain from coupling particles or holes to $J^\pi=0^+$ pairs, resulting in a gain in binding energy. The average gain in binding energy due to pairing is constant across a nuclear shell, and is of the order of a couple of MeV in the region surrounding the $Z = 82$ shell.

The monopole shift is the change in energy of the unperturbed single-particle proton orbitals due to their interaction with the orbitals filled by the neutrons. The strength of this interaction is dependent on the radial overlap of the proton and neutron orbitals and can be either attractive or repulsive in nature.

The quadrupole interaction is the change in energy due to the proton-neutron quadrupole-quadrupole interaction, an energy gain resulting from the strongly attractive interaction between protons and neutrons. This effect breaks $J^\pi=0^+$ pairs of protons or neutrons into $J^\pi=2^+$ pairs, and in doing so strongly polarizes the core, driving quadrupole deformation. This effect is greatest when the number of pairs of valence protons, N_π , and neutrons, N_ν , is greatest and scales approximately with the product of the two, $N_\pi \cdot N_\nu$.

Within the framework of the Nilsson model (discussed in Section 2.1.3), the low-energy intruder states of the NPSM arise naturally as a result of the deformed mean field. The energies of Nilsson orbitals in the vicinity of major shell closures are seen to change rapidly with increasing deformation. For example, when ϵ_2 decreases away from 0, the energy of the $9/2^- [505]$ in Fig. 2.6 is seen to rapidly decrease.

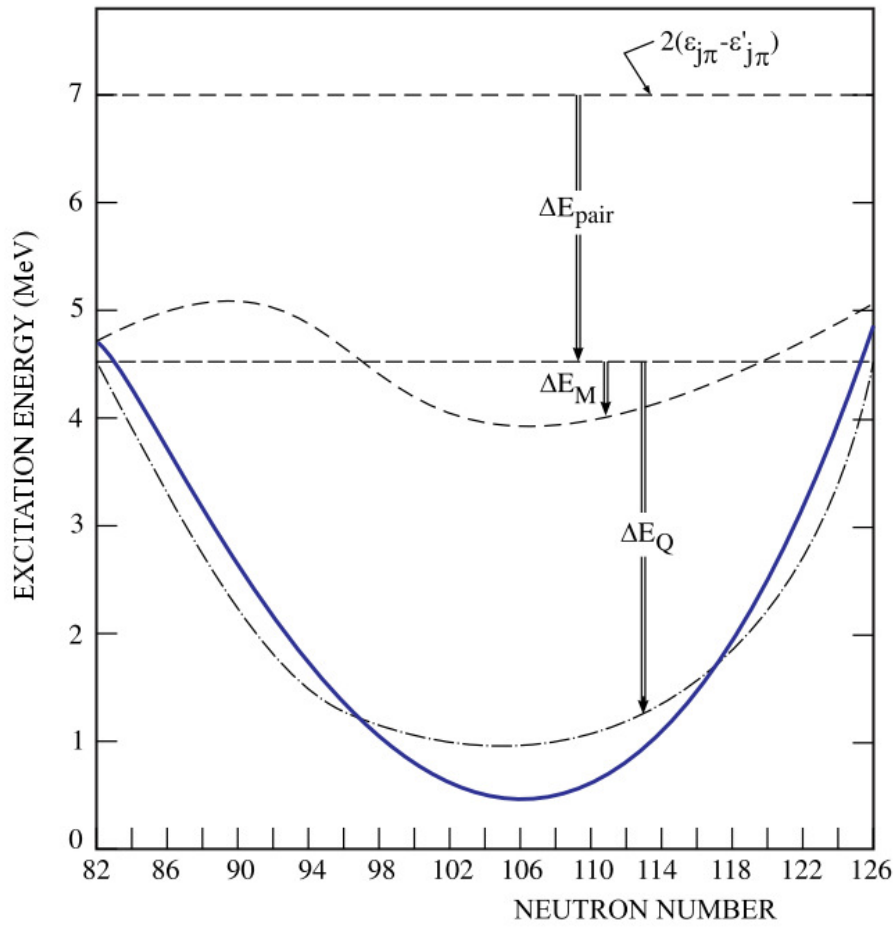


Figure 2.11: A schematic drawing of the impacts of the individual terms upon the unperturbed energy of an intruder state (upper straight dashed line labelled $2(\epsilon_{j\pi} - \epsilon'_{j\pi})$,) for nuclei in the Pb region, as a function of neutron number. Individual contributions can be seen for the pairing correlation (lower straight dashed line) ΔE_{pair} , monopole shift (curved dashed line) ΔE_M and the quadrupole interaction (dot-dashed line) ΔE_Q . The solid blue line is the sum of these effects [7].

As a result, the energy required to make the particle-hole excitation between the corresponding $\pi 3s_{1/2}$ and $\pi 1h_{9/2}$ states of the NPSM reduces [41]. Thus, by equating the two approaches, shape coexistence can be explained within the simple NPSM description of intruder states.

2.3 Probing the structure of the nucleus

Knowledge of the structure of a nucleus may be gained by observing how it decays, or by measuring properties such as the electromagnetic moments or the charge radius. In order to extract information from such observations, it is important to understand how they relate to the underlying structure of the nucleus.

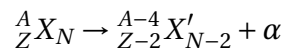
2.3.1 Alpha decay

Alpha decay is the process by which a ${}^4_2\text{He}$ nucleus, known as an α particle, is emitted from a parent nucleus. Alpha particles are emitted with typically high kinetic energies in the range of 5-10 MeV.

The process is a result of the repulsive Coulomb interaction between protons within the nucleus. As the proton number of nuclei increases, so does the Coulomb repulsion to the order of Z^2 . Eventually the repulsive Coulomb force becomes comparable to or greater than the attractive nuclear force that increases approximately linearly with A , resulting in the emission of an α particle.

Due to the double-magicity of the ${}^4_2\text{He}$ nucleus, it has a large binding energy of 28.3 MeV [26], making it energetically preferential for a number of nuclei to emit α particles. Spontaneous α decay occurs predominantly in neutron-deficient nuclei above the $Z = 82$ shell closure, with some cases found in light- and medium-mass nuclei near the extremities of existence.

The mechanism for α decay is given by,



with the total energy released, known as the Q_α -value, given by,

$$\begin{aligned} Q_\alpha &= (m_X - m_{X'} - m_\alpha)c^2 \\ &= E_\alpha + E_{X'}, \end{aligned} \tag{2.11}$$

where m_X and $m_{X'}$ are the parent (X) and daughter (X') atomic masses, respectively, m_α is the mass of the α particle, E_α and $E_{X'}$ are the kinetic energies of the α particle and recoiling daughter nucleus respectively. Alpha particles are emitted spontaneously when $Q_\alpha > 0$. The energy released by the process is shared between the α particle and recoiling nucleus, conserving the momentum of the system. The

relationship between the Q_α value and the α -particle kinetic energy is given by,

$$\begin{aligned} Q_\alpha &= E_\alpha \left(\frac{m_X}{m_{X'}} \right) \\ &\simeq E_\alpha \left(\frac{A}{A-4} \right) \end{aligned} \quad (2.12)$$

where A is the mass number of the parent nucleus.

In addition to the requirement that $Q_\alpha > 0$, α decay obeys certain angular momentum and parity selection rules. The possible values of angular momentum of an α particle, L_α , from an initial state I_i , to a final state I_f , can range from $|I_i - I_f| \leq L_\alpha \leq I_i + I_f$. The ${}^4_2\text{He}$ nucleus has a total spin of 0, and so the α particle carries only orbital angular momentum in transitions between initial and final states. Thus, the corresponding wavefunction of the α particle can be represented as a spherical harmonic, Y_{lm} , with $l = L_\alpha$.

The change in parity associated with such transitions is $(-1)^{L_\alpha}$. This leads to a selection rule for α decay; transitions with even (odd) values of L_α with the same (different) parities between the initial and final states are possible and are called "allowed" decays. The so-called α -decay fine structure, in which α decay populates different states in the daughter nucleus, is a direct result of these spin-parity selection rules. It is possible for a number of final states to be populated by an α transition from an initial state, provided the transition complies with the spin-parity selection rule, and the requirement that $Q_\alpha > 0$.

Alpha decay is a quantum tunnelling process whereby the strong force is represented as a strongly attractive potential with a width equal to the nuclear radius, R , inside of which exists a preformed α particle. Figure 2.12 shows a schematic of this process with the nuclear potential represented by a finite square well. Beyond the nuclear radius is a potential barrier which is the combination of a Coulomb and a centrifugal term. As the α particle moves within the nucleus it will approach the potential barrier with a frequency, ν , and a non-zero probability of penetrating through the barrier, P . These two factors are combined to give the decay constant, $\lambda_\alpha = \nu \cdot P$.

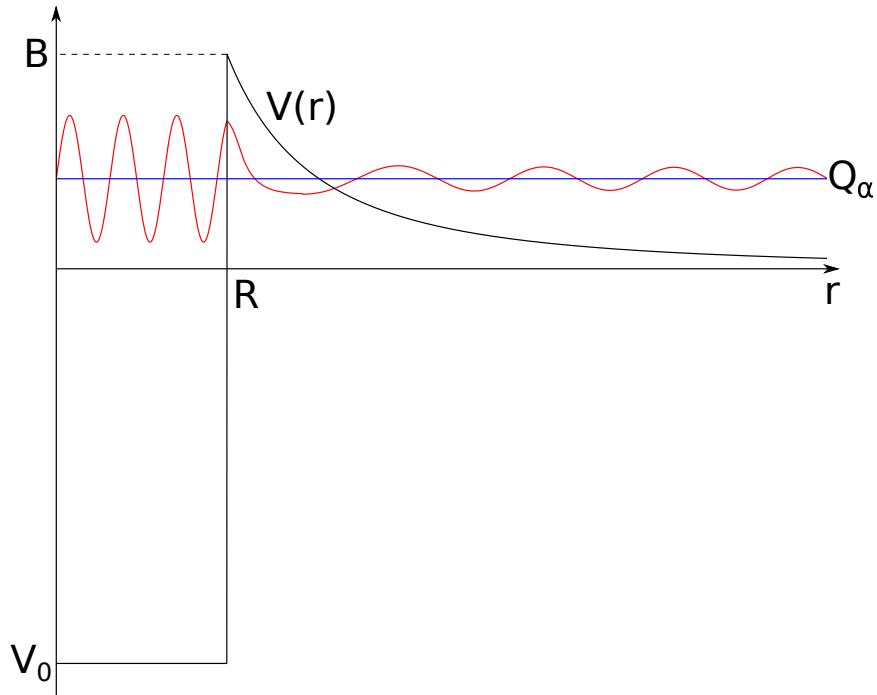


Figure 2.12: A schematic of an α particle in a one-dimensional square well potential, tunnelling through a potential barrier that is the sum of a Coulomb and centrifugal term.

However, this approach does not include the probability that an α particle is formed in the nucleus - known as the preformation factor - which is in turn dependent on the structures of the parent and daughter nucleus. This structural information is contained in a value called the α particle “spectroscopic factor”, also known as the reduced α -width, δ_α^2 . This value is defined as the overlap integral of the parent nucleus wavefunction with the product of daughter nucleus and an α particle wavefunctions:

$$\delta_\alpha^2 = |\langle \psi_i(A) | \psi_f(A-4) \cdot \varphi_\alpha(4) \rangle|^2, \quad (2.13)$$

where $\psi_i(A)$, $\psi_f(A-4)$ and $\varphi_\alpha(4)$ are the wavefunctions of the parent, daughter and α particle respectively.

The value of δ_α^2 can be extracted from experimental measurements of the energy E_α , intensity I_α , half-life $t_{1/2}$, and α -branching ratio b_α , of a decay [42]. These measurements, in conjunction with calculations for the penetration probability P

using the Rasmussen approach [43], can be used to calculate δ_α^2 , such that

$$\delta_\alpha^2 = \frac{h \ln(2) I_\alpha b_\alpha}{t_{1/2} 100 P} \quad (2.14)$$

where h is Planck's constant.

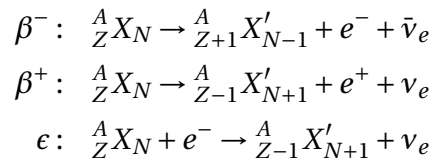
Along with the reduced widths it is often useful to define and compare the so-called hindrance factor (HF_α) of a decay. The strongest component of the fine structure of an α decay is classed as unhindered, and has $HF_\alpha = 1$. The HF_α of a component of the α decay fine-structure, α_2 , is defined relative to that of the unhindered decay, α_1 , such that

$$HF_\alpha = \frac{I_{\alpha 1} P_{\alpha 2}}{I_{\alpha 2} P_{\alpha 1}} = \frac{\delta_{\alpha 1}^2}{\delta_{\alpha 2}^2} \quad (2.15)$$

The HF_α of a decay is sensitive to changes in spin and/or parity between the initial and final state. Large degrees of hindrance are an indication of differing structures between the initial and final states of an α decay process, and therefore is a useful metric when studying the evolving nuclear structures in areas of the nuclear chart where α decay takes place, such as the Pb region.

2.3.2 Beta decay

Beta decay is the collective term for three different processes, namely β -minus decay (β^-), β -plus decay (β^+) and electron capture (ϵ), the mechanisms for which are shown below. These three processes allow either a proton or a neutron to transform into the other via the weak interaction.



The β^- and β^+ processes involve the emission of a β particle in the form of an electron (e^-) or positron (e^+), respectively. Unlike α decay, the energies of the particles emitted in β^- and β^+ decay are not quantised but have a continuous distribution. This is due the fact that β^- and β^+ decay are three-body processes, with the total energy of the decay being shared amongst the daughter nucleus (X'), the β particle (e^- or e^+) and the electron neutrino (ν_e or $\bar{\nu}_e$).

The electron capture process involves the capture of an atomic electron, usually from one of the inner atomic orbitals, as these electrons have the greatest wavefunction overlap with that of the nucleus. An electron occupying a higher orbital will de-excite to fill the vacancy left by the captured electron. In order to conserve the energy of the system, an x ray is emitted with energy characteristic of the initial and final states of the de-exciting electron. This x ray is labelled according to the shell the captured electron originates from (i.e. K, L, M, etc.).

As with α decay, β decay obeys spin-parity selection rules:

$$\mathbf{I}_i = \mathbf{I}_f + \mathbf{L}_\beta + \mathbf{S}_\beta$$

$$\pi_P = \pi_D (-1)^{L_\beta},$$

where L_β represents the change in spin due to the orbital angular momentum carried away by the decay, and S_β is the coupled spin of the β particle-neutrino pair. As both the β particle and neutrino are spin = 1/2 fermions, S_β can equal 0, or 1 for the antiparallel and parallel coupling, respectively.

There are two classes of β decay: allowed and forbidden transitions. Allowed transitions have no change in parity, and $L_\beta = 0$. There are two types of allowed decays: Fermi ($S_\beta = 0$), and Gamow-Teller ($S_\beta = 1$).

Forbidden transitions span a number of orders, with first forbidden decays having $L_\beta = 1$, second forbidden with $L_\beta = 2$, third forbidden $L_\beta = 3$, and so on. As orbital angular momentum is carried away by these transitions, there can also be changes in parity between the initial and final states. Forbidden decays have significantly lower transition probabilities compared to allowed decays. This is reflected in their long partial half-lives, relative to those of allowed transitions.

2.3.3 Gamma decay

Gamma decay is the process by which a photon is emitted during the de-excitation of a nucleus from an initial to a final state. Alpha and beta decay often populate excited states in the daughter nucleus, and so are followed by γ transitions. Typical γ -ray energies range from tens of keV to a few MeV. The energy of the photon emitted by a γ decay, E_γ , is defined as

$$E_\gamma = E_i - E_f - T_X, \quad (2.16)$$

where E_i and E_f are the energies of the initial and final states of the transition, and T_X is the small amount of kinetic energy imparted to the nucleus in order to conserve

the momentum of the system. This recoil energy is defined as

$$T_X = \frac{p_X^2}{2m_X} = \frac{p_\gamma^2}{2m_X} = \frac{E_\gamma^2}{2m_X c^2}, \quad (2.17)$$

where p_X and p_γ are the momenta of the recoiling nucleus and γ photon, respectively, m_X is the mass of the recoiling nucleus, and c is the speed of light. Due to the rest-mass energies of nuclei being much greater than typical γ -ray energies, T_X has a very small value, and usually not included in Equation 2.16.

The photons emitted in γ decays come in two classes, electric (E) and magnetic (M), and have a multipole order of 2^L . The spin-parity selection rules associated with γ decay are:

$$|I_i - I_f| \leq L \leq I_i + I_f$$

$$\pi(EL) = (-1)^L, \text{ or, } \pi(ML) = (-1)^{L+1},$$

where L is the angular momentum carried away by the γ ray. Estimations of the partial half-life for the emission a γ ray due to the de-excitation of a single particle are given by the Weisskopf estimates:

Table 2.1: Weisskopf estimates for the single-particle γ -transition half-lives [34].

ΔL	$t_{1/2}(E)$ [s]	$t_{1/2}(M)$ [s]
1	$\frac{6.76 \times 10^{-6}}{E_\gamma^3 A^{2/3}}$	$\frac{2.20 \times 10^{-5}}{E_\gamma^3}$
2	$\frac{9.52 \times 10^6}{E_\gamma^5 A^{4/3}}$	$\frac{3.10 \times 10^7}{E_\gamma^5 A^{2/3}}$
3	$\frac{2.04 \times 10^{19}}{E_\gamma^7 A^2}$	$\frac{6.66 \times 10^{19}}{E_\gamma^7 A^{4/3}}$
4	$\frac{6.50 \times 10^{31}}{E_\gamma^9 A^{8/3}}$	$\frac{2.12 \times 10^{32}}{E_\gamma^9 A^2}$

As well as the angular momenta and parities of initial and final states, the shape of the nucleus also plays a role in the γ decay process. A nucleus with a certain order of deformation will have its protons, and thus its electric field, shaped accordingly. E-type transitions of the same multipolarity more readily couple to the pre-existing field created by the deformed nucleus, resulting in an increase in their transition strengths.

Internal Conversion

Internal conversion is an electromagnetic process by which the nucleus de-excites via the emission of an atomic electron, and competes directly with γ decay. The probability of internal conversion occurring depends on the energy of the γ -ray transition with which it competes, increasing for lower energy and higher multipolarity transitions. This probability also increases with higher Z values of the nucleus in which it occurs. There is a non-zero probability of internal conversion occurring instead of any γ transition, with the exception of nuclei of fully ionised atoms. Single γ decay is impossible in cases where the spins of the initial and final states are equal to zero. However, internal conversion may still occur, such transitions are known as E0 transitions.

Unlike electrons released in β decay, conversion electrons are monoenergetic, and have a characteristic kinetic energy, T_e , given by

$$T_e(\Lambda) = E_\gamma - E_B(\Lambda), \quad (2.18)$$

where E_B the binding energy of the electron, and Λ denotes the shell from which it originates (i.e. K, L, M, etc.). Therefore, internal conversion can only occur when $E_\gamma > E_B$. As with the electron capture process discussed in Section 2.3.2, and for the same reasons discussed therein, the conversion electron typically originates from an orbital in one of the inner electron shells, and is followed by a characteristic x ray. The conversion electron is labelled with the atomic shell from which it originates.

By detecting the number of characteristic conversion electrons, or x rays, it is possible to calculate the conversion coefficient, α_c , for electrons from a specific shell, such that

$$\alpha_c(\Lambda) = \frac{I_{ce}(\Lambda)}{I_\gamma} \quad (2.19)$$

where I_{ce} and I_γ are the intensities of the internal conversion process, and the γ transition, respectively. Thus, the total conversion coefficient, $\alpha_{c,tot}$, is defined as

$$\alpha_{c,tot} = \alpha_c(K) + \alpha_c(L) + \alpha_c(M) + \dots \quad (2.20)$$

Other more exotic processes exist through which a nucleus can de-excite, such as double γ decay [44, 45] or the internal electron-positron pair production [46] processes. However, these processes are not relevant to this work and so will not be discussed further.

Laser spectroscopy

Laser spectroscopy provides an excellent technique for making systematic studies across the nuclear chart. By performing such investigations, one can map the evolving structures of ground and isomeric states across whole regions of the nuclear landscape. Experimental investigations involve measuring the isotope shifts and the atomic hyperfine structure (HFS) of nuclei along the isotopic chain of a particular element [47]. By measuring the isotope shifts, the changes in nuclear mean-square charge radius between isotopes can be observed. From measurements of the HFS it is possible to extract properties of the nucleus such as its spin, magnetic dipole moment and spectroscopic electric quadrupole moment. All this can be done without dependence on nuclear models for interpretation of the results – an advantage that is unique to the laser spectroscopy method [48].

3.1 Isotope and isomer shifts

The energy required for a specific atomic transition is observed to shift between different isotopes of the same element. These shifts, known as the isotope shift, are a result of the change in mass and size between isotopes, A and A' . The isotope shift can be measured by observing the difference in frequency of light from a laser used to make the same atomic transition, in different isotopes. Thus, the isotope shift, $\delta\nu^{A,A'}$, is defined as [49]

$$\delta\nu^{A,A'} = \nu^{A'} - \nu^A, \quad (3.1)$$

where $\nu^{A'}$ (ν^A) is the laser frequency required to make the transition in isotopes A' (A), known as the central transition frequency.

Generally the isotope shift can be split into two components, the mass shift and

the field shift, such that

$$\delta\nu^{A,A'} = \delta\nu_{MS}^{A,A'} + \delta\nu_{FS}^{A,A'}. \quad (3.2)$$

The mass shift, $\delta\nu_{MS}^{A,A'}$, is caused by the change of the total mass of the system, when the number of nucleons is changed. It can be broken down into two parts, the normal mass shift (NMS) and the specific mass shift (SMS). The former is a result of the change in the reduced electron mass and the latter is caused by electron-electron correlations within multi-electron systems. The total mass shift is a combination of these two components and can be expressed as

$$\delta\nu_{MS}^{A,A'} = \frac{m_{A'} - m_A}{m_A m_{A'}} M, \quad (3.3)$$

where m_A and $m_{A'}$ are the masses of isotopes A and A' , and $M = M^{NMS} + M^{SMS}$, where M^{NMS} and M^{SMS} are the NMS and SMS, respectively. The SMS value must be calculated using large-scale atomic calculations, or calibrated using experimental results [50]. The NMS can be calculated exactly, using the expression

$$M^{NMS} = \frac{\nu \cdot m_e}{m_p}, \quad (3.4)$$

where ν is the transition frequency, m_p is the mass of a proton, and m_e the mass of an electron.

The field shift, $\delta\nu_{FS}^{A,A'}$, is caused by changes in the distribution of charge inside the nucleus. This leads to differences in the spatial overlap between the nuclear volume and the electron wavefunction. This means that it is sensitive to the changes in the mean-squared charge radii between different nuclides. The field shift is defined as

$$\delta\nu_{FS}^{A,A'} = F \delta\langle r^2 \rangle^{A,A'}, \quad (3.5)$$

where F contains the optical transition dependence, and $\delta\langle r^2 \rangle^{A,A'}$ is the change in mean-squared charge radius between isotopes A and A' . As with M , F can either be calculated using models, or calibrated from experimental data.

By combining these expressions for the mass and field shifts, an expression for the total isotope shift can be constructed [51]:

$$\delta\nu^{A,A'} = M \frac{m_{A'} - m_A}{m_A m_{A'}} + F \delta\langle r^2 \rangle^{A,A'}. \quad (3.6)$$

By using this expression, the change in mean-squared charge radius between different isotopes can be extracted from experimental measurements of the isotope shift. This can also be applied to isomer shifts, from which the change in mean-

squared charge radius between different states within the same nucleus can be extracted. To this end, laser spectroscopy can be used as an effective tool in the search for shape coexistence.

3.2 The hyperfine structure

The hyperfine structure (HFS) is a result of the coupling of non-zero atomic spins, J , and nuclear spins, I . This coupling results in a splitting of the atomic levels into new hyperfine states, identified by a new quantum number, F , such that:

$$\mathbf{F} = \mathbf{I} + \mathbf{J}, \quad (3.7)$$

where F is the total spin of the hyperfine level. Transitions between hyperfine states are allowed if $\Delta F = 0, \pm 1$, with the exception of transitions between two states with $F = 0$, which are forbidden.

The shift in energy of a hyperfine level, relative to the unperturbed atomic level, is defined as

$$\Delta E = a \frac{K}{2} + b \frac{3K(K+1) - 4I(I+1)J(J+1)}{8I(2I-1)J(2J-1)}, \quad (3.8)$$

where K is given by:

$$K = F(F+1) - I(I+1) - J(J+1), \quad (3.9)$$

and a and b factors are the so-called hyperfine parameters, which are related to the magnetic dipole and electric quadrupole moments of the nucleus, respectively. The factor a is defined as

$$a = \frac{\mu B_e}{IJ}, \quad (3.10)$$

where μ is the nuclear magnetic dipole moment, and B_e is the magnetic field produced by the electrons at the site of the nucleus. The b factor is defined as

$$b = eQ_s \left\langle \frac{\delta^2 V_e}{\delta z^2} \right\rangle, \quad (3.11)$$

where Q_s is the nuclear electric quadrupole moment and $\langle \delta^2 V_e / \delta z^2 \rangle$ is the average electric field gradient generated by the electrons at the site of the nucleus.

3.2.1 Magnetic dipole moment

The magnetic dipole moment is a result of the motion of protons and neutrons within the nuclear volume. Nucleons that couple to $J^\pi=0^+$ pairs produce magnetic dipole moments of equal magnitude but opposite sign, resulting in a zero net dipole moment for an even-even nucleus. In odd-mass nuclides, the total dipole moment results from the motion of the remaining unpaired valence nucleon, and so gives an insight to the single-particle nature of the orbitals they occupy. For odd-odd nuclei, both unpaired nucleons play a role, and so the evaluation of the total magnetic moment of a nucleus is performed using the so-called additivity rule (See discussion in Section 6.5.2).

3.2.2 Electric quadrupole

The electric quadrupole moment is sensitive to the distribution of charge within the nucleus. It provides a metric for describing both the magnitude, and sign of the quadrupole deformation (whether the nucleus is oblate or prolate).

The spectroscopic quadrupole moment, Q_s , can be related to the intrinsic quadrupole moment, Q_0 , using the strong-coupling projection formula,

$$Q_s = Q_0 \left(\frac{3\Omega^2 - I(I+1)}{(I+1)(2I+3)} \right), \quad (3.12)$$

where Ω is the projection of the nuclear spin along the symmetry axis of the nucleus.

The intrinsic quadrupole moment can be used to calculate the deformation factor $\langle\beta_2\rangle$:

$$Q_0 \approx \frac{5Z\langle r^2\rangle_{sph}}{\sqrt{5\pi}} \langle\beta_2\rangle (1 + 0.36\langle\beta_2\rangle), \quad (3.13)$$

where $\langle r^2\rangle_{sph}$ is the mean-square charge radius of the same nucleus if it were spherical. This value can be calculated using the droplet model.

Experimental method

The results discussed in this thesis are from experiments performed at the Iso-
tope Separator On-Line DEvice (ISOLDE) facility at CERN (Geneva, Switzerland).
The facility is located next to the Proton-Synchrotron Booster (PSB) at the CERN
accelerator facility, shown in Fig. 4.1.

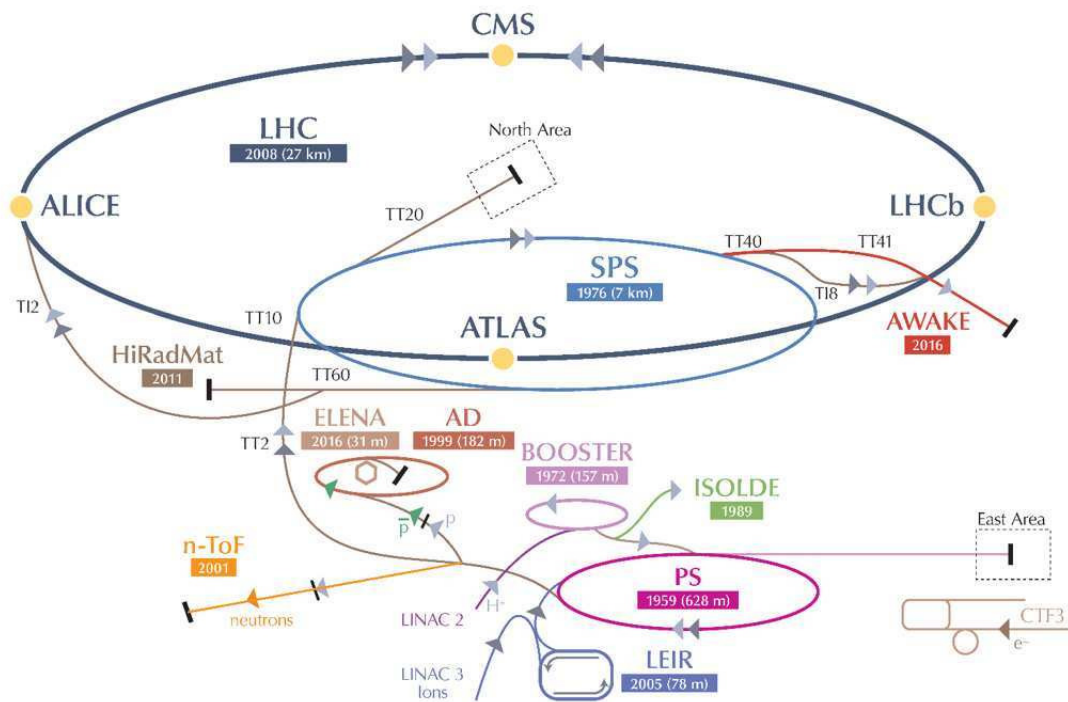


Figure 4.1: A schematic representation of the CERN accelerator complex, taken from [52]. The ISOLDE facility is shown in green.

4.1 ISOLDE facility

The ISOLDE facility at CERN began operation in 1967 and underwent major upgrades in 1974 and in 1992. A layout of the current facility is shown in Fig. 4.2. It employs the Isotope Separation On-Line (ISOL) technique [53] in order to produce radioactive ion beams.

The facility is home to two mass separators which deliver high-purity beams to a number of permanent, or travelling experiments. To date, more than 20 different target materials and ionisers are available for use, providing over 1300 different isotopes of 73 different elements for experimental investigation [54].

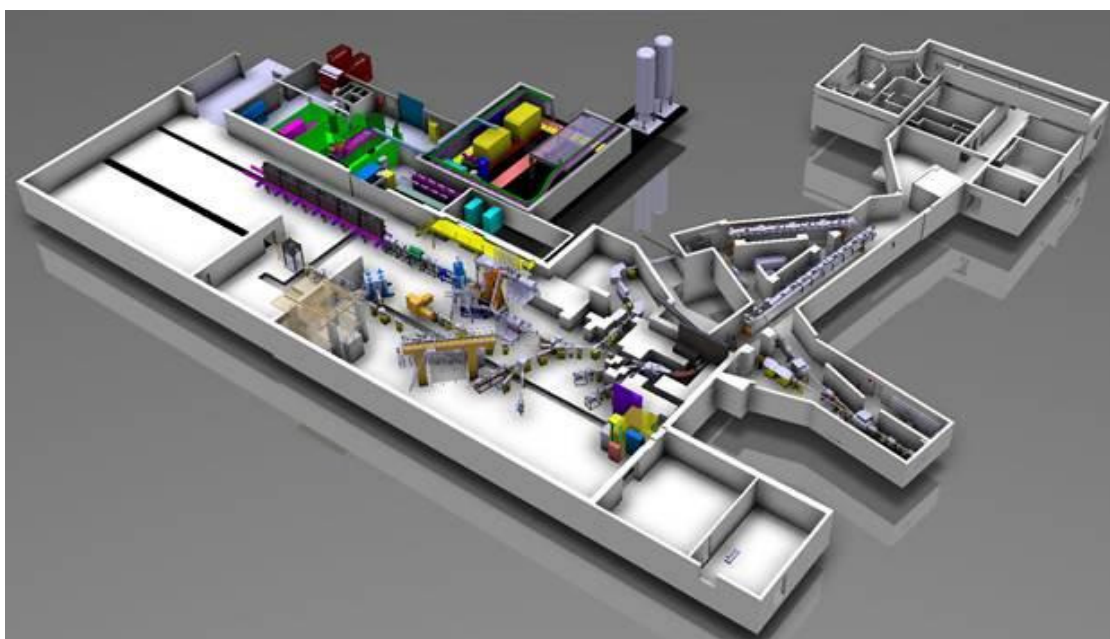


Figure 4.2: A three-dimensional computer model of the ISOLDE facility, CERN [55].

The At and Au isotopes that are the focus of this work were produced by bombarding a thick UC_x target with high-energy protons. The At and Au atoms were then ionised using the laser ion source, extracted by an electrostatic potential and then mass separated. The mass-separated beams were then delivered to either the Windmill decay station or the ISOLTRAP MR-ToF. The Windmill decay station was used to perform decay studies and measurements of the HFS and isotope shifts of short-lived α -decaying isotopes. The ISOLTRAP MR-ToF was used to make HFS and isotope shift measurements on stable or long-lived nuclides, or in cases where high levels of isobaric contamination was present. An overview of the entire beam production and delivery process is shown in Fig. 4.3, and a more detailed discussion of the different stages is given in the following sections.

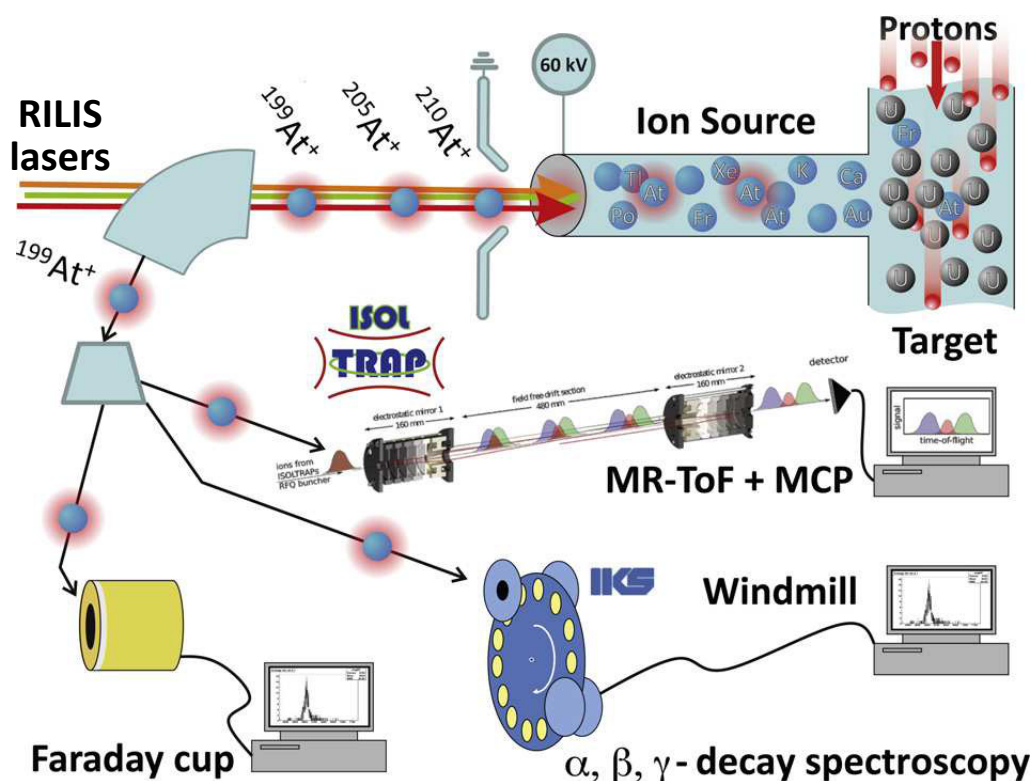


Figure 4.3: Schematic drawing of the in-source resonance ionisation spectroscopy setup for the experiment on At beams [56]. The figure includes the proton beam incident on the UC_x target, the lasing light from RILIS and extraction of the At ions from the ion source, the mass separation by a bending magnet and the delivery of the ion beam to three different detection setups, namely the Faraday cup, the Windmill system and the ISOLTRAP MR-ToF.

4.2 Radioactive beam production

At ISOLDE a 1.4 GeV pulsed-proton beam is delivered to the facility by the PSB, in order to produce a wide variety of nuclides for experimental investigation. The pulses have a length of $2.4 \mu\text{s}$, a spacing of 1.2 s, and contain up to 3.1×10^{13} protons, giving an average current of $2.1 \mu\text{A}$ [57]. The pulses are organised in a logical sequence called a supercycle (SC) which typically consists of 35-40 proton pulses that are distributed across CERN depending on the needs of the different facilities. During an experiment, ISOLDE will typically receive 50% of the pulses within a SC.

During the At and Au experiments, 50 g/cm^2 UC_x targets were used, upon which the proton beam was impinged. These high-energy collisions induced spallation, fission and fragmentation reactions within the target, details of which are given below (see Fig. 4.4).

- Fission – The target nucleus is excited above the fission barrier, allowing nuclear fission to occur which produces two large daughter fragments, plus a number of free neutrons. The A/Z ratio of the parent nucleus of a fission process is greater than that of the stable isotopes of the daughter products. Thus, the fission process allows experimental access to a large number of neutron-rich isotopes, with $A \approx 140$ -150.
- Fragmentation – This is the primary reaction mechanism used to produce the lightest nuclei for study, such as the halo nucleus ${}^{11}\text{Li}$. These reactions result in the production of two daughter nuclei; a light- and a heavy-mass nucleus, with the latter having a similar mass to those of the isotope used for the target.
- Spallation – A two-stage process in which a relativistic particle collides with a target nucleus. This collision excites multiple constituent protons and neutrons within the target nucleus, into high-energy states. What then follows is called an intranuclear cascade in which the nucleus de-excites either by evaporating off nucleons, or through the emission of γ rays. Spallation reactions produce neutron-deficient nuclei and are the primary mechanism for the creation of At and Au isotopes studied in this work [58].

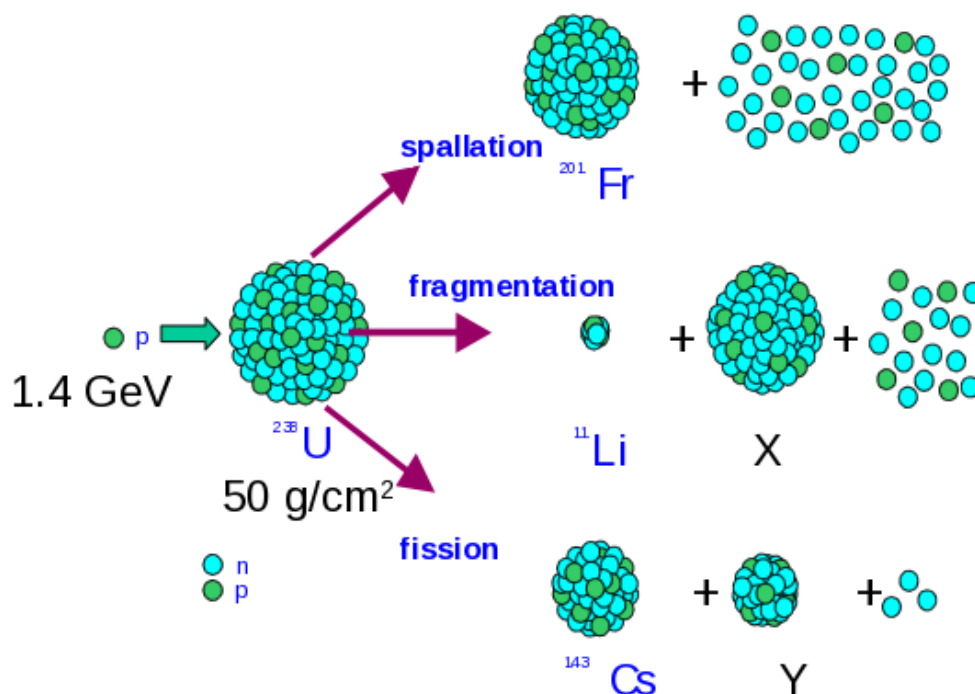


Figure 4.4: Schematic of the spallation, fragmentation and fission reactions used to produce radioactive isotopes at the ISOLDE facility.

Neutral reaction products, having low recoil energies, stop within the target material. The products then diffuse through and effuse out of the target matrix, along a transfer line, and into a hot-cavity ion source of 34 mm length and 3 mm diameter. In order to reduce the release time of the products and adsorption losses, the target and transfer line are kept at a temperature of ≈ 2300 K. Once inside the hot-cavity of the ion source, neutral atoms may be ionised.

4.2.1 RILIS

The Resonance Ionisation Laser Ion Source (RILIS) at ISOLDE is the most commonly used ion source at the ISOLDE facility, with over half of all experiments performed at ISOLDE using it for beam production. It provides a highly selective and efficient way to ionise reaction products created in the ISOLDE target. RILIS can produce ion beams of 35 different chemical elements in 1^+ charge states [59] and more recently has produced beams of Ba in a 2^+ charge state [60].

A multi-step resonant photo-ionisation process exploits the characteristic atomic properties of elements of interest in order to produce an ion beam. Typically a combination of three different tunable lasers is used, with 6 broadly tunable lasers available that can produce wavelengths of light from the ultra violet to the near infra-red range.

Two lasers are used to resonantly excite an atomic electron from the ground, to a first, then to a second excited state. A third laser is then used for the final ionisation step, removing the electron from the atom, leaving an ion in a 1^+ charge state. After atoms of the element of interest are ionised, they are accelerated out of the cavity by an electrostatic potential of 30-60 kV. The extracted ions are then mass separated and delivered to an experimental setup at the end of one of ISOLDE's beam lines.

On average an atom will remain within the hot cavity of the ion source for 0.1ms before diffusing out. In order to maximise the ionisation efficiency of RILIS, the repetition rate of the pulsed laser must be at least 10 kHz. This ensures that each atom is exposed to at least one pulse of laser light, maximising the chance of an interaction between the atom and a photon from the lasers.

Prior to the work performed on At, a significant effort had to be made to develop an ionisation scheme [61]. Very little was known about the atomic structure of At due to the absence of a stable isotope and only trace amounts found in nature (≈ 70 mg found in the outermost mile of the Earth's land area [62]). Only two atomic lines were documented and the ionisation potential was not known. The ionisation schemes used to produce the ion beams during the Au and At experiments can be seen in Figs. 4.5 (a) and (b), respectively.

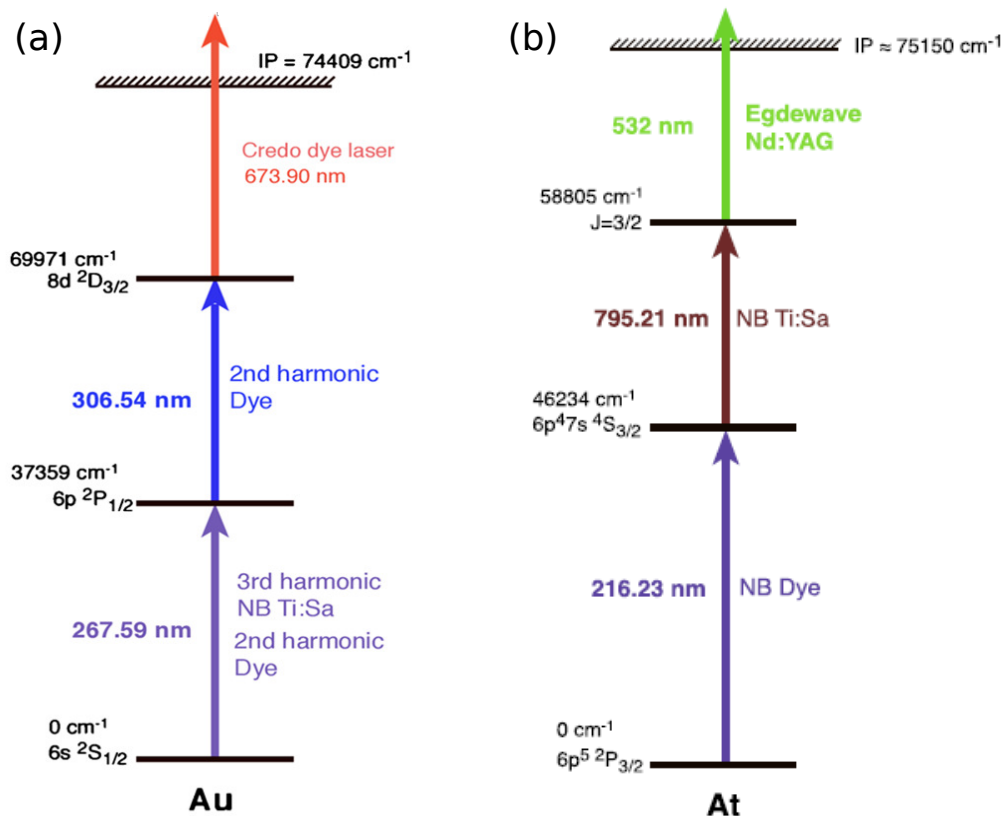


Figure 4.5: The three-step resonant ionisation scheme used to produce (a) the Au beam during the May 2015, IS534 run and (b) the At beam during the September 2014, IS534 run. The first and second step lasers were frequency scanned in the case of the Au and At experiments, respectively.

Due to the hyperfine structure of the electronic energy levels, excitations can only happen at discrete combinations of laser frequencies, where the energy of the photon emitted by the laser matches the energy gap between the different hyperfine levels. By scanning one of the lasers across a range of frequencies in a series of steps and observing when ionisation occurs, the HFS of the isotope can be measured and from this properties of the nucleus can be extracted. During the Au experiment the laser used to make the first step of the resonant ionisation scheme was frequency scanned in order to perform the HFS measurements. In the case of the At experiment the second-step laser was used to perform the scans. More details on the Au and At HFS will be given in their respective chapters.

In addition to the laser-ionised At and Au isotopes, reaction products with low ionisation potentials can be ionised upon contact with the surface of the hot cavity of the ion source. These surface ions are then extracted along with the laser-ionised element of interest, leading to the presence of beam contamination. The majority of these surface-ionised beam contaminants are removed by the ISOLDE mass

separators (discussed in following section). However, the mass separators do not have a high enough resolving power to remove isobars of the isotope of study. This results in the presence of isobaric contamination in the mass-separated beam. For studies of nuclei in the vicinity of the $Z = 82$ shell closure, the main source of beam contamination comes from Fr and Tl, having ionisation potentials of just 4.07 and 6.11 eV, respectively [63]. For the decay studies of ^{178}Au presented in Chapter 5, no appreciable levels of contamination were present due to the low production cross-section of ^{178}Tl , and there being no existing isobar of Fr.

Surface-ionised Fr was the main source of contamination during the experiments on At isotopes discussed in Chapter 6. For ^{217}At and isotopes with $A < 202$, the isobars of Fr are either proton unbound, have a low production cross section, or are too short-lived to be extracted from the ion source, thus, did not pose a problem. For $^{202,218}\text{At}$, the α -decay energy for the Fr isobars were easily separable by the Windmill decay station (discussed in Section 4.3). As for $^{203-211,219}\text{At}$, the Multi Reflection Time-of-Flight Mass Separator device (discussed in Section 4.4.1) was able to remove any isobaric contamination, and so was used to measure the HFS and isotope shifts for these isotopes.

4.2.2 Mass Separation

The ISOLDE facility has two on-line mass separators each with their own target; the General Purpose Separator (GPS) and the High Resolution Separator (HRS). The GPS consists of a single magnet with a resolving power of $M/\Delta M \approx 2400$ [54, 57]. The separator also has two pairs of movable electrostatic deflector plates, allowing for selective production of three ion beams within a maximum acceptance of $\pm 15\%$ of a central mass. The lower- and higher-mass beams are transported to the ISOLDE GLM and GHM beam lines, respectively, and the central-mass beam is transported down the GPS beam line. This makes it possible to perform up to three experimental studies at a time.

The HRS consists of two bending magnets, providing a mass resolution of $M/\Delta M > 5000$. Unlike the GPS, the HRS possesses no deflector plates, only a single beam with specific mass can be produced and is transported down the HRS beam line.

Both the GPS and HRS beam lines then feed into the central beam line via a merging switchyard. This central beam line then feeds into the ISOLDE experimental hall, from where it can be steered to one of a number of experimental stations where a user's setup can be installed. In the case of the IS534 experiments on Au and At, the setups used included the Windmill, the ISOLTRAP MR-ToF and the Faraday Cup, as shown in Fig. 4.3.

4.3 The windmill decay station

In the case of this work, the laser-ionised and mass-separated beam was delivered to the so-called Windmill (WM) decay station, shown in Fig. 4.6. The beam entered the WM through a collimator, passed through the 6 mm central hole of an annular Si detector and was implanted into one of ten carbon foils of 6 mm diameter and $20 \mu\text{g}/\text{cm}^2$ thickness [64]. The foils were mounted upon a wheel that could be rotated after a fixed number of SC, removing long-lived daughter radioactivity from the implantation site to a decay site, and introducing a fresh foil for beam implantation.

Four silicon detectors were placed inside the WM chamber in order to detect and measure the energies of conversion electrons, β and α particles. A $300 \mu\text{m}$ -thick annular surface-barrier with a 6 mm central hole, named Si1, and a $500 \mu\text{m}$ circular surface-barrier, named Si2, were positioned 10.5 mm upstream and 6.5 mm downstream of the foil at the implantation site, respectively. The two detectors gave a combined α -decay detection efficiency of 34%. A second pair of Passivated Implanted Planar Silicon (PIPS) detectors, named Si3 and Si4, were positioned at the decay site to measure any long-lived α and β activity.

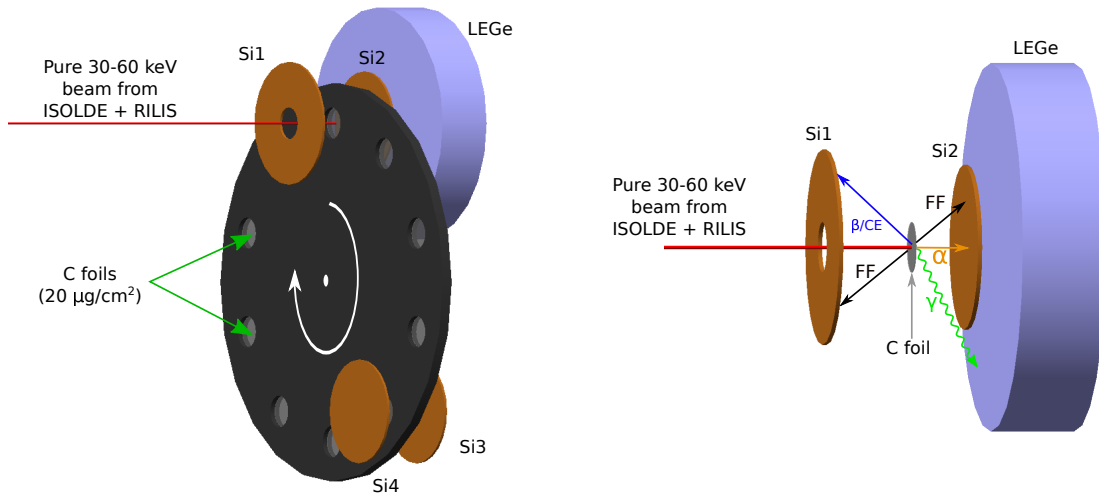


Figure 4.6: Three-dimensional model of the detectors used in the Windmill decay station. Left: positions of the four silicon (brown) and the Low-Energy germanium (LEGe, light blue) detectors relative to the wheel (dark grey) of the Windmill, carbon foils (light grey) and the beam (red). Right: zoomed in view of the detectors and foil at the implantation site and the β /conversion electrons (blue), α particles (orange), γ rays (green) and fission fragments (black) that are measured by the system.

Two germanium detectors were positioned around the WM chamber in order to detect γ rays. The first, Ge1, was a low-energy planar germanium detector and was positioned directly behind Si2. The second was a single-crystal high-purity germanium detector, Ge2, and was positioned 90° relative to the beam direction, to the side of the WM chamber. A schematic displaying the positioning of the Si and Ge detectors relative to each other and the carbon foils can be seen in Fig. 4.6.

4.3.1 Electronics and data acquisition

As mentioned in Section 4.3 the WM wheel was turned after a fixed number of SC lengths. The number of SC per turn of the WM wheel was chosen by the user and depends on the production rate and half life of the isotope being studied. As well as removing long-lived decay products this also provided a logical point to retune the laser frequency during the HFS measurement scans (discussed in the following section).

Digital Gamma Finder (DGF), revision 4C, digital electronic modules from XIA were used for the collection of data [65]. Each module had 4 input channels through which they received and processed electronic signals, and internal clocks to record the time of each signal received. Each “event”, whether it be the detection of radiation inside one of the detectors or a signal from one of the clocks, was given a number of stamps which were then used during the analysis of the data.

- Identification stamp - tells the system which channel and which module the signal was received by allowing for the identification of what type of event was received (i.e. a radiation detection event inside one of the Si or Ge detectors, or a timing event from the pulser (see below) or clocks logic).
- Time stamp - taken from the internal clock of DGF modules and gives the time a signal was received to the precision of 25 ns.
- Energy stamp - proportional to the magnitude of the electronic signal received by the module, the larger the signal, the larger the energy of the event.

During the two experiments 8 modules were used. The energy signals from each detector were first sent through preamplifiers before being sent to one of the modules dedicated to that detector. Of the remaining two cards, one was dedicated to a pulser set to run at 100 Hz. The pulser was used to monitor the total live time of each run as well as the fractional dead time of the system throughout data acquisition. The final card was used to record signals from the clock logic used to control and synchronise the recording of data and the rotation of the WM wheel. The time of the start of a

measurement step within a HFS scan, any proton pulse sent to ISOLDE, the turning of the WM wheel and the end of data recording by the DAQ were all recorded by this card.

The modules were controlled remotely and their internal clocks were synchronised by a dedicated data acquisition computer, using the IGOR software package by wavemetrics [66]. The writing of data from the module buffers to the hard drive of the PC was synchronised using a logic gate in order to minimise dead time from the readouts, as well as to avoid missing any coincident events.

4.4 Scanning the hyperfine structure

In order to measure the HFS of the different isotopes, one transition of the resonant-ionisation scheme is scanned using a laser that operates in a ‘high-resolution’ narrowband (NB) mode. In this mode, the linewidth of the NB laser is ≈ 1 GHz [56], matching the resolution limit set by the 1-1.5 GHz Doppler broadening of the atomic transitions. The Doppler broadening is due to a velocity distribution of atoms within the hot-cavity ion source. The other transitions of the photoionisation scheme are performed by separate lasers that operate in a fixed-frequency broadband (BB) mode, optimised such that they give the maximum ionisation efficiency. The BB lasers have a linewidth of 10-20 GHz, covering the full widths of the HFS for all isotopes of a given element. This ensures that all isotopes and isomers are ionised with the same efficiency.

The frequency of the light produced by the NB laser is changed in a series of discrete steps. At the beginning of a step the NB laser is tuned by the tilting two etalons in order to select a fixed frequency [67]. Once frequency stabilised, the implantation of beam to the Windmill decay station commences, and the recording of data begins. During each step, the frequency of the NB laser light is monitored using a precision wavemeter, and the measured average is taken as the laser frequency for that step. After a fixed period of time, the acquisition of data stops and the lasers are tuned to a new frequency. During this tuning time, the wheel of the windmill is rotated in order to introduce a fresh foil to the implantation site. This process is repeated until the full range of the HFS of the isotope of interest has been covered by the scan. The start and end data recording during each step in the scan, and the movement of the wheel before the next step are controlled by the signals from a number of digital clocks that are combined with those from the CERN PSB in an electronic logic system.

The range of frequencies the HFS covers is determined by preliminary measure-

ments which scan an extended range of frequencies using large step sizes in order to ensure no resonances are missed. It was during one of these extended measurements that the HFS of the second isomer in ^{178}Au (presented in Chapter 5) was discovered, at somewhat of a surprise to the experimentalists.

The Windmill setup was used to measure the HFS of short-lived α -decaying isotopes and isomers of At. The number of α decays or γ transitions were measured per laser step, thus giving a measurement of ionisation efficiency at a certain setting of laser frequency. The characteristic radiation, unique to a specific isomer, makes decay-tagged laser-spectroscopy an extremely selective method for investigating the HFS of different states within the same nucleus. By gating on either the characteristic α decays or γ transitions measured by the Windmill decay station, it is possible to extract the HFS of multiple isomers during a single laser scan. An example of such a study is displayed in Fig. 4.7. The plot shows the number of counts of singles α decays as a function of laser wavenumber setting, for a scan of ^{200}At . The HFS of the three different isomers present in ^{200}At can be individually investigated due to the ability to make clean gating conditions on their respective α decay energies.

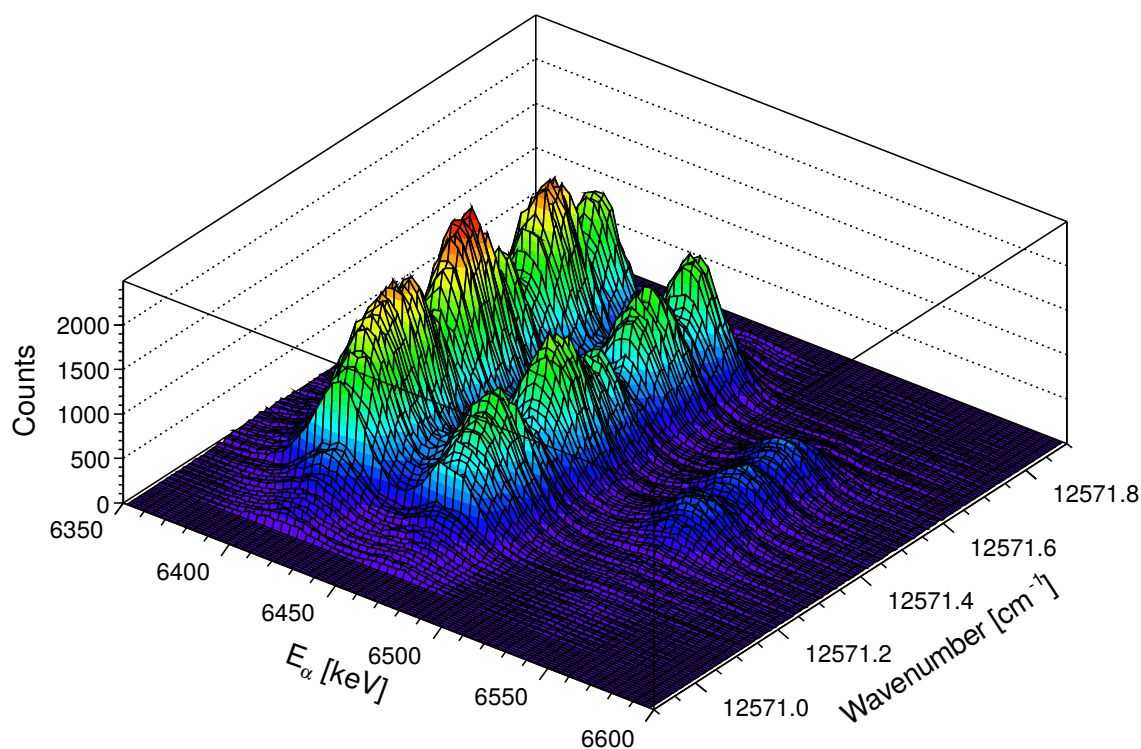


Figure 4.7: Surface plot of the α -decay energy measured in the Windmill system, versus the laser wavenumber recorded at the time the α particle was detected for ^{200}At . Three ridges can be seen, corresponding to three different α decays, from three different states in ^{200}At . The different structures of the three ridges are a direct result of the difference in HFS, due to the different structures of the three nuclear isomers.

4.4.1 The ISOLTRAP MR-ToF device

In cases where the nucleus of interest has no α decay, has a long lifetime, or there are high levels of isobaric contamination present in the beam, the Multi-Reflection Time-of-Flight Mass Spectrometer (MR-ToF MS) of ISOLTRAP was used. A brief overview of the principles of how the MR-ToF MS operates is given below. For further details on the device we refer to Refs. [68, 69].

First, the mass-separated beam enters the Radio Frequency Quadrupole cooler-buncher (RFQ), which slows and bunches the ions of the beam. The ions are then injected into the 460-mm long cavity of the MR-ToF MS device. Two 160-mm long, coaxial electrostatic mirrors are positioned at either end of the cavity, with central apertures allowing the entrance of the mixed beam, and exit of the mass-separated ion beam. The whole device has a length of ≈ 0.8 m. Ions are reflected back and forth thousands of times between these mirrors, effectively giving them a long flight path. This produces a temporal separation of species due to differences in their respective masses. The final result is a mass-resolving power of $\sim 2 \times 10^5$, with the mass separating process taking ~ 30 ms. A schematic of the operation principles of the device is shown in Fig. 4.8.

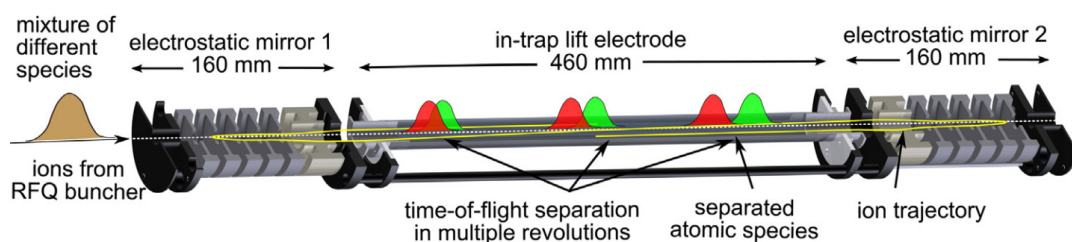


Figure 4.8: Schematic of the operation of the MR-ToF MS device, taken from [69].

Once mass separated, a high-time resolution electrical deflector is used to select the isotopes of interest. This deflector allows the desired species to exit through the aperture of the exit mirror, and rejects contaminants by reflecting them back into the MR-ToF cavity. Once the isotopes of interest have exited the cavity, a multichannel-plate detector is used to count the number of ions.

Decay studies of ^{178}Au

5.1 Identification and separation of different isomers

As mentioned in Section 1.1, previous decay studies of ^{178}Au identified just one α -decaying state [11, 12, 70]. However, β -decay feeding from ^{178}Au to the states with $I = 2$ and 4, as well as to $I = 8$ states in ^{178}Pt was also observed, in the study of Ref. [13]. This provided the first indication for the presence of two α -/ β -decaying states in ^{178}Au , with possible spins of $I = 2-4$, and $I = 7-8$.

The first direct confirmation of these two states in ^{178}Au was made during the IS534 experiment - a collaboration between the Windmill and ISOLTRAP groups. This was achieved based on the HFS measurements made for the two states, shown in Fig. 5.1. The large difference between the HFS of the ground and isomeric states made possible the production of isomerically pure beams, allowing independent studies to be made upon the two states. The ISOLTRAP Penning trap [71] was used to perform mass measurements, which were used to identify which was the ground state (^{178g}Au), and which was the isomeric (^{178m}Au) state.

Decay studies were performed upon $^{178g,m}\text{Au}$ using the Windmill decay station (see Section 4.3). Dedicated runs were made in order to measure the half-lives, branching ratios and decay properties of the two states, the results of which will be presented and discussed in this chapter. Throughout the decay studies, laser settings of 12453.38 cm^{-1} , and 12452.18 cm^{-1} were used to produce isomerically pure beams of the ground and isomeric states in ^{178}Au , respectively. The results of the mass measurements showed ^{178m}Au to have an excitation energy of 188(14) keV relative to ^{178g}Au . The details of the mass measurements will not be presented in this work, but will be discussed in a forthcoming publication [72].

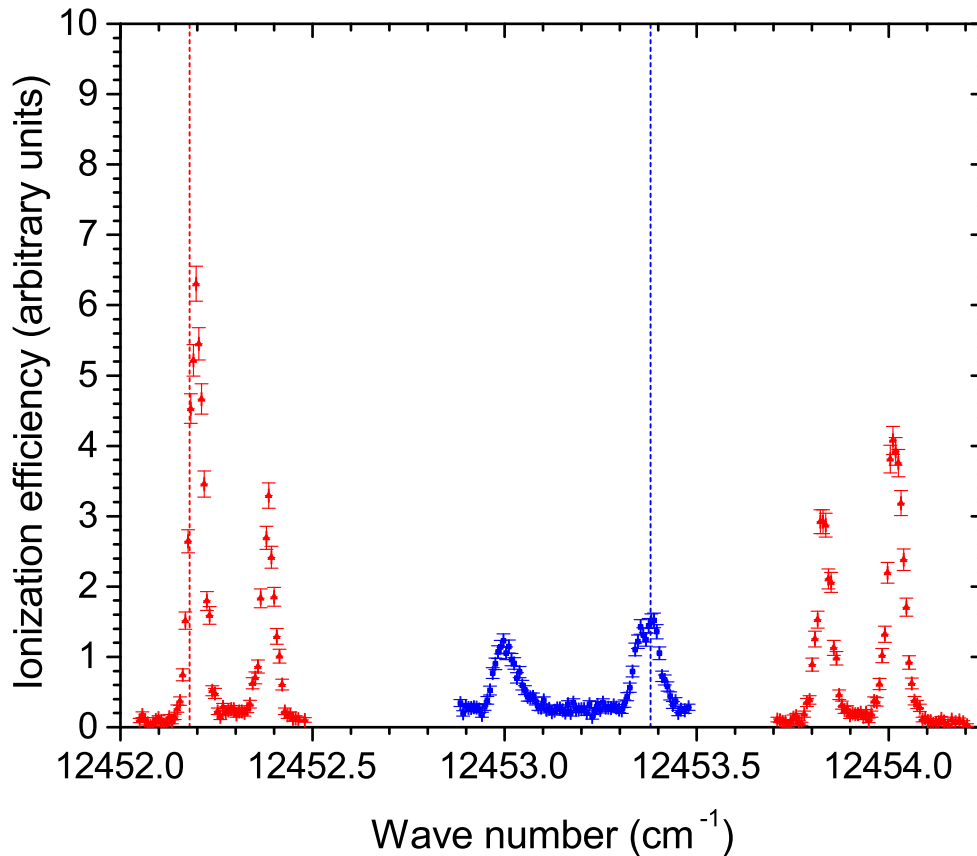


Figure 5.1: The measured HFS of the ground (blue) and isomeric (red) states of ^{178}Au .

5.2 Calibration of detectors

5.2.1 Silicon detectors

The silicon detectors were calibrated using the well-known α -decay energies of ^{178}Pt [73], the β -decay daughter of ^{178}Au , and ^{198}At [74, 75, 76], the data for which were taken during a neighbouring run. The results for the calibration of the silicon detectors are shown in Fig. 5.2.

The evaluation of the α -electron (α -e) summing discussed in Section 5.3.2, due to the simultaneous deposition of energy of the α particle and subsequent conversion electrons within the Si detectors, requires the positions of the detectors to be well known, relative to the implantation foil. These were determined by comparing the fraction of α decays from a 50(1) Bq ^{241}Am source that were measured by Si1 and Si2, to their respective solid angle coverages at varying distances from the foil (shown in Fig. 5.3). From this analysis, Si1 and Si2 were found to be positioned 10.5(10) and 6.5(10) mm away from the implantation foil, respectively.

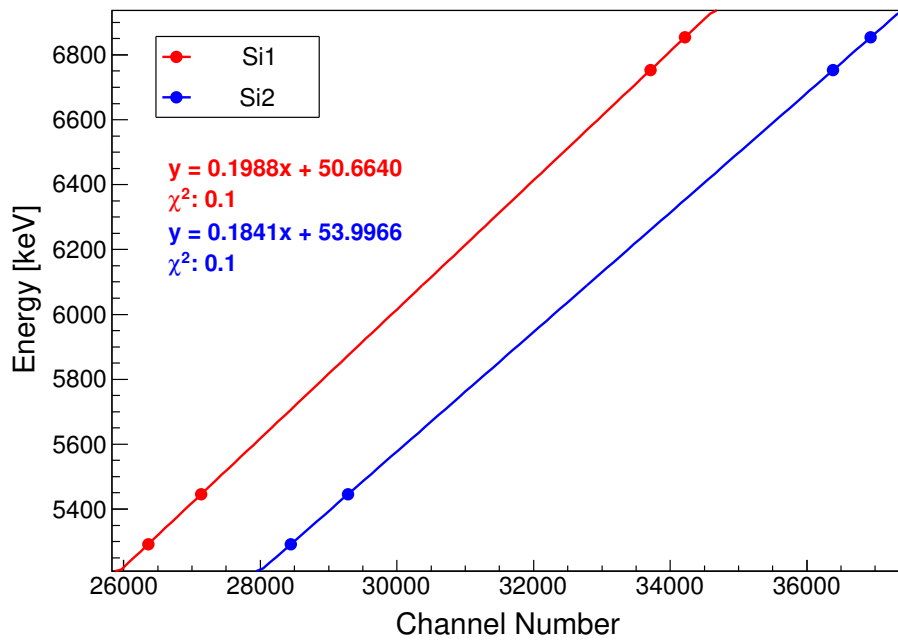


Figure 5.2: Energy calibration for the Si1 (red) and Si2 (blue) detectors, using the α decays of ^{178}Pt , $E_\alpha = 5291(4)$ and $5446(3)$ keV [73], and ^{198}At , $E_\alpha = 6753(4)$ and $6854(4)$ keV [74, 75, 76]. The data are fitted with linear functions.

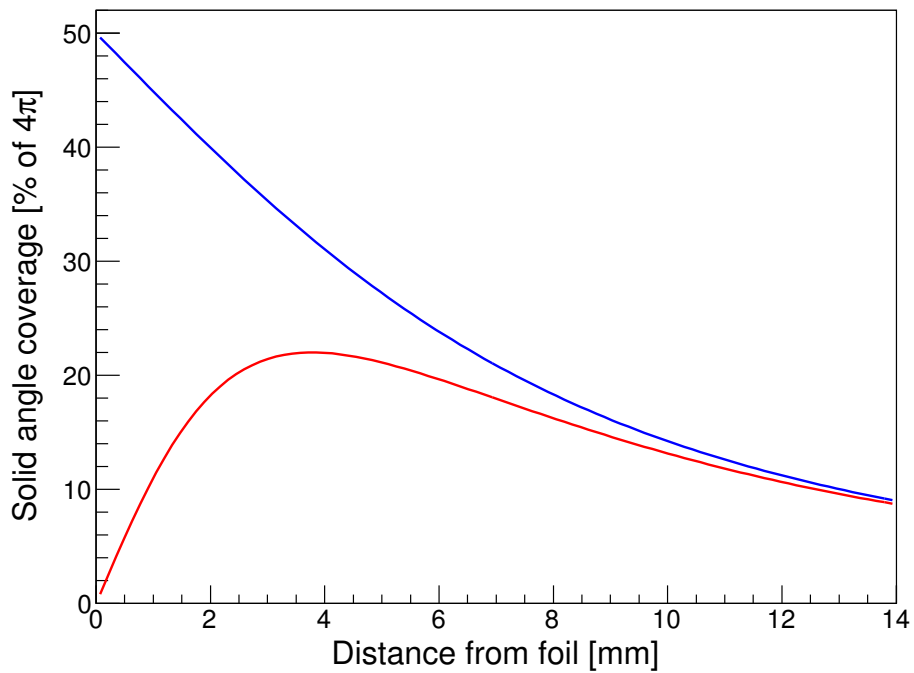


Figure 5.3: The solid angle coverage of Si1 (red) and Si2 (blue) as a function of distance from the implantation foil.

5.2.2 Germanium detectors

The germanium detector was energy and efficiency calibrated using ^{60}Co (0.716 kBq), ^{133}Ba (6.686 kBq), ^{152}Eu (7.953 kBq) and ^{137}Cs (18.519 kBq) sources [34]. The top panel of Fig. 5.5 shows the energy of a detected γ ray as a function of the channel number, fitted with a linear relationship. The bottom panel of Fig. 5.5 shows the absolute detection efficiency as a function of the energy of γ rays from the aforementioned calibration sources. The data are fitted with a crystal ball function - a Gaussian plus tail function that will also be used for fitting the α -decay peaks in the following sections (see Refs. [77, 78, 79] for more details).

5.2.3 Prompt timing gates

Before final analysis of the α - γ coincidence data it was necessary to define a prompt time gate between the detection time of an α particle in a silicon detector, and a γ ray measured in the germanium detector. The gate was set such that as many time-random coincidences as possible were removed, whilst keeping the true coincidence events within the data.

This was achieved by plotting the time distribution of the 5291(4)-158.6(1) keV α - γ coincidences belonging to the fine structure of ^{178}Pt [80]. The results are shown in Fig. 5.4, based on which a prompt timing condition of $20 \text{ ns} < \Delta t < 230 \text{ ns}$ was used for investigating the α - γ coincidences in the following discussion.

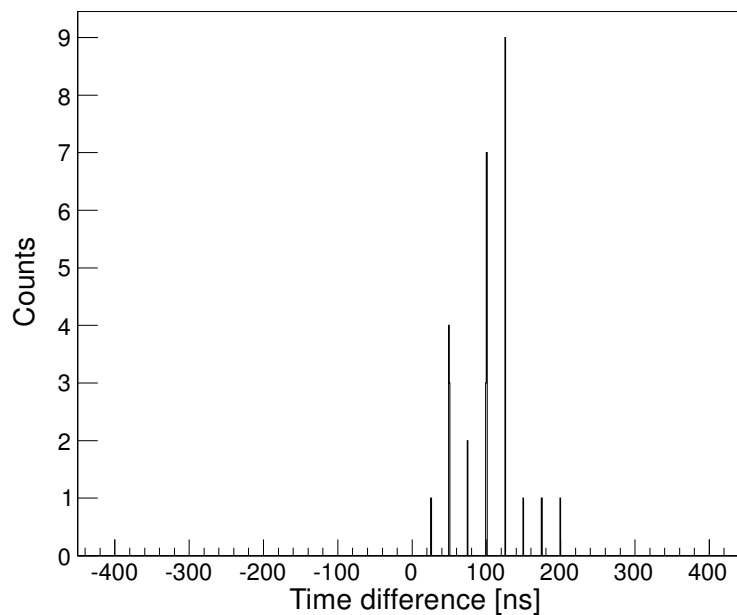


Figure 5.4: The difference between the time of detection for an α particle and a γ ray belonging to the 5291-158.6 keV fine-structure decay of ^{178}Pt .

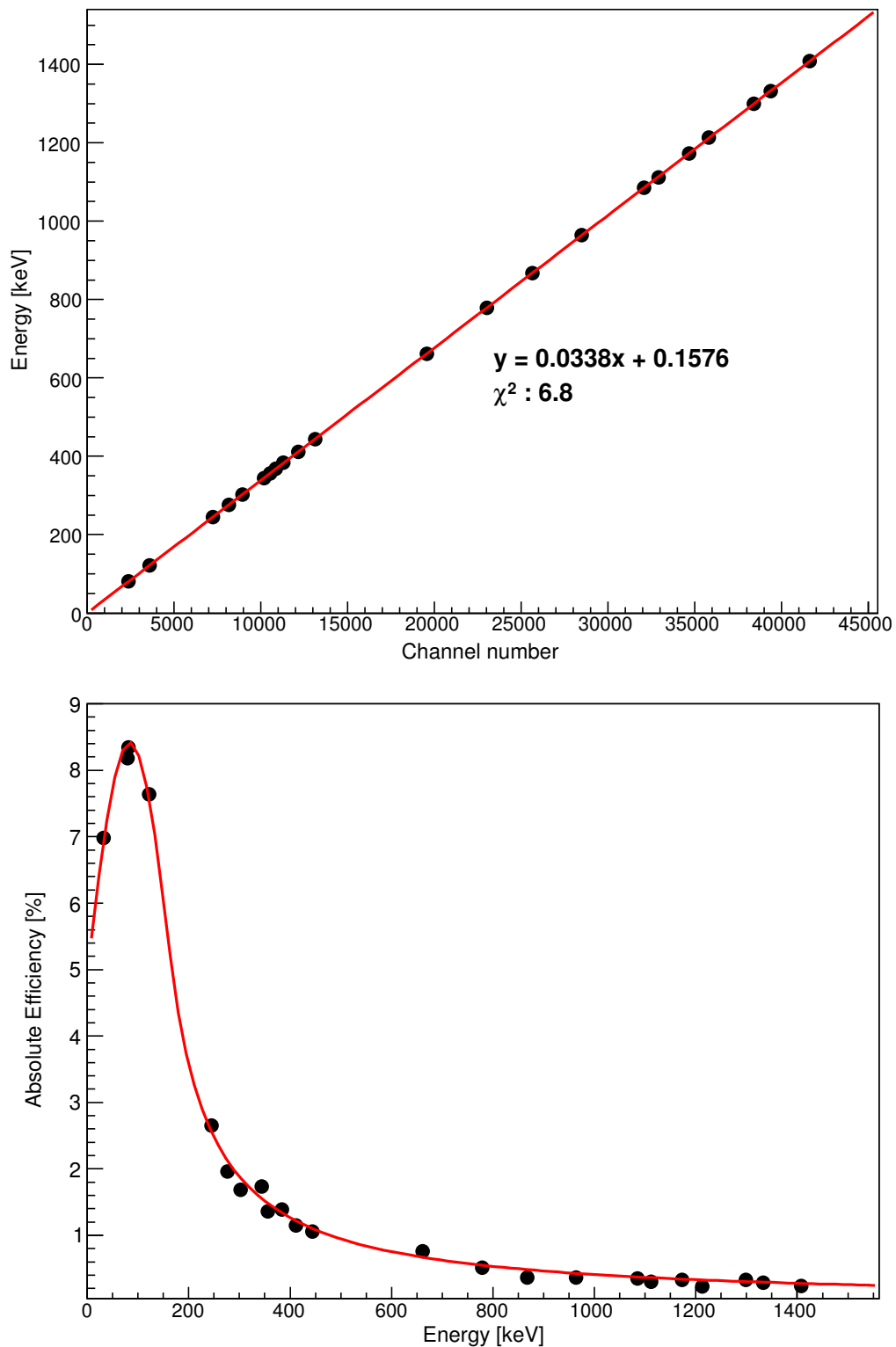


Figure 5.5: Calibration of the germanium detector. The top panel shows the energy calibration, with the energy of the detected γ ray as a function of the channel number, fitted with a linear relationship. The bottom panel displays the absolute detection efficiency of the LEGe detector as a function of energy, fitted with a crystal ball function.

5.3 Decay analysis

The decay data for the ground and isomeric states in ^{178}Au are shown in left- and right-hand side panels of Fig. 5.6, respectively. In these figures, panels (a) and (b) show the combined singles α -decay spectra measured in Si1 and Si2 of the Windmill station, and panels (c) and (d) display the α - γ coincidence matrices. Panels (e) and (f) are the projections upon the E_γ axes of the aforementioned coincidence matrices, made for the E_α regions between the dashed vertical red lines shown in panels (c) and (d). The solid horizontal red lines in panels (c) and (d) point to groups of α - γ coincidences discussed in the following sections. Figures 5.7 and 5.10 show the projections on the E_α axis for the groups of α - γ coincidences that belong to the fine-structure decay of the ground and isomeric states in ^{178}Au , respectively.

It is worth noting the cleanliness of the spectra displayed in Fig. 5.6, due to the high purity of the beams of ^{178}Au produced at ISOLDE. Only decays belonging to ^{178}Au and its β -decay daughter, ^{178}Pt , are seen in the plots.

5.3.1 Singles alpha decay

For ^{178g}Au , two high intensity peaks at 5843(10) and 5922(5) keV are evident in Fig. 5.6 (a), along with a third low-intensity peak at 5750(15) keV. In comparison, the spectrum for ^{178m}Au shown in Fig. 5.6 (b) displays three high-intensity peaks, at 5839(10), 5925(7) and 5973(7) keV, with an additional two low-intensity peaks at 5521(10) and 5571(10) keV. The differences between these two spectra alone indicates the presence of two different α -decaying states in ^{178}Au . The peaks at 5291(5) and 5446(5) keV in both spectra are due to the α decay of ^{178}Pt , the daughter nucleus of the β^+ /EC decay of ^{178}Au . As will be shown in the following discussions, there are additional fine-structure decays contributing to these observed peaks, which will be identified by the analysis of the data for α - γ coincidences.

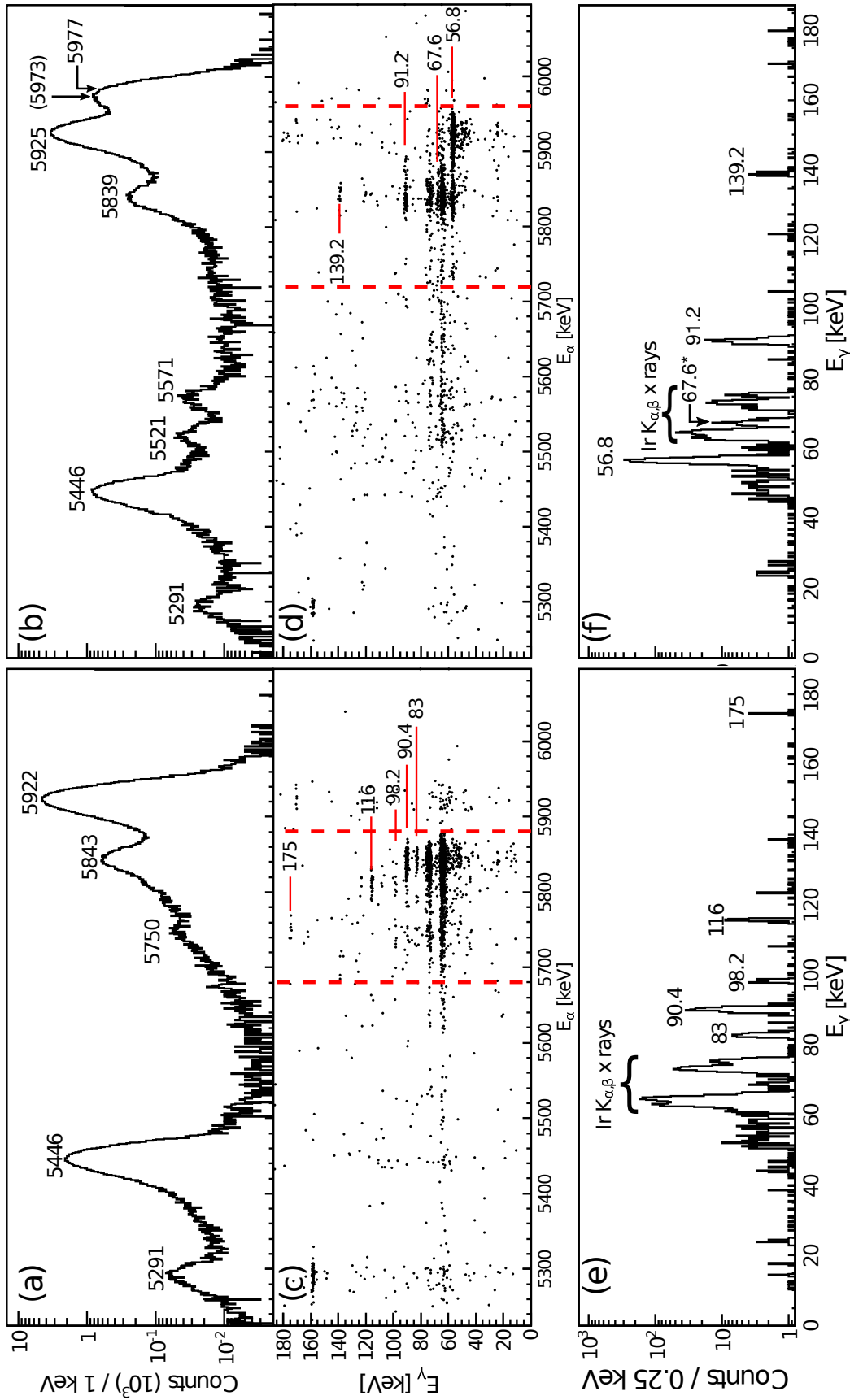


Figure 5.6: Singles α -decay and α - γ coincidence spectra for ^{178g}Au (left-hand side panels), and ^{178m}Au (right-hand side panels). Panels (a) and (b) are the single α -decay spectrum measured in Si1 + Si2, (c) and (d) are the E_α - E_γ coincidence matrices with a 20 ns $< \Delta t < 230$ ns timing condition, and (e) and (f) are the projections upon the E_γ axis for the α -decay energy regions indicated by the dashed red lines in panels (c) and (d). *The 67.6 keV peak at 67.6 keV is a γ -ray transition in ^{174}Ir , not an Ir $K_{\alpha,\beta}$ x ray.

Results for the ground state

Several prominent groups of α - γ coincidences can be seen in Figs. 5.6 (c) and (e): 5843(10)-83.0(3) keV, 5840(10)-90.4(3) keV, 5811(10)-116.0(3) keV and 5753(15)-175(1) keV. Due to the large intensity of the 170 keV $2_1^+ \rightarrow 0_1^+$ γ -ray transition in ^{178}Pt , a small number of time random coincidences at 5922-170 keV can be seen in Fig. 5.6 (c).

In addition to the main α - γ coincidence groups, a number of other groups with low statistics can be seen in Figs. 5.6 (e) and 5.7. A group at 5753(20)-83.0(3) keV is visible in Fig. 5.7 (a), and two at 5740(20)-98.2(3) keV and 5810(20)-98.2(3) keV in Fig. 5.7 (c). The $E_\alpha \pm 20$ keV uncertainties stem from the low number of counts in these groups.

Should these α - γ coincidences be components of the fine-structure decay of the same state, then their total Q-values, $Q_{\alpha,tot}$, should be in agreement with the $Q_\alpha = 6058(5)$ keV of the 5922 keV α decay. The value of $Q_{\alpha,tot}$ is defined as

$$Q_{\alpha,tot} = Q_\alpha + \sum_{i=1}^n E_\gamma(i), \quad (5.1)$$

where the last term represents the sum of the energies of all γ rays belonging to a cascade with n transitions, following an α decay.

The calculated $Q_{\alpha,tot}$ values of these coincidences are displayed in Table 5.1. The 5811-116 keV and 5753-175 keV groups are in agreement with the $Q_{\alpha,tot}$ of the 5922 keV α decay. Therefore, these α decays, followed by single-step γ -ray transitions, are assigned to the fine-structure decay of ^{178g}Au , as shown in Fig. 5.8.

Table 5.1: Energies for α decays (E_α) and γ transitions (E_γ) in coincidence with one another and the calculated total Q-values ($Q_{\alpha,tot}$), for ^{178g}Au .

E_α [keV]	E_γ [keV]	$Q_{\alpha,tot}$ [keV]
5922(5)	0	6058(5)
5811(10)	116.0(3)	6061(10)
5753(15)	175.0(10)	6060(15)
5843(10)	83.0(3)	6060(10)
5840(10)	90.4(3)	6065(10)
5753(20)	83.0(3)	5968(20)
5810(20)	98.2(3)	6042(20)
5740(20)	98.2(3)	5970(20)

The $Q_{\alpha,tot}$ values of the 5840-90.4 keV and 5843-83 keV groups are within error of

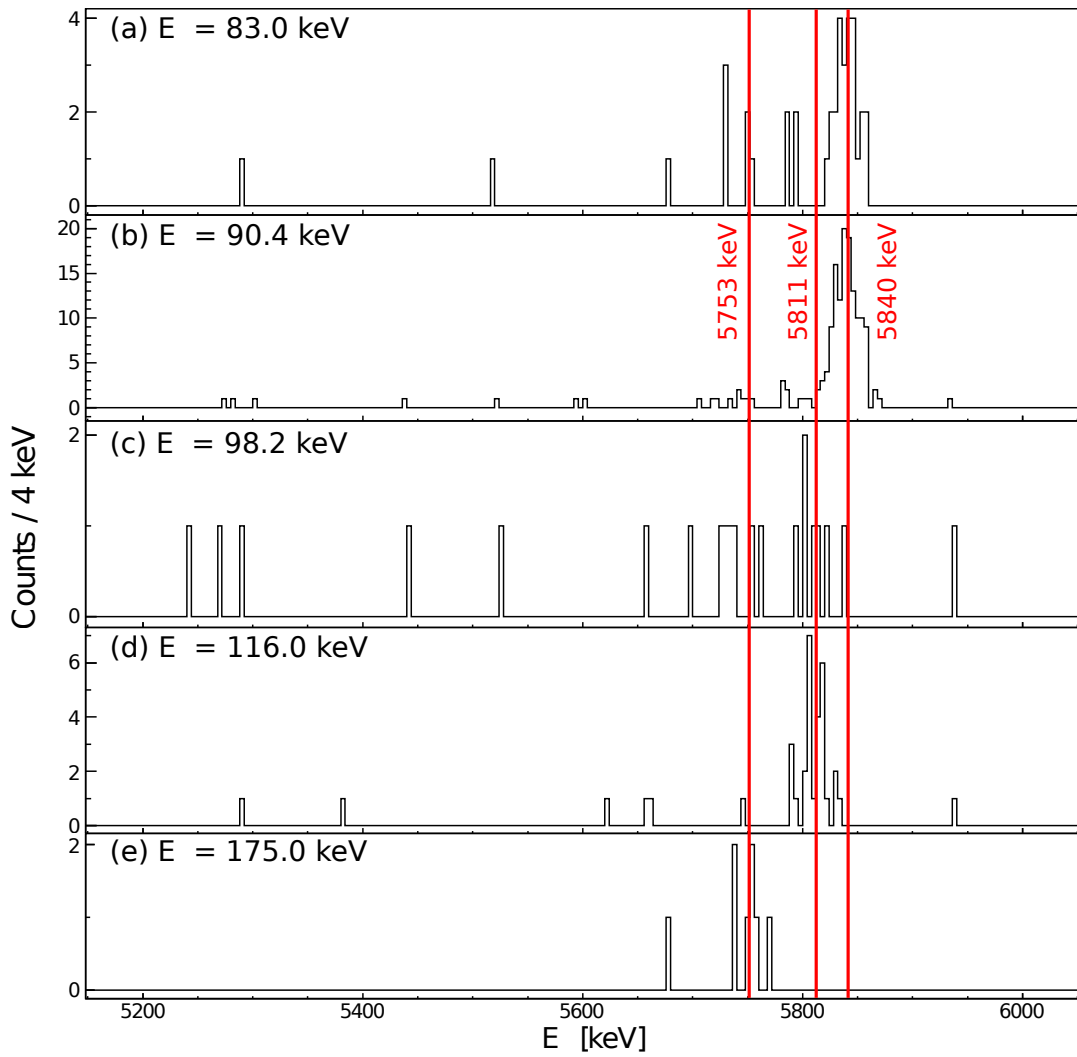


Figure 5.7: Projections on the E_α axis from the α - γ coincidence matrix of ^{178g}Au shown in Fig. 5.6, for the $E_\gamma =$ (a) 83.0, (b) 90.4, (c) 98.2, (d) 116.0 and (e) 175.0 keV groups. The vertical red lines represent α -decay energies for different components of the ^{178g}Au fine-structure decay, shown in Fig. 5.8. Gating conditions of $E_\gamma \pm 1$ keV were used to make these projections.

one another, as well as that of the 5922 keV singles α decay. One possible explanation for this is that both the 90.4 and 83 keV γ -ray transitions originate from the same state in ^{174}Ir , populated by the same α decay of ^{178g}Au . This would require the existence of a 7 keV transition following the 83 keV decay to account for the difference in the $Q_{\alpha, tot}$ values, however, this is not observed in the data. An alternative explanation could be that the two γ transitions follow two α decays, with an energy difference of a few keV. The energies of the two α decays would be so close that they cannot be resolved within the resolution of the Windmill silicon detectors. The second of the two scenarios is drawn in Fig. 5.8.

The 5810-98.2 keV group most likely has the same α decay as that of the 5811-116 keV fine-structure decay. This means that there is 17.8 keV of energy missing from the full-energy fine-structure decay, when comparing the γ -ray energies of a 5811-98.2 keV and a 5811-116 keV group. Similarly, the α decays of the 5753-83 keV and 5740-98.2 keV groups are most probably the same as that of the 5753-175 keV fine-structure decay. This would lead to 92 keV of energy missing from the 5753-83 keV group, and 76.8 keV from a 5753-98.2 keV decay path.

The missing 92 keV of energy from the 5753-83 keV decay can be placed between the 175 keV and 83 keV levels in ^{174g}Ir , as shown in Fig. 5.9. However, the placement of the 98.2 keV transition is uncertain, as it is unclear whether the missing 17.8 keV of energy precedes or follows it. This leads to two possible scenarios, labelled scenario 1 and scenario 2 in Fig. 5.9. In scenario 1, the 116 keV level in ^{174}Ir decays via the emission of a 98.2 keV γ ray, followed by a 17.8 keV γ -ray transition to the ground state. In this scenario the 5753-98.2 keV group would result from a 59 keV transition between the 175 keV and 116 keV levels in ^{174}Ir .

In scenario 2, the 98.2 keV transition is preceded by a 17.8 keV transition in a γ -ray cascade from the 116 keV level to the ground state in ^{174}Ir . The 5753-98.2 keV group can either result from feeding to the 116 keV level by a 59 keV γ -ray from the 175 keV state, as in scenario 1, or by a 76.8 keV γ -ray transition between the 175 keV and a 98 keV level.

In the case of scenario 1, a 5753-116 keV α - γ coincidence group would be expected in the data. There is only one count in Fig. 5.7 (d) that could be attributed to such a group. On the other hand, scenario 2 does not require such a transition and so may be the preferable option, however, the available statistics are too low to choose either scenario with certainty.

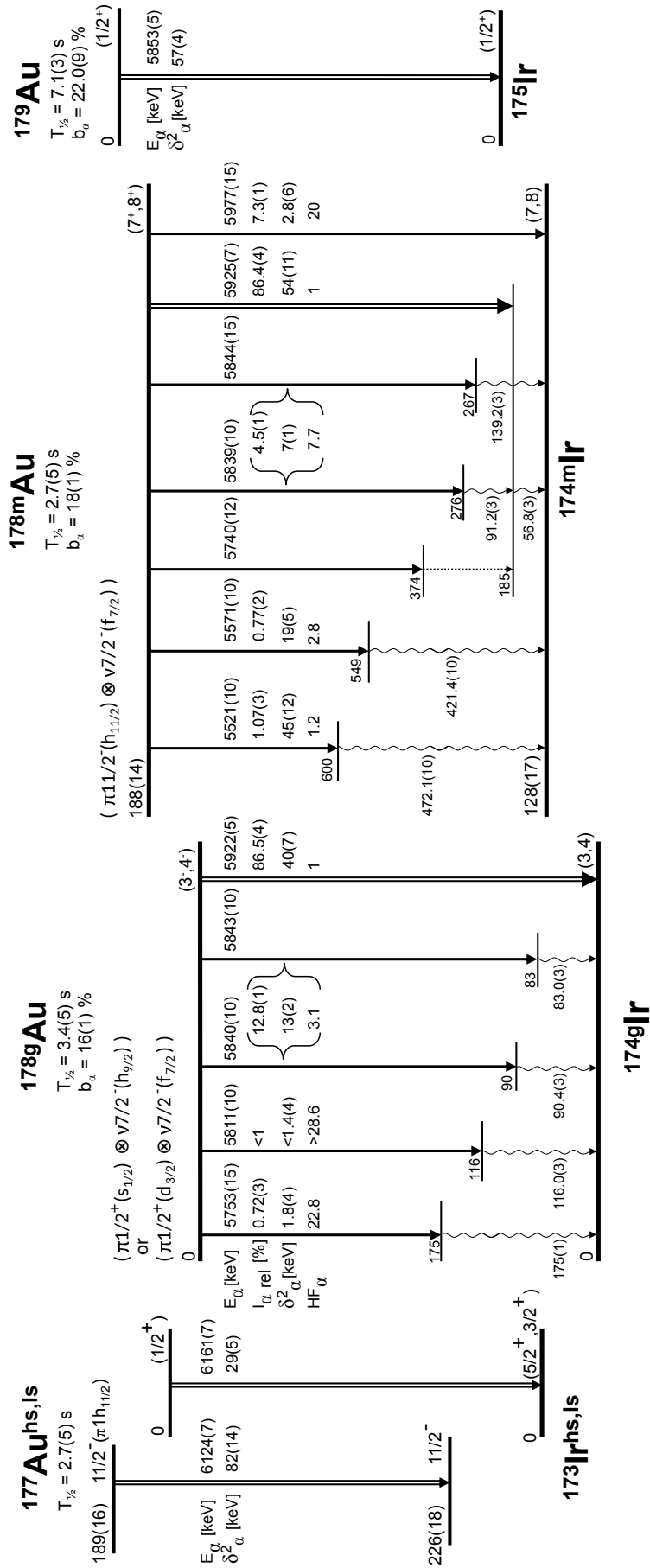


Figure 5.8: Decay scheme for $^{178g,m}\text{Au}$, deduced in this work. Shown are the α -decay energies, E_α , relative intensities, $I_{\alpha,rel}$, reduced α -decay widths, δ_α^2 , and hindrance factors, HF_α . The values of HF_α were calculated for the ground and isomeric state fine-structure decays relative to the strongest 5922 keV and 5925 keV α decays, respectively, for which $\text{HF}_\alpha = 1$ was assumed. The α -decay schemes for the neighbouring ^{177}Au [81] and ^{179}Au [82] isotopes are also provided.

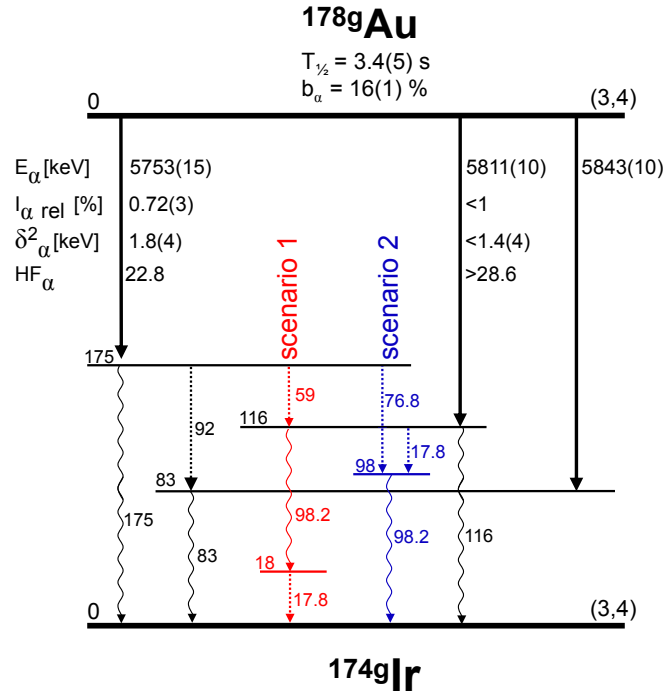


Figure 5.9: The two possible options for placing the 98.2 keV γ -ray transition (see text), scenario 1 (red), and scenario 2 (blue), in ^{174}Ir

Results for the isomeric state

Seven groups of α - γ coincidences were identified in Figs. 5.6 (d) and (f): 5740(15)-56.8(3) keV, 5839(10)-91.2(3) keV, 5839(10)-67.6(3) keV, 5839(10)-56.8(3) keV, 5844(15)-139.2(3) keV and 5925(7)-56.8(3) keV. The calculated $Q_{\alpha, tot}$ values for these groups are shown in Table 5.2.

In addition to the above, the two low-intensity peaks at $E_{\alpha} = 5521$ and 5571 keV seen in Fig. 5.6 (b), were observed in coincidence with γ transitions with $E_{\gamma} = 421.4(5)$ and 472.1(5) keV, respectively. The spectra for the α decays in coincidence with these two γ rays are shown in Figs. 5.10 (e) and (f), but contain low statistics. In Fig. 5.10 (e) The 421.4 keV transition is seen to be in coincidence with 4 counts at $E_{\alpha} \approx 5571$ keV, and 2 counts at $E_{\alpha} \approx 5521$ keV. Four counts at $E_{\alpha} \approx 5521$ keV are seen in coincidence with the 472.1 keV γ -ray transition, in Fig. 5.10 (f).

In passing we mention that a follow-up experiment, JR121 [83], that was inspired by the ISOLDE study, was performed on ^{178}Au at the accelerator laboratory at the University of Jyväskylä (JYFL). The JYFL experiment used the JuroGam II [84] - RITU [85] - GREAT [86] setups and employed the recoil-decay tagging method [87] in order to study the γ decay of excited states, and the subsequent α decay of $^{178g,m}\text{Au}$. The data from the JYFL experiment contains ~ 10 times the statistics of the ISOLDE study, and confirms the presence of the 5521-472.1 keV and 5571-421.4 keV α - γ coincidence

groups, each having ~ 40 α - γ events. An α - γ coincidence group at 5521-421.4 keV was not observed in the JYFL data. Therefore, the 2 counts seen at $E_\alpha \approx 5521$ keV in Fig. 5.10 (e) are attributed to coincidences with the low-energy tail events of the 5571 keV α decay, and the 5521-421.4 keV group excluded from the following analysis.

The 5925-56.8 keV group establishes a state at 185 keV (56.8 keV above the isomer in ^{174}Ir), fed to by the ^{178m}Au 5925 keV α decay, as shown in Fig. 5.8. In the following discussion of the $Q_{\alpha,tot}$ values belonging to the aforementioned α - γ coincidence groups, the different decay paths will be compared to that of $Q_{\alpha,tot} = 6118(7)$ keV of the 5925-56.8 keV group. The reason for this is twofold; firstly, this is the most intense α decay of ^{178m}Au , and is followed by a single-step 56.8 keV γ -ray transition (see Fig. 5.8). Thus, the α -decay energy for this α - γ group, taken from Fig. 5.10 (a), is not affected by α -e summing (see below); secondly, as will be shown in the following discussion and Section 5.3.2, a significant component of the peak observed at $E_\alpha = 5973$ keV in Fig. 5.6 (b) is due to α -conversion electron (α -e) summing within the Si detectors. This results in a large error estimate for the α -decay energy, as the subtraction of the α -e summing results in a significant reduction in intensity, and a shift in peak centroid to $E_\alpha = 5977(15)$ keV (see details in Section 5.3.2). Therefore, it is safer to compare $Q_{\alpha,tot}$ values of the different α - γ coincidence groups to that of the 5925-56.8 keV group.

The excitation energy of the isomeric state in ^{174}Ir (^{174m}Ir), $E_x(^{174m}\text{Ir})$, was calculated by comparing the excitation energy of ^{178m}Au , the $Q_{\alpha,tot} = 6118$ keV of the ^{178m}Au fine-structure decay, and the $Q_{\alpha,tot} = 6058$ keV of the 5922 keV ^{178g}Au , ground state-to-ground state decay, such that

$$E_x(^{174m}\text{Ir}) = Q_{\alpha,tot}(^{178g}\text{Au}) + E_x(^{178m}\text{Au}) - Q_{\alpha,tot}(^{178m}\text{Au}). \quad (5.2)$$

This yielded a value of $E_x(^{174m}\text{Ir}) = 128(17)$ keV, as shown in Fig. 5.8.

The $Q_{\alpha,tot}$ values of 6118(15) keV for the 5844-139.2 and 6118(7) keV for the 5925-56.8 keV groups are in agreement with one another. This establishes an excited state at 267 keV (139 keV above ^{174m}Ir , see Fig. 5.8).

The 5521-472.1 and 5571-421.4 keV groups both have $Q_{\alpha,tot}$ values of 6120(10) keV. This is in good experimental agreement with the $Q_{\alpha,tot}$ values belonging to the other α - γ coincidence groups, shown in Table 5.2. Thus, these two groups are assigned as components of the fine-structure decay of ^{178m}Au , and states with excitation energies of 600 and 549 keV (472 and 421 keV above ^{174m}Ir) are established in Fig. 5.8. We note here that it is unusual to see such intense fine-structure components feeding to states at such high excitation energies, relative to the strongest decay path. A further, dedicated discussion of these two peaks is given in Section 5.6.

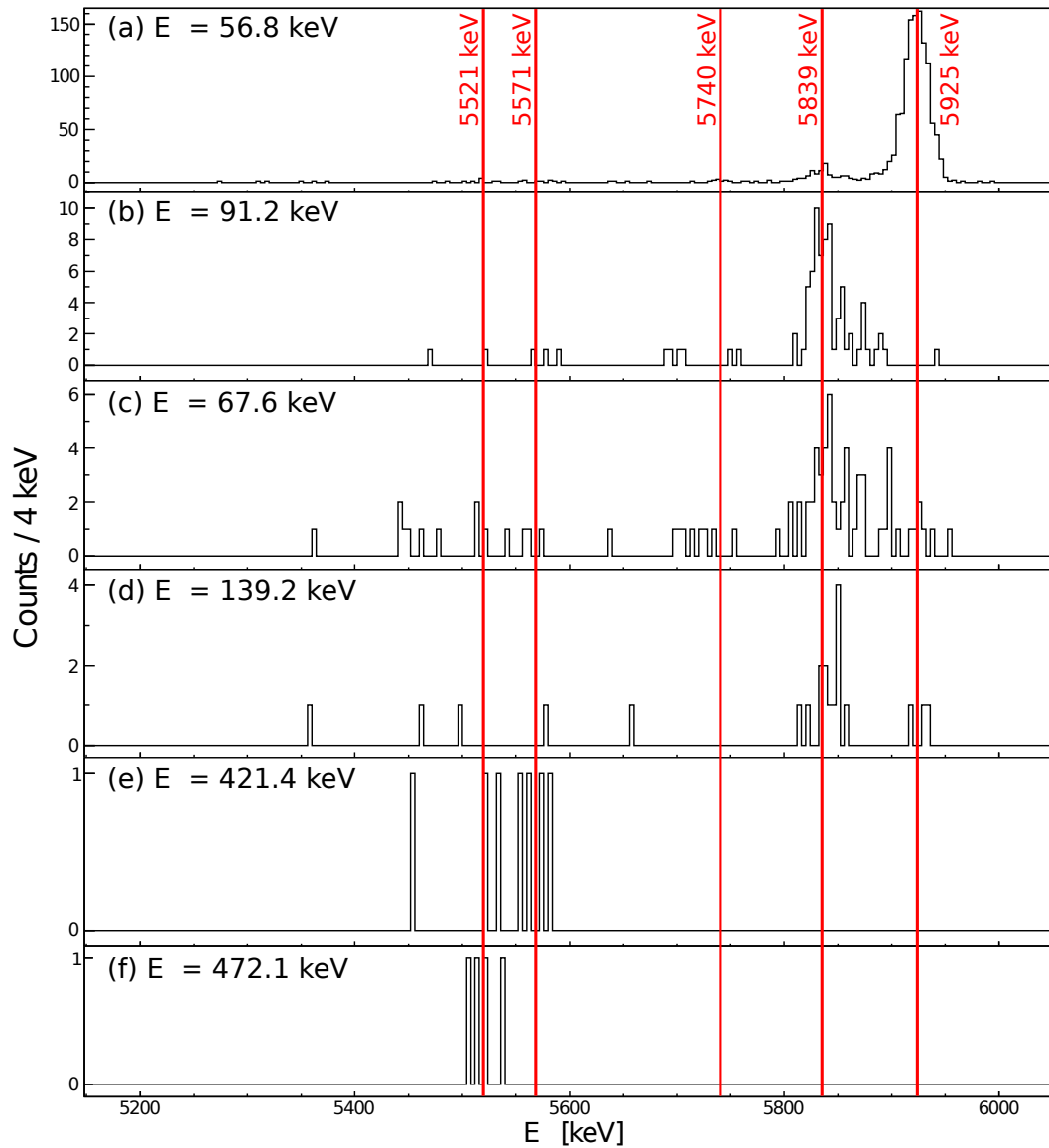


Figure 5.10: Projections on the E_α axis from the α - γ coincidence matrix of ^{178m}Au shown in Fig. 5.6, for $E_\gamma =$ (a) 56.8, (b) 91.2, (c) 67.6, (d) 139.2, (e) 421.4 and (f) 472.1 keV. The vertical red lines represent α -decay energies for different components of the ^{178m}Au fine-structure decay, shown in Fig. 5.8. Gating conditions of $E_\gamma \pm 1$ keV were used to make these projections.

If the 91.2 and 56.8 keV γ rays belong to a two-transition cascade, the 5839-91.2-56.8 keV α - γ - γ decay path would have a $Q_{\alpha,tot} = 6121(10)$ keV, which is within experimental uncertainty of the $Q_{\alpha,tot}$ values of the aforementioned groups¹. A cascade involving the 91.2 keV γ ray and the strongly converted 56.8 keV transition would also explain the high-energy tail seen on the $E_{\alpha} = 5839$ keV peak in Fig. 5.10 (b). Therefore, we assign these decay paths to the fine-structure decay of the isomeric state in ^{178}Au .

The 5740-56.8 keV group requires the presence of a yet unobserved 189 keV γ -ray transition in order to match the $Q_{\alpha,tot} = 6118$ of the 5925-56.8 keV coincidence group. The missing transition energy is indicated by the dashed arrow between the 374 keV and 185 keV levels in Fig. 5.8.

The 5839-67.6 keV decay path is missing 80.4 keV of energy in order to match the 91.2-56.8 keV γ cascade. The missing energy is greater than that of the Ir K_{β} x rays ($E_x = 73$ -76 keV [34]), and the γ -ray detection efficiency at this energy is greater than at 67.6 keV. Thus, taking into account the number of counts for the 5839-67.6 keV group seen in Fig. 5.10 (c), a 5839-80.4 keV group should be visible in Fig. 5.6 (f). However, no such transition is seen. The absence of an 80.4 keV γ -ray transition in the data could be due to it being strongly converted. This explanation is supported by the large total conversion coefficients of $\alpha_{c,tot}(80.4 \text{ keV}) = 11.4(2)$, $11.6(2)$ and $122.3(2)$ calculated using BrIcc [88] for M1, E2 and M2 γ -ray transitions, respectively. The presence of a 67.7-80.4 keV γ -ray cascade following the 5839 keV α decay could also explain the high-energy tail of the 5839 keV peak in Fig. 5.10 (c). However, it is impossible to determine whether the missing 80.4 keV transition would come before, or after the 67.6 keV γ ray in such a cascade. Thus, this decay path is omitted from Fig. 5.8.

A small number of α decays in coincidence with the 139.2 keV γ ray are visible in Fig. 5.10 (d), at $E_{\alpha} \approx 5925$ keV. However, these are believed to be due to time-random background.

It was possible to determine the multipolarity of the 56.8 keV transition, due to it being the sole γ transition in coincidence with the 5925 keV α decay. This was achieved by comparing the number of single α decays measured in the $E_{\alpha} = 5925$ keV peak to the number of coincidence events in the 5925-56.8 keV α - γ group, corrected for the detection efficiency of the 56.8 keV γ ray. From this analysis, the total conversion coefficient, $\alpha_{c,tot}$, was calculated based on the relation

$$\alpha_{c,tot} = \frac{N_{\alpha} \cdot \epsilon_{\gamma}}{N_{\alpha,\gamma}} - 1, \quad (5.3)$$

¹The statistics were too low to verify the 91.2-56.8 keV γ -ray cascade with a γ - γ analysis.

Table 5.2: Energies for α decays (E_α) and γ transitions (E_γ) in coincidence with one another and the calculated total Q values ($Q_{\alpha,tot}$), for ^{178m}Au .

E_α [keV]	E_γ [keV]	$Q_{\alpha,tot}$ [keV]
5977(15)	0	6114(15)
5925(7)	56.8(3)	6118(7)
5844(15)	139.2(3)	6118(15)
5839(10)	56.8(3)	6030(10)
5839(10)	91.2(3)	6064(10)
5839(10)	91.2(3)+56.8(3)	6121(10)
5839(12)	67.6(10)	6041(10)
5740(12)	56.8(3)	5929(12)
5571(10)	421.4(5)	6120(10)
5521(10)	472.1(5)	6120(10)

where N_α is the number of events measured in the singles 5925 keV α -decay peak in Fig. 5.6 (b), ϵ_γ is the detection efficiency of the germanium detector for a 56.8 keV γ ray, and $N_{\alpha,\gamma}$ is the total number of coincidence events measured in the 5925-56.8 keV α - γ group in Figs. 5.6 (d). The analysis of the experimental data yielded a result of $\alpha_{c,tot} = 6.1(2)$.

Theoretical values of $\alpha_{c,tot}$ taken from the BrIcc conversion coefficient calculator [88], for 56.8 keV γ rays of different multiplicities showed that the measured value was closest to that of $\alpha_{c,tot}(\text{M1}) = 5.60(8)$. Thus, based on the comparison between the measured and calculated values, the 56.8 keV γ ray was assigned an M1 multiplicity.

The large value of $\alpha_{c,tot}$ value for the 56.8 keV transition resulted in a significant amount of α -e summing in the Si detectors. This is of particular importance as the L-conversion electron for a 56.8 keV transition has an energy of ~ 43 keV [88], which, when summed to the 5925 keV α decay, produces an α -e sum peak at ~ 5968 keV. Thus, a significant component of the peak at 5973 keV in Fig. 5.6 (b) is due to α -e summing, the effect of which is discussed in Section 5.3.2.

5.3.2 Alpha-decay intensities

The relative intensities of the fine structure α decays of the two states in ^{178}Au were deduced by fitting the peaks in the singles α -decay spectra with crystal ball

functions, where possible. The results of the fitting can be seen in Fig. 5.11. In cases where this was not possible, the number of counts in the different α - γ coincidence groups, corrected for the the γ -ray detection efficiency, were compared². The extracted intensities are shown in Fig. 5.8.

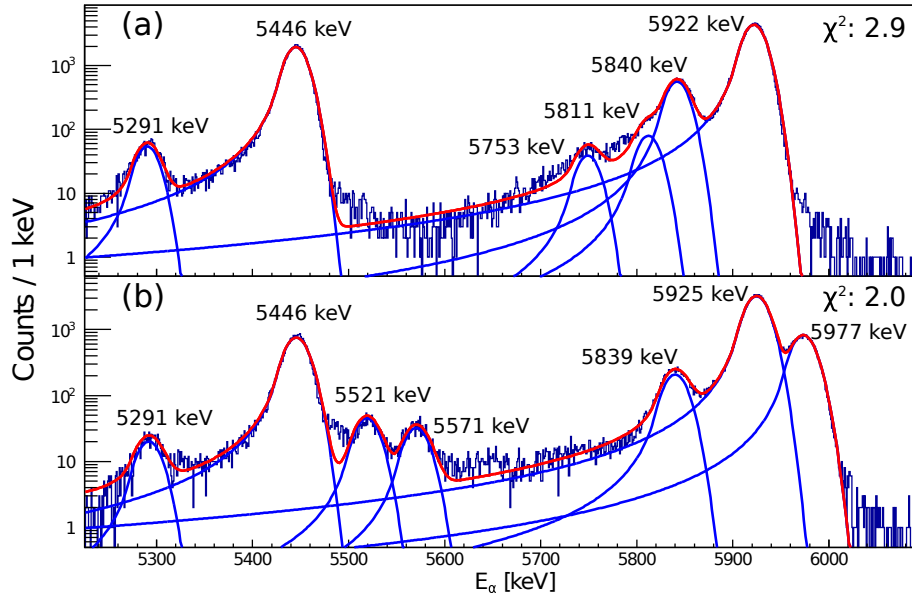


Figure 5.11: The ^{178}Au (a) ground and (b) isomeric states singles α -decay spectra, fitted with crystal ball functions. As well as the ^{178}Pt 5291 and 5446 keV α -decay peaks, the procedure includes the $E_\alpha = 5753, 5811, 5840$ and 5922 keV peaks and the $E_\alpha = 5521, 5571, 5839, 5925$ and 5977 keV peaks for the fitting of the ground and isomeric states singles spectra, respectively.

GEANT4 simulations for alpha-electron summing events

As mentioned previously, a significant component of the the 5973 keV α -decay peak of the isomeric state is due to α -e summing. The effects of this summing were investigated using GEANT4 simulations, the results of which are discussed in the following section.

The contribution to the 5973 keV singles α peak in Fig. 5.6 (b), due to α -e summing from the 5925-56.8 keV fine structure decay was investigated using GEANT4 [89, 90]. The simulation included the detectors Si1 and Si2, with the implantation pattern approximated by generating particles over a two-dimensional Gaussian distribution (se Fig. 5.12). The full-width tenth maximum of the Gaussian was set to be equal to the diameter of the carbon implantation foils (6 mm) of the Windmill decay station.

²We note that no corrections for the conversion coefficients of these γ -ray transitions were made as their multiplicities are unknown. However, we do not expect this effect to be significant.

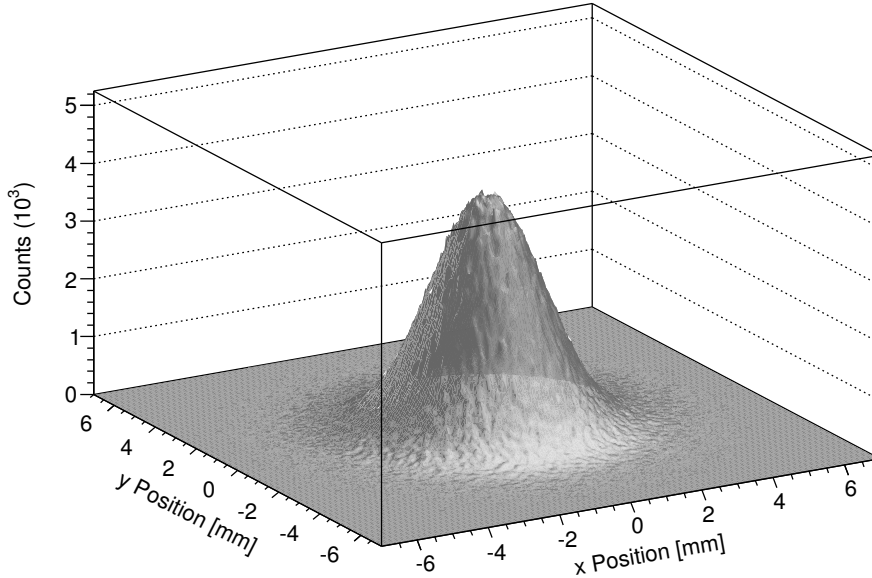


Figure 5.12: Spatial distribution of 10^7 events initialised in the GEANT4 simulations.

An isotropic emission of α particles was simulated, with $E_\alpha = 5925$ keV. An electron was generated following the α particle, with energy, E_{ce} , and probability of generation determined by the respective conversion coefficients for L-, M-, N-, O- and P-conversion electrons. Values for E_{ce} and α_c were taken from the BrIcc calculator and are shown in Table 5.3. In the case of an L-electron, an L x ray was also generated, with energies and intensities taken from Ref. [34]. The simulation excluded K-shell electrons as their 76.1 keV binding energy [34] is greater than the γ -transition energy, making K-conversion impossible.

Table 5.3: Average energies (E_{ce}) and conversion coefficients (α_c) for conversion electrons competing with a 56.8 keV, M1 γ transition, calculated using BrIcc [88].

Shell, Λ	E_{ce} [keV]	$\alpha_c(\Lambda)$
L	43.46	4.32(6)
M	53.66	0.995(14)
N	56.12	0.244(2)
O	56.71	0.0433(6)
P	56.79	0.00326(5)
	$\alpha_{c,tot}$	5.60(8)

Figure 5.13 (a) shows the raw data from the simulation. The line at 5925 keV is due to full energy deposition of an α particle inside a detector volume. The higher energies lines represent summing events, in which an α particle and a conversion electron and/or x ray deposited their full energies in the detector. The continuum between these and the 5925 keV line is due to the full energy deposition of an α particle, plus the partial energy deposition of a conversion electron and/or an x ray.

In order to reproduce the experimentally measured spectra the raw data from the simulation was broadened using a crystal ball function. Parameters for the broadening were taken from fits of experimental data. Figure 5.13 (b) shows the overlap between the experimental data, and the broadened simulated spectrum scaled to match the height of the 5925 keV peak in the experimental results spectrum.

The difference between the experimental and the scaled simulated data is shown in Fig. 5.13 (c). There is a significant reduction in intensity of the peak at $E_\alpha = 5973$ keV, as well as a shift in the peak centroid to $E_\alpha = 5977(15)$ keV. From this it was possible to extract the intensities of the 5840 and 5977 keV peaks, relative to that of the 5925 keV α decay. The final results for the extracted intensities are shown in Fig. 5.8.

The simulation was run again using the extracted intensities for the 5839, 5925 and 5977 keV α decays, plus the effects of the α -e-x ray summing events with the 5925 keV peak. The results for the simulated data and experimental results are overlapped in Fig. 5.14, and are in good agreement with one another.

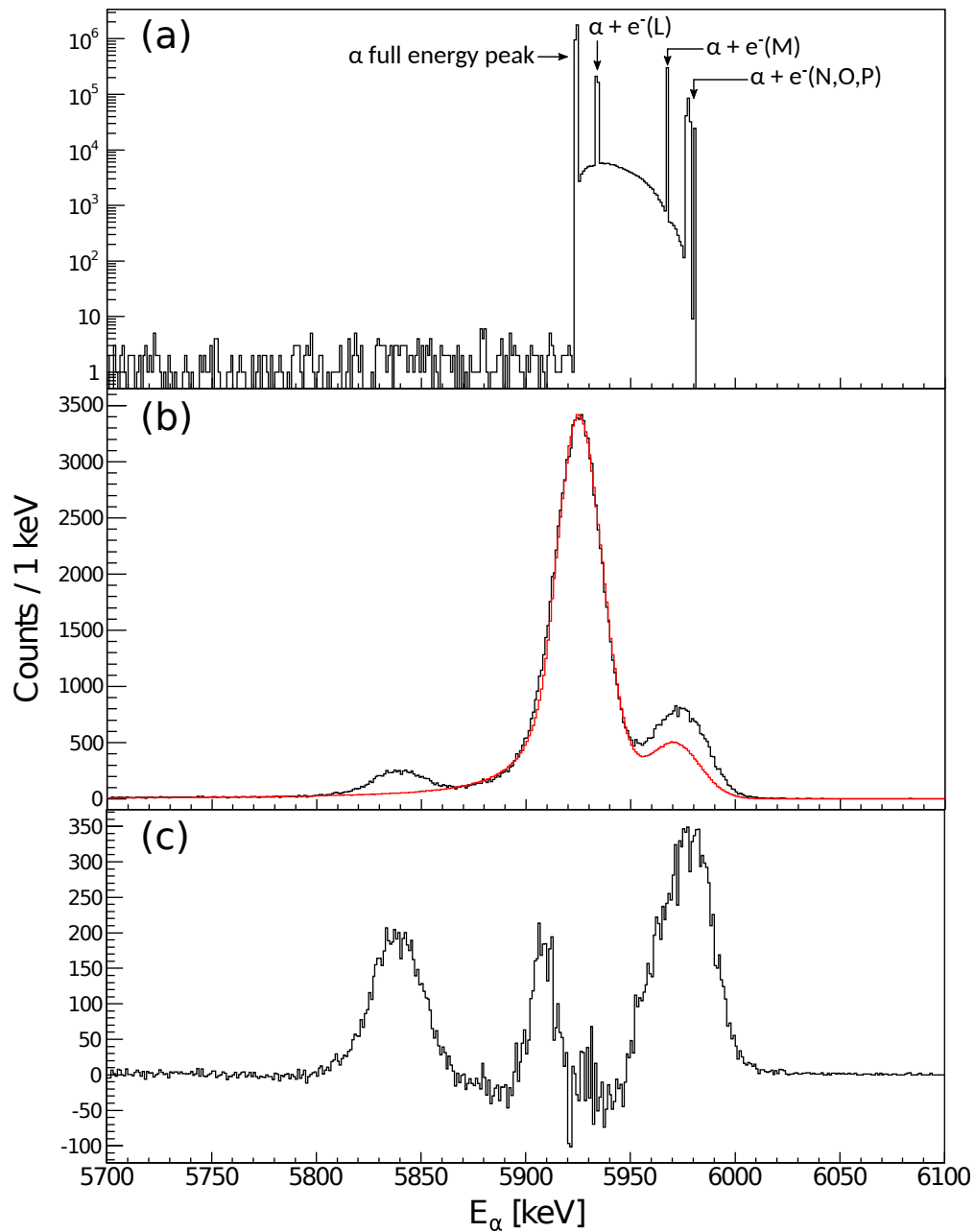


Figure 5.13: (a) the results of the GEANT4 simulations of a 5925 keV α particle plus a conversion electron and/or an L x ray, with energy and generation probability determined by the BrIcc calculator. The peak at 5925 keV is due to the full energy of a single α particle being deposited in the detector material. Counts at higher energies are due to summing events involving full energy deposition by the α particle, with either the full (peaks) or partial (continuum) energy deposition of the electron and/or L x rays, (b) an overlap of the experimental data (black) with the broadened results of the GEANT4 simulations (red), (c) the difference between the two.

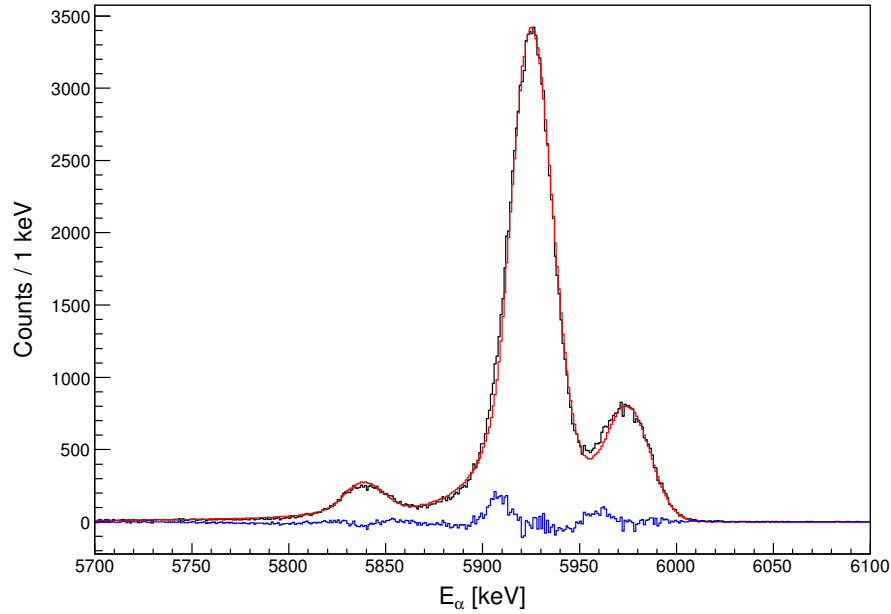


Figure 5.14: The singles α spectrum of the experimental data (black) overlapped with the results from the GEANT4 simulation of the three main α peaks plus α and electron summing events (red), by assuming the deduced intensities of the 5839, 5925 and 5977 keV α decays. The blue trace shows the difference between the two.

5.4 Decay branching ratios

The branching ratios for α decay, b_α , and β decay, b_β , for the two states were calculated by comparing the number of observed ^{178}Au and ^{178}Pt α decays, corrected for the α -decay branching ratio of ^{178}Pt ($b_\alpha(^{178}\text{Pt}) = 7.7(3)\%$ [91]). Based on the observed difference in the α - γ decays matrices shown in Figs. 5.6 (c) and (d), we conclude that there is no internal transition between the isomeric and ground state in ^{178}Au . Were an internal transition decay branch to exist, the α - γ coincidences belonging to the ground-state decay would be visible in the spectra of the isomer. This is not the case, thus, b_α and b_β should sum to unity for both the ground and isomeric states, and the ratio of the two values can be defined as

$$\frac{b_{\alpha,Au}}{b_{\beta,Au}} = \frac{b_{\alpha,Pt} \cdot N_{\alpha,Au}}{N_{\alpha,Pt}}, \quad (5.4)$$

where N_α is the number of measured α decays.

This method assumes that all observed α decays of ^{178}Pt originate from the β decay of ^{178}Au , and that surface ionisation of Pt within the ion source is negligible. This was confirmed by measurements made during runs with the lasers switched off.

Dedicated runs were made for these measurements, during which the wheel

of the Windmill was not rotated to avoid removing any activity from ^{178}Au and ^{178}Pt α decays. The results were $b_\alpha = 16(1)\%$, $b_\beta = 84(1)\%$ for the ground state, and $b_\alpha = 18(1)\%$, $b_\beta = 82(1)\%$ for the isomer.

5.5 Half-lives

Half-life measurements of the two states were made using a grow-in/decay method. A 13.2 s period of implantation was followed by a 6 s period of no implantation, during which the decay curves of the α decays could be measured. This sequence was repeated for a number of SCs, and the data taken during each SC summed together in order to improve statistics.

Unfortunately, during these measurements the system suffered from a significant dead time. This was due to high count rates in the germanium detectors which caused the buffers of the DGF cards to fill quickly, requiring them to spill frequently.

This dead time issue was corrected using the pulser connected to the DAQ. The ratio between the measured rate of the pulser, and the rate of 100 Hz to which the pulser was set, gave the fractional live time of the system. This allowed the measured α -decay rates to be dead time corrected accordingly. Panels (a) and (b) in Fig. 5.15 show the measured α -decay rates before and after the dead time correction, respectively.

Due to its longer half-life of $t_{1/2} = 21.1(6)$ s, ^{178}Pt produced by the β decay of ^{178}Au survived to the decay position, after the Windmill wheel was moved at the end of each SC. Therefore, it was possible to measure a pure ^{178}Pt α decay curve in Si3 and Si4, without any contribution from the β decay of newly implanted ^{178}Au activity. Fitting the decay curve measured at the decay site yielded $t_{1/2}(^{178}\text{Pt}) = 25(4)$ s, which, with its relatively large uncertainty, is in experimental agreement with the tabulated value. The large uncertainty stems from low statistics in the measured decay curves of ^{178}Pt , as well as the short measurement period of 36 s (defined by the length of the SC) relative to $t_{1/2} = 21.1$ s, further limiting the accuracy of the half-life extracted from the fitting of the data.

The corrected data for the $^{178g,m}\text{Au}$ decay curves measured by Si1 and Si2, were fitted using exponential functions (see Fig. 5.16) and the half-lives extracted. This gave $t_{1/2} = 3.4(5)$ s for the ground state and $t_{1/2} = 2.7(5)$ s for the isomeric state. Conservative error estimates are given to account for the dead time correction, as well as the short time window in which the measurement of the decay curve was taken, relative to the extracted values.

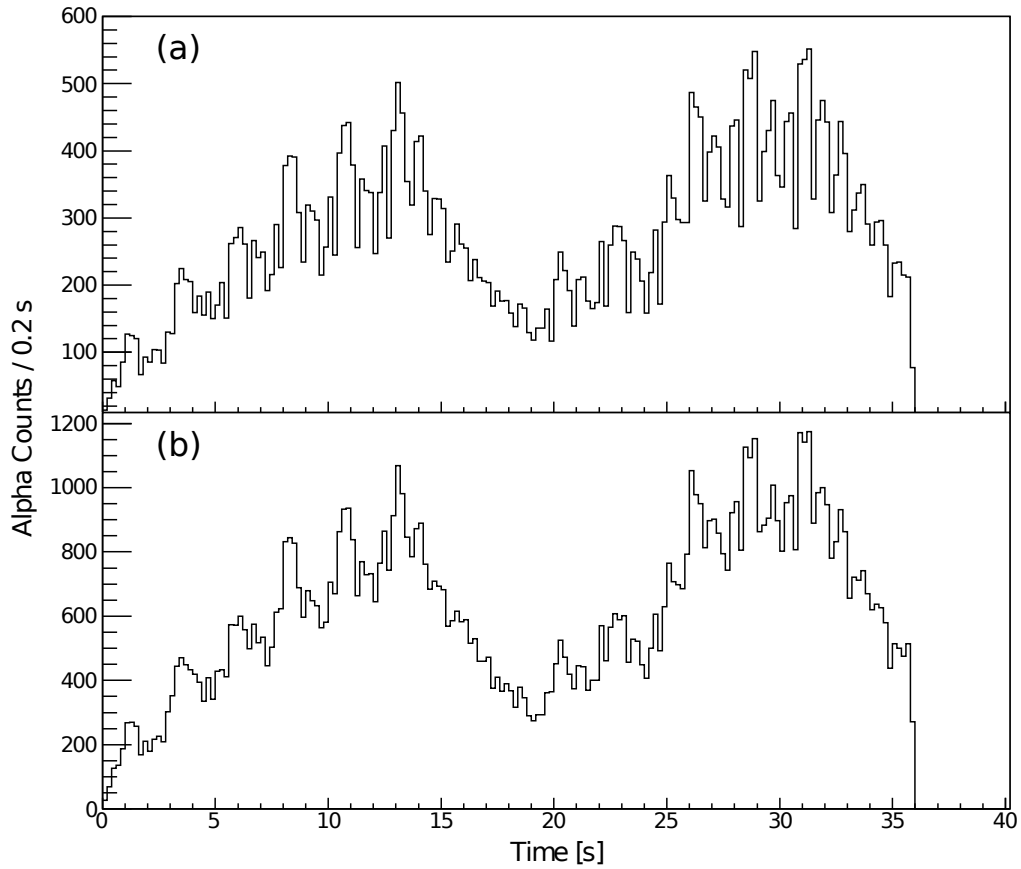


Figure 5.15: Comparison of the data taken for half life measurements of ^{178}gAu , before (a), and after (b) the dead time correction.

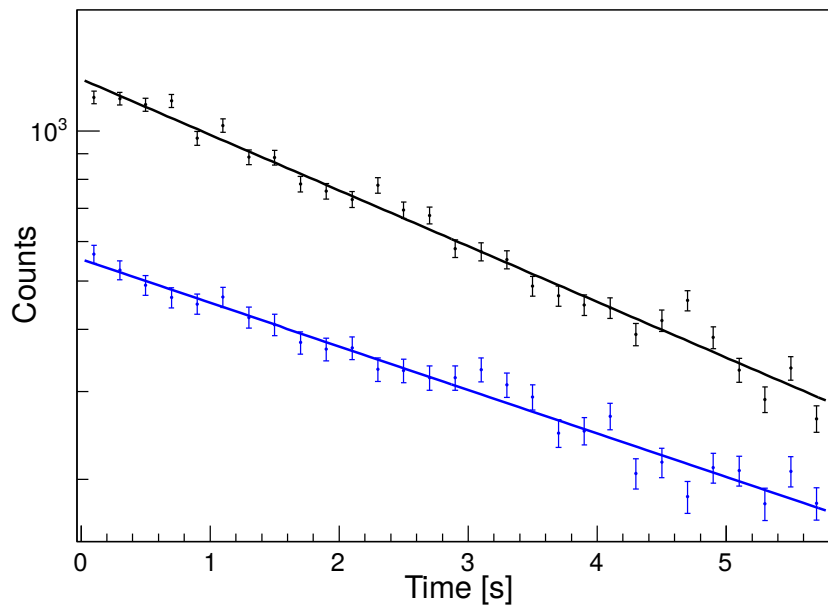


Figure 5.16: The extracted decay curves for ^{178}g (black), and ^{178}mAu (blue), gating on single α -decay events measured during the 'decay' period at the implantation position. The data are fitted with exponential functions.

5.5.1 Reduced widths and hindrance factors for alpha decays

The reduced α -decay widths were calculated using the Rasmussen approach [43], assuming $\Delta L = 0$ between the initial and final states. The results of these calculations are displayed in Fig. 5.8.

5.6 The 5521 keV and 5571 keV alpha decays of the isomeric state

The intensities of the 5521 and 5571 keV α decays were assessed using two methods; the first took the integral of the number of counts underneath the peaks in the singles α -decay spectrum shown in Fig. 5.6 (b); the second method took the integral of the 5521 and 5571 keV components derived from the crystal ball fitting procedure, shown in Fig. 5.11 (b). The results are shown in Table 5.4, with the subscripts “integ” and “CB” denoting the integral and crystal ball fitting methods, respectively, along with their corresponding δ_α^2 and HF_α values. The results from the two methods are in agreement, and show that the 5521 and 5571 keV decays are unhindered, indicating that the states they decay to in ^{174}Ir have a similar structure to the 56.8 keV level populated by the 5925 keV α decay.

Table 5.4: Reduced α -decay widths for the main peaks seen in the singles spectrum; intensities taken from integrating the number of counts underneath the 5521 and 5571 keV peaks (left), or from the integral of the individual components of the crystal ball fits shown in Fig. 5.11 (right).

E_α [keV]	$I_{\alpha,\text{integ}}$ [%]	δ_α^2 [keV]	HF_α	$I_{\alpha,\text{CB}}$	δ_α^2 [keV]	HF_α
5521	1.0(4)	41(20)	1.3	1.07(3)	45(12)	1.2
5571	0.9(3)	22(9)	2.5	0.77(2)	19(5)	2.8
5839	4.5(1)	6.6(15)	8.2	4.49(6)	7(1)	7.7
5925	86.5(4)	54(11)	1.0	86.42(35)	54(11)	1
5977	7.3(3)	2.8(6)	19	7.25(2)	2.8(6)	19.3

However, in addition to the 421.4 and 472.4 keV γ -ray transitions, the 5521 and 5571 keV α decays are seen in coincidence with large numbers of Ir x rays (see Fig. 5.6 (d)). There are two possible reasons for the presence of these x rays. The first is that the 421.4 and 472.1 keV γ -ray transitions are strongly converted. By comparing the number of events in 5521-472.1 keV group to the integral of the 5521 keV peak of the crystal ball fits in Fig. 5.11 (b), a value of $\alpha_{c,\text{tot}} = 2.4(12)$ for the 472.1 keV

Table 5.5: Theoretical $\alpha_{c,tot}$ values for 421.4 and 471.2 keV γ -ray transitions of varying different in Ir, taken from [88].

E_γ [keV]	421.4		472.1	
ΔL	E	M	E	M
1	0.0116(2)	0.113(2)	0.0090(1)	0.84(1)
2	0.0366(6)	0.368(6)	0.0274(4)	0.259(4)
3	0.131(2)	1.03(2)	0.090(1)	0.69(1)
4	0.497(7)	2.98(5)	0.307(5)	1.85(3)

γ -ray transition was extracted. By a similar analysis and in the extreme of taking all 7 counts in Fig. 5.10 (e) as belonging to the 5571-421.4 keV fine-structure decay, a value of $\alpha_{c,tot} = 0.62(24)$ was calculated. The experimental results can then be compared to the theoretical values of $\alpha_{c,tot}$ for 421.4 and 471.2 keV γ -ray transitions of varying multiplicities, belonging to an Ir nucleus are given in Table 5.5.

The experimentally extracted value for a 472.1 keV transition is in closest agreement with the theoretical values of $\alpha_{c,tot}(M4) = 1.85(3)$. As for the 421.4 keV γ ray, the calculated $\alpha_{c,tot}$ value is consistent with the theoretical values for M2 and E4 transitions. However, the prompt nature of these transitions, observed in both the ISOLDE and JYFL data, rules out high-multipolarity transitions, as these would have single-particle transition half-lives in excess of hundreds of seconds [34].

An M2 transition would require the 421 keV level in the ^{174}Ir isomer to have a different parity to the states fed by the 5925-56.8 keV fine-structure decay. This would introduce significant hindrance to the α -decay process, which is not reflected in the results shown in Table 5.4. In addition to this, the low K-conversion coefficient $\alpha_{c,K} = 0.291(4)$, calculated using BrIcc [88], for a 421.4 keV M2 γ ray cannot explain the large number of Ir K-x rays seen in coincidence with the 5571 keV α decay, shown in Figs. 5.6 (d) and (f).

An alternative explanation could be that the two states populated by the 5521 and 5571 keV α decays have the same spin-parity quantum numbers as the one fed to by the 5925 keV α decay, and de-excite via transitions involving strong E0 components. In such a scenario, the 421.4 and 472.1 keV γ -ray transitions would have mixed E0/M1/E2 compositions. The electric monopole operator is directly related to the nuclear mean-squared charge radius, with the strengths of E0 transitions between mixed states of differing radii being enhanced [10, 92]. Thus, the presence of an E0 component of a transition is a strong signature for shape-coexistence. This interpretation would mean that the α decay of the isomeric state in ^{178}Au would

populate a triplet of states in ^{174}Ir , with the same spin-parities but different shapes.

The origins of the unhindered 5521 and 5571 keV α decays are still under discussion and remain a complex issue that goes beyond the scope of this work. The final interpretation will be given in an upcoming publication, currently in preparation [72].

The possible effect of α -E0 electron summing was investigated using GEANT4. Simulations were made for a 5521 keV α particle and a 396 keV K-electron (in place of a 472.1 keV γ ray), with $\alpha_{c,K}$ values of 1.5, 2.0 and 2.5. The results for the $\alpha_c = 2.0$ simulation are shown in Fig. 5.17. The number of counts due to summing for $\alpha_c = 2.0(5)$ was found to be 15.5(2)% of the number due to single α events, and so the Ir x rays seen in coincidence with α decays between $E_\alpha = 5500$ and 5800 keV can be explained in part by α -e summing from the 5521-472.1 and 5571-421.4 keV fine structure decays. The counts in the peak at $E_\alpha \approx 5920$ keV in Fig. 5.17 would contribute somewhat to the 5925 keV peak in Fig. 5.6 (b). However, number of counts in the α -e sum peak would be negligible when comparing the experimental spectrum to that of the simulation, when scaling to match the intensity of the 5521 keV α -decay peak.

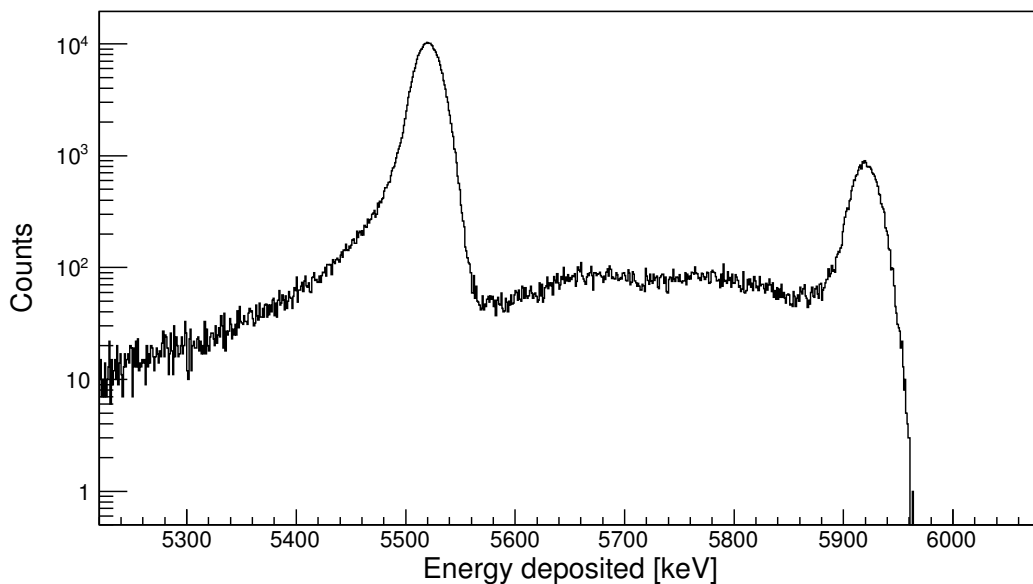


Figure 5.17: Spectrum for the results of GEANT4 simulations for α -e summing in the silicon detectors, between a 5521 keV α particle and a 396 keV conversion electron, with $\alpha_c = 2.0$.

5.7 Spin assignments for $^{178g,m}\text{Au}$

Spin assignments were made by identifying which states in the ^{178}Pt daughter nucleus were populated by the β decay of ^{178}Au , by observing the β -delayed γ -ray transitions. Figures 5.18 (a) and (b) show the background-subtracted singles γ -ray spectra measured in Ge1 for the ground and isomeric states, respectively. The background spectra were taken from measurements made with the lasers turned off.

The 257.4(3) keV and 170.4(3) keV peaks in Fig. 5.18 (a) correspond to the known $4_1^+ \rightarrow 2_1^+$ and the $2_1^+ \rightarrow 0_1^+$ E2 γ -ray transitions of the ^{178}Pt yrast band. In contrast to this, four peaks are seen in Fig. 5.18 (b) at $E_\gamma = 413.6(3)$, 338.1(3), 257.4(3) and 170.4(3) keV. The additional two peaks at 413.6 and 338.1 keV correspond to the $8_1^+ \rightarrow 6_1^+$ and $6_1^+ \rightarrow 4_1^+$ E2 γ transitions in the ^{178}Pt yrast band, respectively.

Due to the feeding to $I = 4$ states, and assuming no high-order forbidden β decays between the ^{178}Au and ^{178}Pt nuclei, a spin of 3 or 4 was assigned to the ground state in ^{178}Au . A spin of 5 was excluded as no γ transitions from states with a spin of 6 were recorded. Based on the feeding to the $I = 8$ state in ^{178}Pt , a spin of 7 or 8 was assigned to the isomeric state. An $I = 9$ assignment was excluded as no feeding to the $I = 10$ states in ^{178}Pt was observed. This confirms the observations made by Davidson *et al.* [13], and their suggestion that the observer feeding was due to the presence of both a low-spin and a high-spin β -decaying state in ^{178}Au . However, thanks to the laser-ionisation method employed during the ISOLDE study, it was possible to cleanly separate the two states for their respective studies.

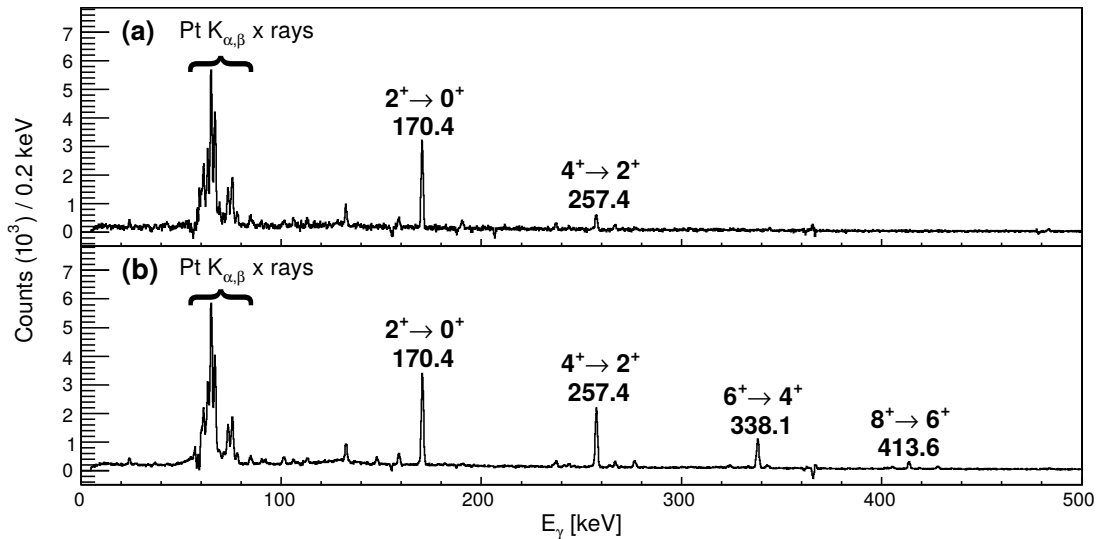


Figure 5.18: Background subtracted singles γ spectra for the ground (top panel) and isomeric (bottom panel) states in ^{178}Au .

5.8 Configuration assignments for the ground and isomeric states in ^{178}Au and ^{174}Ir

The Nilsson diagram for single-particle orbitals in the vicinity of ^{178}Au ($Z = 79$, $N = 99$) are shown in Fig. 5.19. Preliminary results from the laser spectroscopy measurements show that both $^{178g,m}\text{Au}$ are deformed, yet the sign of the deformation is unknown. This, combined with the high density of states originating from $\pi 3s_{1/2}$, $\pi 2d_{3/2}$ and $\pi 1h_{11/2}$ orbitals for protons, and the $\nu 1h_{9/2}$ and $\nu 2f_{7/2}$ orbitals for neutrons, makes it difficult to interpret the underlying configurations of $^{178g,m}\text{Au}$. However, the known configurations of the low-lying states in the neighbouring odd- A isotopes (see Fig. 5.8) can give some clue as to what may be expected. Further constraints on the possible proton-neutron configurations can be made using the Gallagher-Moszkowski (GM) rules [93] – a set of rules which give a guideline for the coupling of the angular momenta of the odd proton and neutron in an odd-odd nucleus. The GM rules state that the spins and angular momenta of the odd proton and neutron couple to give the total spin of the nucleus, I , such that

$$\begin{aligned} I &= \Omega_p + \Omega_n, & \text{if } \Omega_p = \Lambda_p \pm 1/2 & \text{ and } \Omega_n = \Lambda_n \pm 1/2 \\ I &= |\Omega_p - \Omega_n|, & \text{if } \Omega_p = \Lambda_p \pm 1/2 & \text{ and } \Omega_n = \Lambda_n \mp 1/2, \end{aligned}$$

where Ω and Λ represent the usual asymptotic quantum numbers of the Nilsson model (see Section 2.1.3), the subscripts p and n represents protons and neutrons, respectively, and the values of $1/2$ represents the intrinsic spin of the nucleons. These rules reflect the preference of the odd proton and neutron to couple with their intrinsic spins aligned. It should be noted that these rules are not absolute (see Ref. [93] for more details), but hold well in regions with 3 or more particles outside of a closed shell. The Au nuclei, having three protons less than the $Z = 82$ shell closure, lie on this limit of applicability. As such, the configuration assignments provided using the GM rules in the following discussions are given tentatively.

The spin assignment in this work of $I = (7, 8)$ for ^{178m}Au cannot be made by coupling of the $\pi 3s_{1/2}$ or $\pi 2d_{3/2}$ to either the $\nu 1h_{9/2}$ or $\nu 2f_{7/2}$ orbitals. Thus, the valence proton of the isomeric state in ^{178}Au is assigned to the unique-parity $\pi 1h_{11/2}$ orbital. This is consistent with the known $\pi 1h_{11/2}$ configuration of the high-spin state in the neighbouring ^{177}Au nucleus [81]. As for the valence neutron, the GM rules would rule out a state originating from a $\nu 1h_{9/2}$ orbital as it would not preferentially couple to a $\pi 1h_{11/2}$ proton. The possible combinations of coupled proton-neutron

Nilsson states, origination from either a $\pi 1h_{11/2}$ or $\nu 2f_{7/2}$ orbital and give $I = 7$ or 8 , are shown in Table 5.6. At present it is not possible to distinguish which of these configurations is correct or most likely. Thus, for the high-spin $I = (7, 8)$ isomer in ^{178}Au , a $\pi 11/2^- (h_{11/2}) \otimes \nu 7/2^- (f_{7/2})$, configuration is proposed, with a positive parity assignment.

Assigning a configuration to the low-spin $I = (3, 4)$ ground state of ^{178}Au is more complicated, due to the possible mixing of the $\pi 3s_{1/2}$ and $\pi 2d_{3/2}$ states. Multiple solutions can be found for configurations that give $I = 3$ or 4 by employing the GM rules (see Table 5.6). However, as was the case with the isomeric state, it is not possible to distinguish which of these configurations is correct with the current data. Therefore, a negative parity is assigned to ^{178g}Au , with either a $\pi 1/2^+ (s_{1/2}) \otimes \nu 7/2^- (h_{9/2})$, or a $\pi 1/2^+ (d_{3/2}) \otimes \nu 7/2^- (f_{7/2})$ configuration.

The values of δ_α^2 extracted from the data (shown in Fig. 5.8) can give some indication as to the structure of the daughter states in ^{174}Ir , populated by the α decay of $^{178g,m}\text{Au}$. The unhindered, $E_\alpha = 5922$ keV decay from ^{178g}Au to ^{174g}Ir suggests that ^{174g}Ir has the same configuration as ^{178g}Au .

In comparison, the isomeric-to-isomeric state, $E_\alpha = 5977$ keV α decay is hindered. The 56.8 keV M1 γ -ray transition following the unhindered 5925 keV α decay could suggest that the 56.8 keV level and 0 keV state in ^{174m}Ir are two states of the same proton-neutron multiplet. In this scenario, the 5977 keV α decay would be hindered by a spin difference between ^{174m}Ir and the 56.8 keV level. Alternatively, the configurations of ^{178m}Au and ^{174m}Ir may differ, giving rise to the observed level of hindrance.

The final analysis of the data from the laser spectroscopy measurements on Au isotopes taken during the IS534 experiment is ongoing. The results from these data will include extracted values for the magnetic moments of the Au nuclei that were studied. These will provide a better insight into the underlying proton and neutron configurations in $^{178g,m}\text{Au}$.

Based on the analysis and results presented in this chapter, it was possible to produce the decay scheme shown in Fig. 5.8. The results from the mass measurements of $^{178g,m}\text{Au}$ are not presented here³, and so the energy labels given for the states in ^{174}Ir are the excitation energies relative to either the ground, or isomeric state to which they decay.

³The mass measurements will be included in the forthcoming publication [72]

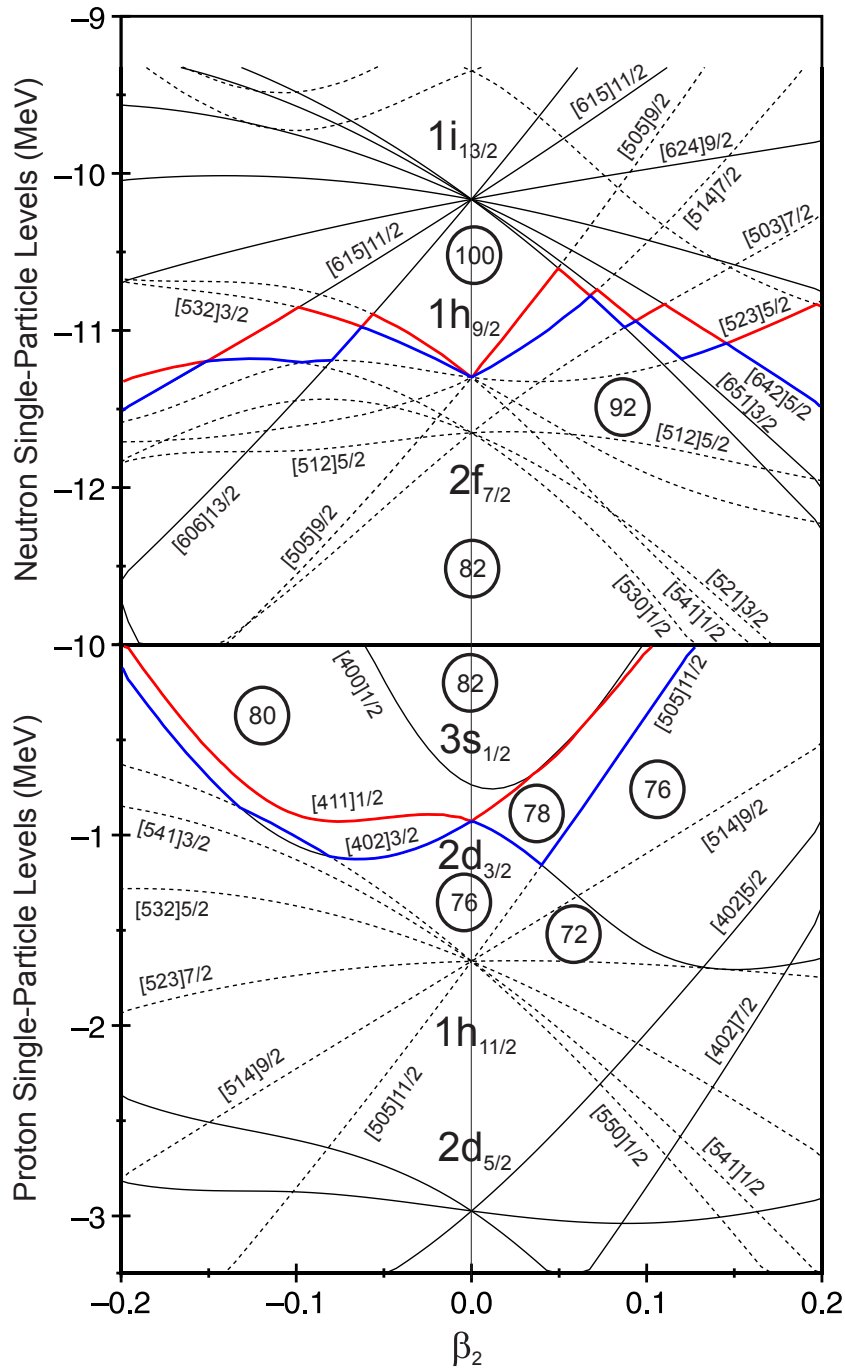


Figure 5.19: Single-particle energies for neutron (top panel) and proton (bottom panel) Nilsson orbitals, in the regions pertinent to ^{178}Au ($Z = 79$, $N = 99$). The dashed and solid lines represent negative, and positive parity states, respectively. The red and blue lines represent the ^{178}Au and ^{174}Ir Fermi surfaces, respectively. Figure adapted from [94].

Table 5.6: The possible configurations for the odd proton and neutron states in $^{178g,m}\text{Au}$, in accordance with the Gallagher-Moszkowski (GM) angular-momenta coupling rules, and their corresponding spherical shell model orbitals.

State		GM rule assignment		Spherical orbital	
		I	π	ν	π
Ground state	3	1/2[400]	7/2[514]	$3s_{1/2}$	$1h_{9/2}$
		1/2[411]	7/2[503]	$2d_{3/2}$	$2f_{7/2}$
	4	1/2[400]	9/2[505]	$3s_{1/2}$	$1h_{9/2}$
Isomeric state	7	11/2[505]	3/2[521]	$1h_{11/2}$	$2f_{7/2}$
		9/2[514]	5/2[512]	$1h_{11/2}$	$2f_{7/2}$
		7/2[523]	7/2[503]	$1h_{11/2}$	$2f_{7/2}$
	8	11/2[505]	5/2[512]	$1h_{11/2}$	$2f_{7/2}$
		9/2[514]	7/2[503]	$1h_{11/2}$	$2f_{7/2}$

Laser spectroscopy studies of At isotopes

This chapter presents the measured HFS data and isotope/isomer shift values, the respective extracted changes in mean-square charge radii, and the nuclear magnetic dipole moments for $^{195-211,217,218,219}\text{At}$. The data were taken during the IS534 experiment conducted in September 2014. The results presented in this chapter represent the collaborative efforts of the RILIS, ISOLTRAP, and Windmill decay station research groups. The contribution to these efforts by the author was in leading experimental work with the Windmill setup, performing online analysis during the September 2014 IS534 experimental run, as well as the final offline analysis of decay data and extraction of the HFS spectra taken by the Windmill group, for $^{195-200,202,217,218}\text{At}$. Due to the systematic nature of the study, it does not make sense to exclude the results taken by the ISOLTRAP group, and so the results are presented and discussed as an entire set in the following chapter.

During the experiment, ionisation of the At atoms was achieved by a three-step photoionisation process in order to excite atomic electrons resonantly using RILIS. The first excitation step was performed by a 216.23 nm broadband (BB) dye laser, the second excitation step was made using a 795.21 nm narrowband (NB) titanium-sapphire laser, and the final ionisation step was made by a 532 nm EdgeWave Nd:YAG laser. (For more information on the RILIS laser system see Ref. [59].) The HFS of the different At isotopes were measured by scanning the second-step Ti:Sa lasing light across a range of frequencies. The ionisation efficiency at a given laser frequency is measured by either recording the number of ions produced using the ISOLTRAP MR-ToF device, or the number of α decays or γ transitions using the Windmill decay station.

6.1 Nuclear structure of At isotopes

As a first approximation, the At isotopes can be described by a valence proton coupled to a Po core. As such, it is expected that the At chain should be similar to that of the Po isotopes [14, 19]; nuclei in the vicinity of the $N = 126$ shell closure should have a near-spherical shape, with an onset of deformation commencing at $N \approx 114$ and increasing as the neutron number decreases.

The excitation energies of the $I^\pi = 9/2^-, 1/2^+, 7/2^-$ and $13/2^+$ states in the odd- A At isotopes are shown as a function of mass number in Fig. 6.1. These states are associated with the $\pi 1h_{9/2}$, $\pi 3s_{1/2}^{-1}$, $\pi 2f_{7/2}$ and $\pi 1i_{13/2}$ configurations, respectively. The data were taken from recent in-beam and α -decay studies (see [95, 96, 97, 98, 99, 100] and references therein) and shows that the ground states for even- N , $A \geq 197$ have a $\pi 1h_{9/2}$ configuration, as is expected when considering the spherical shell model.

In contrast, the ground-states of the lightest At isotopes are observed to possess a spin-parity of $1/2^+$. This is due to the lowering in energy of the $\pi 3s_{1/2}^{-1}$ intruder orbital which becomes the ground state for $A \leq 195$. Nuclei in this state are presumed to possess an oblate deformation.

The energies of the $I = 7/2$ and $13/2$ states are also seen to reduce significantly. This lowering of energies is greatest in ^{193}At , where the $I^\pi = 1/2^+, 7/2^-$ and $13/2^+$ states are almost degenerate, having respective excitation energies of 0, 5(10) and 39(7) keV. This systematic decrease in energy provides evidence that the lightest At isotopes are more collective in their nature, and more deformed.

Another feature is the disappearance of the $I^\pi = 9/2^-$ state for the $A \leq 195$ isotopes. This was explained by Kettunen et al. [96] as a change from the spherical $\pi 1h_{9/2}^3$ configuration, to an oblate nucleus in a $7/2^-$ [514] Nilsson orbital, originating from an admixture of the spherical $\pi 1h_{9/2}$ and $\pi 2f_{7/2}$ states.

Similar phenomena are also expected to be observed in the even- A isotopes of At. Shape coexistence is expected if the same intruder orbitals as in the odd- A neighbours play a significant role in the low-lying structure of the even- A isotopes.

The heavy At isotopes with $N \approx 132$, are expected to possess octupole deformation. Octupole deformed nuclei are predicted in regions where pairs of spherical single-particle levels with Δl and $\Delta j = 3$ exist near the Fermi level [101]. Nuclei in the region above the $Z = 82$ and $N = 126$ shell closures are such an example; here, the $\pi i_{13/2}$ - $\pi f_{7/2}$, and the $\nu j_{15/2}$ - $\nu g_{9/2}$ orbitals couple, increasing octupole collectivity. The predictions were recently proven by measurements of electric octupole (E3) transition strengths [5], which confirmed the presence of octupole deformation in ^{224}Ra ($Z = 88$, $N = 136$) and the presence of octupole collectivity in ^{220}Rn .

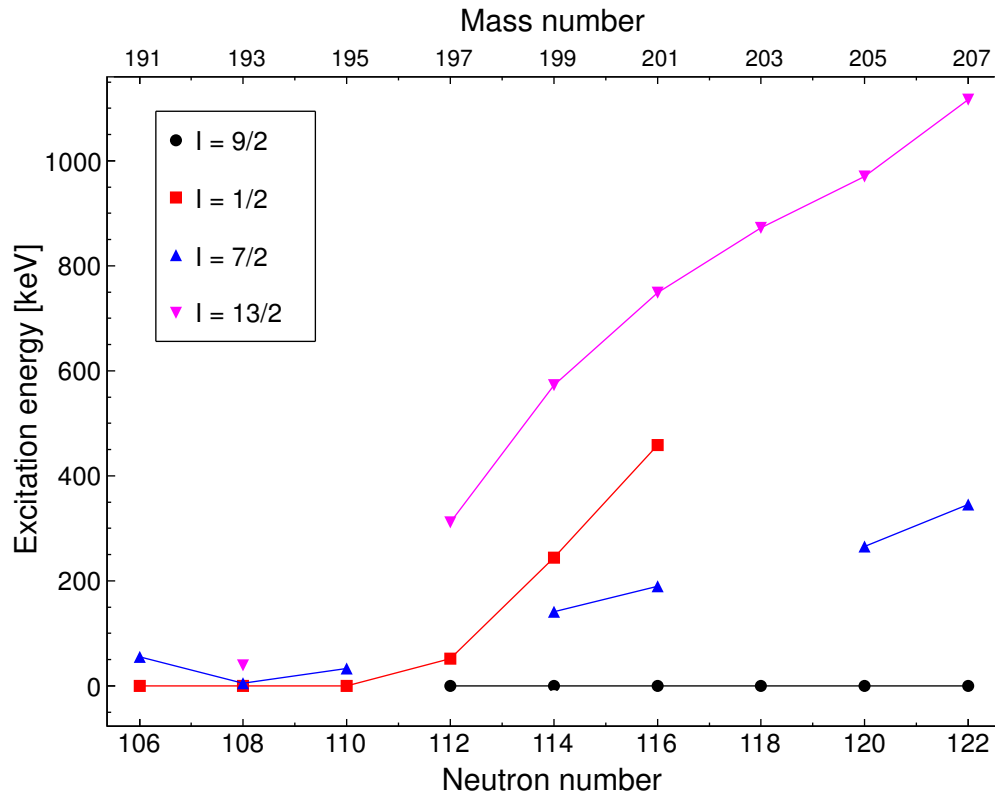


Figure 6.1: Energies of the $I = 9/2$ (black circles), $1/2$ (red squares), $7/2$ (blue triangles) and $13/2$ (pink downwards triangles) states in the odd-mass At isotopes, taken from [95, 96, 97, 98, 99, 100] and references therein.

Expected HFS

The left-hand side of Fig. 6.2 shows the three-step photoionisation scheme used during the experiment. The right-hand side presents a schematic view of the HFS expected from the coupling of a ^{199}At , $I = 9/2$ nucleus, to the two $J = 3/2$ atomic levels involved in the 795.21 nm transition, that was scanned during the experiment. These atomic levels are split into 4 hyperfine levels, with total atomic spins of $F = 3, 4, 5$ and 6. The red arrows indicate allowed transitions between the different hyperfine levels. The case depicted in Fig. 6.2 is representative of the most complex HFS measured during the experiment where there are 10 transitions between different hyperfine levels. This is the case for all nuclei with $I \geq 2$.

Simulations of what the measured HFS spectrum for ^{199}At , $I = 9/2$ should look like are shown in Fig. 6.3. The blue trace is what would be expected from a collinear method with a spectral resolution of ≈ 45 MHz, such as by the CRIS experiment [102], and the red trace is what is expected using the in-source method with a Doppler broadening of 850 MHz. The resolution for the in-source method as well as the a - and b -hyperfine parameters are taken from fits of the experimental data, discussed

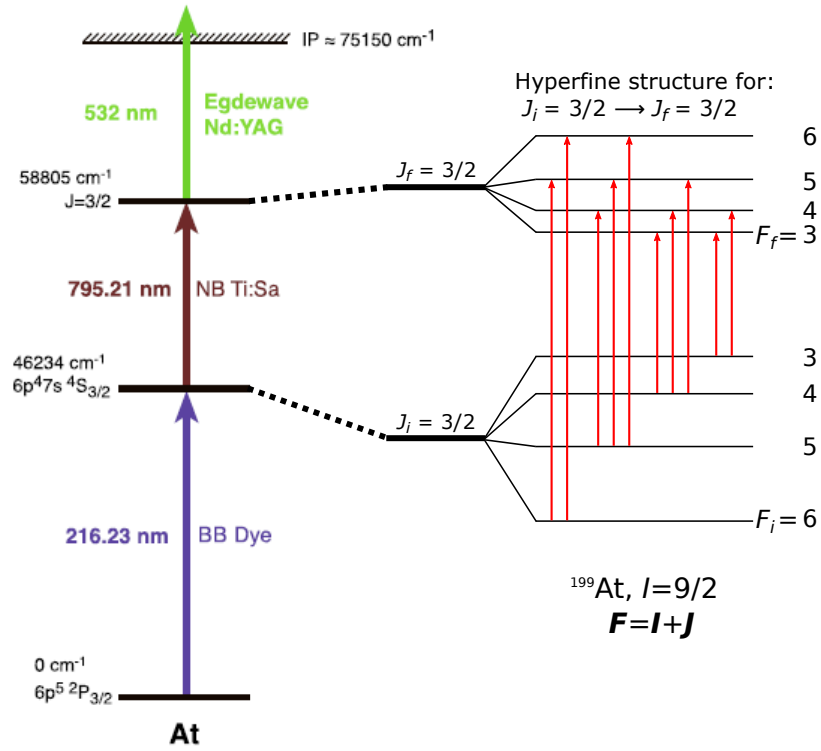


Figure 6.2: The three-step photoionisation scheme (left) used to ionise At atoms during the experiment, and the hyperfine splitting of the atomic levels due to the coupling of the nuclear and atomic electron spins (right), for an $I = 9/2$ ^{199}At nucleus. The red arrows indicate allowed transitions between initial and final states, after the hyperfine splitting. The magnitude of the splitting is not to scale.

in the following sections. The strengths of transitions between hyperfine levels, $S_{F_i F_f}$, relative to the strength of the transition between the initial and final unperturbed electronic states, $S_{J_i J_f}$, is given as

$$\frac{S_{F_i F_f}}{S_{J_i J_f}} = (2F_i + 1)(2F_f + 1) \begin{Bmatrix} F_i & F_f & 1 \\ J_f & J_i & I \end{Bmatrix}^2, \quad (6.1)$$

where the subscripts i and f denote initial and final states, respectively, and $\{\dots\}$ is a Wigner 6- j symbol.

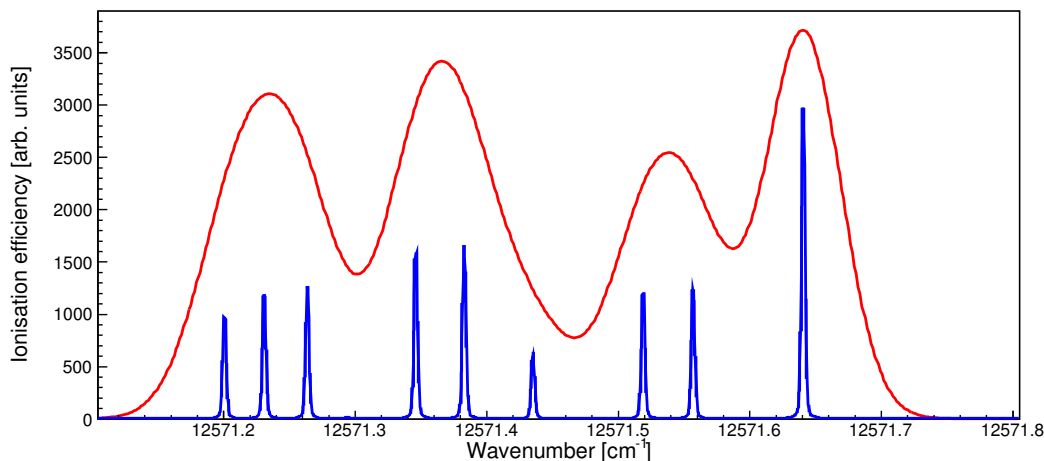


Figure 6.3: Simulation of the expected HFS measured for the hyperfine splitting shown in Fig. 6.2. The red trace is what would be expected from an in-source method such as the one used during the IS534, 2014 experiment, with a Doppler broadening of 850 MHz. The blue trace is what would be expected from a typical collinear laser spectroscopy method such as CRIS, with a Doppler broadening of 35 MHz. Both simulations use a Lorentzian width of 20 MHz, resulting in a total linewidth of 860 and 47 MHz for the in-source and collinear methods, respectively. The a and b factors used to produce the distribution of lines are taken from the fitting results of the ^{199}At HFS data, which is discussed further in the following sections. The intensity of the transitions are calculated using Equation 6.1. The $F_i = 4$ to $F_f = 4$ transition (centroid at $\approx 12571.9 \text{ cm}^{-1}$) has a very low intensity, thus, only 9 transition peaks are visible.

6.2 Extraction of hyperfine structure from windmill data

The HFS of the At isotopes were measured by counting the number of α decays or γ transitions measured by the Windmill setup, as a function of the laser frequency used for a specific step in the scan. This was done by setting energy gates to select the the decays of specific isomers.

For all but the ^{199}At $I = 1/2$ state, the characteristic α decays of different states were used, the energies of which are summarised in Table 6.1. The spectra shown in the left-hand panels of Fig. 6.4 are the singles α -decay spectra measured for each isotope, recorded over an entire laser scan run. The vertical coloured lines in these spectra represent the gating conditions used to select the α -decay energies listed in Table 6.1. The panels on the right-hand side of Fig. 6.4 show the extracted HFS plots, with the colours of the data points matching those of the lines of the gating conditions used to produce them.

The gating conditions were chosen such that the contribution from the tails from

peaks of similar energies were minimised. This includes the low-energy tails due to the energy attenuation of α particles as they pass through the carbon foil and the dead-layer of the Si detectors, and high-energy tails caused by α -e summing events due to fine-structure α decays that are followed by converted transitions in the daughter nucleus. In order to avoid contributions from these high- and low-energy tails narrow gating conditions were used, with just the most intense part of the peak selected. This is particularly evident in ^{200}At where the α -decay peak of the $I^\pi = 3^+$ state is sandwiched closely between those of the $I^\pi = 7^+$ and 10^- states. In the case of the $I = 1/2^+$ state in ^{195}At , it was possible to improve statistics by widening the gate in order to include the α decay of the $I = 1/2^+$ states in the ^{191}Bi daughter, which has $E_\alpha = 6870(3)$ keV, and $t_{1/2} = 121(8)$ ms [95].

Table 6.1: The α -decay energies that were gated on to select specific states of the At isotopes investigated using the Windmill setup. The spin assignment for ^{218}At from the analysis of the decay data taken during this run, the results of which are currently unpublished.

A	I^π	E_α [keV]	Ref.
195	$(1/2^+)$	6953(3)	[95]
	$(7/2^-)$	7075(4), 7221(4)	[95]
196	(3^+)	7049(3)	[75, 103, 104]
197	$(9/2^-)$	6959(3)	[76, 103, 105]
	$(1/2^+)$	6705(4)	[76, 105, 106]
198	(3^+)	6753(4)	[74, 75, 76]
	(10^-)	6854(4)	[74, 76, 103]
199	$(9/2^-)$	6643(3)	[103, 107, 108]
200	(3^+)	6464.5(18)	[73]
	(7^+)	6412.0(18)	[73]
	(10^-)	6536(4)	[73]
202	(3^+)	6227.7(14)	[73]
	(7^+)	6134.6(12)	[73]
217	$9/2^-$	7066.9(16)	[73]
218	(2^-)	6653(5), 6693(3), 6756(5)	[73]

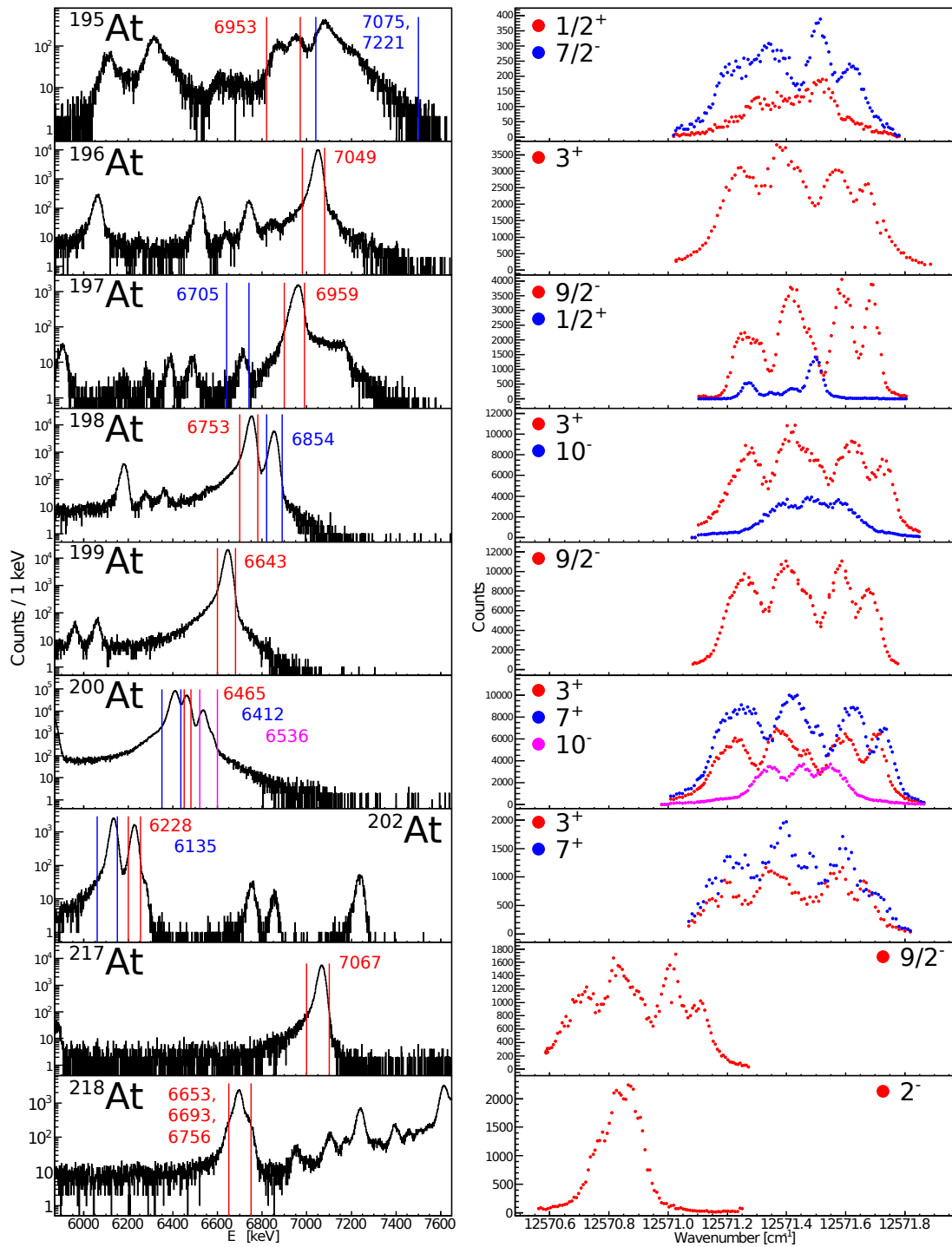


Figure 6.4: The panels on the left-hand side show the Windmill data for the single α -decay spectra. The peaks are labelled with their decay energies in keV, and the respective gating conditions used to extract the HFS are indicated by the vertical lines, with colours matching that of the energy labels. The panels on the right-hand side show the data for the extracted HFS as a function of the measured wavenumber, with the colours of the data points matching those of the respective α -decay energy gates used to produce them.

In the case of the $I = 1/2$ isomer in ^{199}At , the α branching ratio $b_\alpha \approx 1.0\%$ [109] was too low to observe the 6480 keV α decay. Instead, the 103(2)-141.0(1) keV, E3-M1 γ -ray cascade by which the $I = 1/2$ state decays to the $I = 9/2$ ground state [99] was used for the HFS extraction. The 103-keV E3 transition is strongly converted ($\alpha_{tot}(E3) = 180(15)$) and was not visible in the singles γ -ray spectrum. However a peak at 141 keV was observed (Fig. 6.5 - top panel). This peak was present in the spectra for runs with the lasers switched on, but not during those with the lasers switched off. Thus, it was identified as the aforementioned transition associated with the $I = 1/2$ state in ^{199}At .

The HFS of the $I = 1/2$ state in ^{199}At was extracted by gating on the 141-keV peak using two methods. The first approach employed a background subtraction technique in which three energy gates of equal width were used, shown by the vertical coloured lines in top panel of Fig. 6.5. One was placed upon the 141-keV peak (green lines), and two background gates were placed either side (blue and red lines). The number of counts from the two background gates were averaged and then subtracted from the integral of the peak gating condition. The second method plotted a singles γ -ray spectrum for each laser step and fitted the 141-keV peak with a Gaussian plus quadratic function, the latter used to account for the background the peak sat upon. The Integral of the Gaussian component was taken to be the number of counts in the peak.

The central panel of Fig. 6.5 shows the number of counts between the gates of the background subtraction method, as a function of laser wavenumber. The plots for the two background regions are in good agreement with one another. However, there is a clear excess in the number of counts from condition that gated upon the peak at certain laser frequencies, in comparison to those of the background conditions. The fact that there is not a constant excess of counts at all laser frequencies is further evidence that this transition does belong to ^{199}At , and not to some beam contaminant or background source.

The final results for the background subtraction method are plotted as the black data points in the bottom panel of Fig. 6.5. The red data points are the results from the peak fitting method. The two methods are in excellent agreement with one another, with the fitting method having slightly higher statistics and smaller errors.

6.3 Fitting of HFS data

After extraction of the HFS, a chi-squared minimisation routine was used to fit the data in order to extract values for central frequency of the HFS, from which the

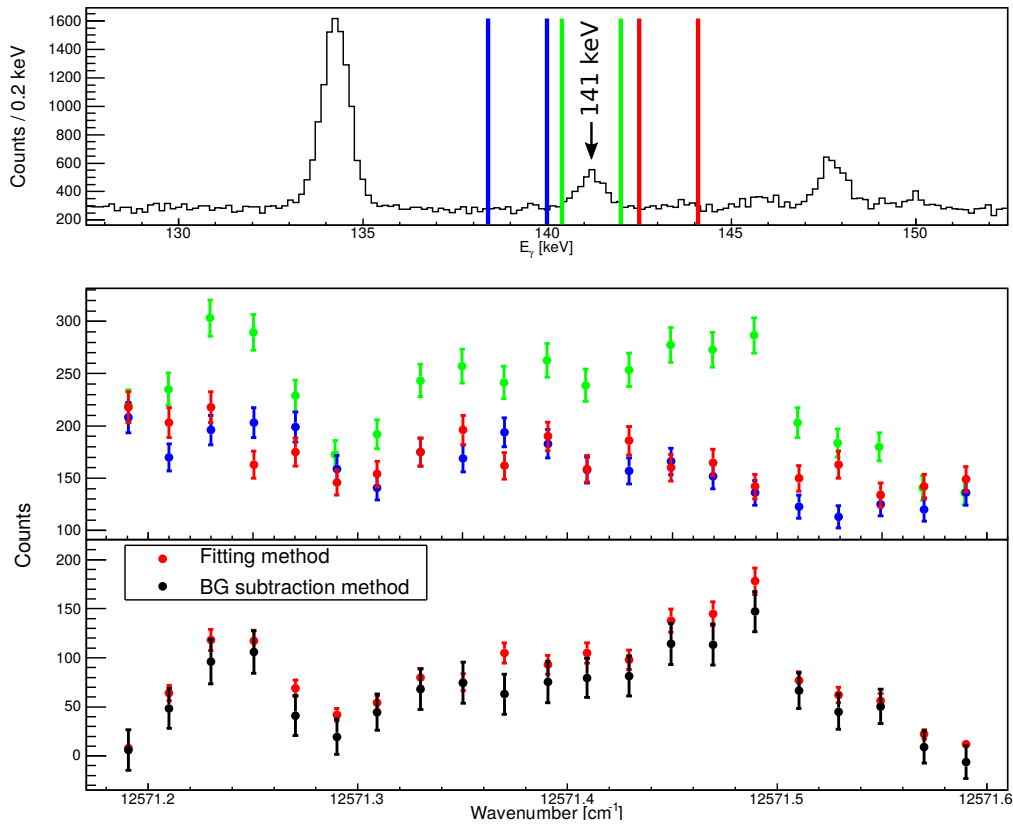


Figure 6.5: Top panel: the singles γ -ray spectrum measured during the laser scan of ^{199}At . Central panel: HFS spectra from gating on the 141 keV peak (green) and the background regions either side (blue and red). Bottom panel: comparison of the background subtraction (black) and fitting (red) method results.

isotope/isomer shifts are determined, and the a and b hyperfine parameters. A code was developed by the author of this work, henceforth referred to as the York code, which fitted the number of possible transitions between hyperfine levels with Voigt profiles [110] – a convolution of a Gaussian and a Lorentzian distribution. The intensity of each transition was determined by the theoretical strength using Equation 6.1, and the widths of each profile kept constant for each transition. The transition centroids were determined by the a and b hyperfine parameters, the values of which were used as parameters for the routine to minimise on when fitting the experimental data.

The results of the fitting of the $I = 1/2$ (top panel) and $I = 9/2$ (bottom panel) states in ^{197}At are displayed in Fig. 6.6. Only 9 blue lines are seen in the plot for the $I = 9/2$ state instead of the expected 10, this is due to the $F_i = 4 \rightarrow F_f = 4$ transition having an intensity 4×10^3 lower than the strongest, $F_i = 6 \rightarrow F_f = 6$ transition.

The code developed at York does not account for saturation and polarization

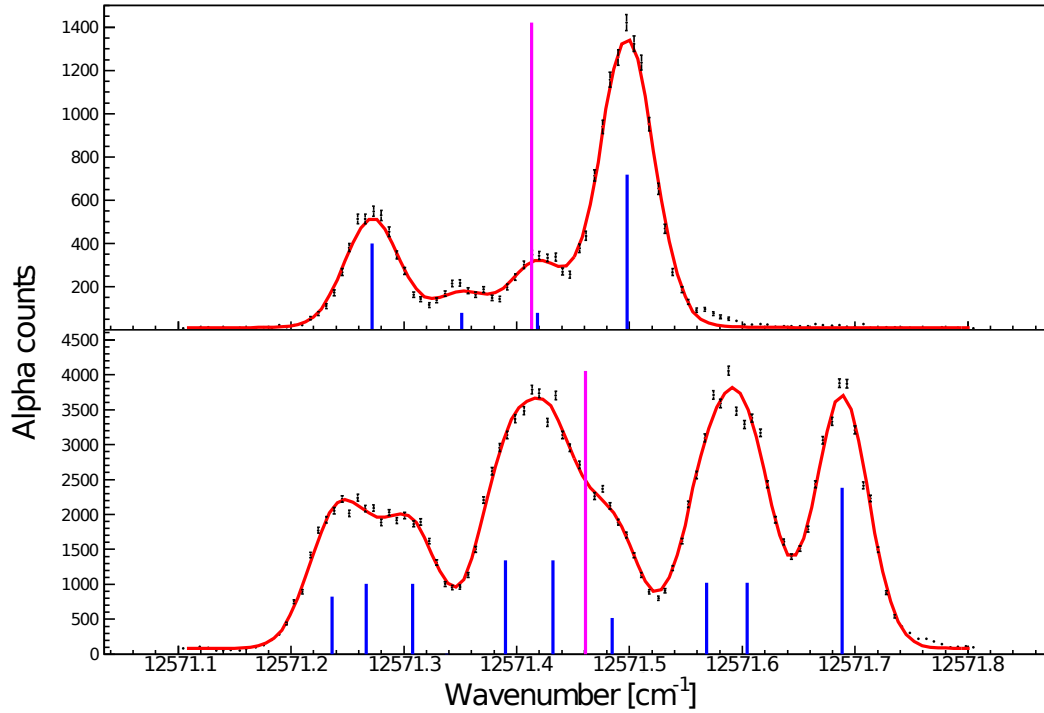


Figure 6.6: Fitting of HFS spectra for the ^{197}At $I = 1/2$ (top panel) and $I = 9/2$ (bottom panel) states using the York routine. The fits are shown by the red lines and the central frequency of the HFS by the vertical pink line. The vertical blue lines indicate the centroid positions for the different hyperfine transitions.

effects, or nonuniform population of the hyperfine levels by the laser used in the first resonant-excitation step. Accounting for such effects is not trivial, and so, a more sophisticated fitting procedure was developed by collaborators Maxim Seliverstov and Anatoly Barzakh from The Petersburg Nuclear Physics Institute, Gatchina. Table 6.3 gives a comparison of the results given by the two procedures, although in good agreement for the a and b factors for the $I = 9/2$ state, there is significant difference in the a factor for the $I = 1/2$ state and a large discrepancy between the isomer shift, $\delta\nu$, between the two states. As such, the final results presented in the following sections are taken from the fits made using the Seliverstov-Barzakh routine.

Table 6.2: Comparison of the York and the Seliverstov-Barzakh fitting routines for the a and b hyperfine parameters of, and the isomer shift, $\delta\nu$, between the $I = 1/2$ and $9/2$ states in ^{197}At .

Routine	$a(1/2)$ [MHz]	$a(9/2)$ [MHz]	$b(9/2)$ [MHz]	$\delta\nu$ [MHz]
York	-1224(15)	-334(6)	-753(67)	1698(113)
Seliverstov-Barzakh	-1235(10)	-342(4)	-690(50)	1868(106)

6.4 Changes in charge-radii and deformation across the At isotopic chain

The results for the isotope shifts relative to ^{211}At ($N = 126$), taken from the fitting of the HFS data, are given in Table 6.3. These are accompanied by the extracted values of the change in mean-squared charge radius relative to ^{211}At , $\delta\langle r^2 \rangle$, calculated using Equation 3.6. The atomic factors M and F were calculated using large-scale atomic calculations [111], giving values of $M_{795nm}^{SMS} = -580(100)$ GHz amu, and $F_{795nm} = -11470(570)$ MHz fm $^{-2}$.

The magnitudes of the quadrupole deformation parameters, $\langle \beta^2 \rangle^{1/2}$, corresponding to the $\delta\langle r^2 \rangle$ when compared to the droplet model [29, 112] are also given. These values were normalised such that the deformation of ^{209}At was set to be equal to that of the neighbouring isotope ^{208}Po . The latter was assessed using Grodzin's rule [113], from which a relationship between $E(2_1^+)$ and β_2 can be expressed as

$$\beta_2 = \frac{466 \pm 41}{A\sqrt{E(2_1^+)}} \quad (6.2)$$

where the uncertainty of ± 41 stems from the error in the fitting of the relationship to measured data [114]. A value of $E(2_1^+) = 685$ keV in ^{208}Po gave a quadrupole deformation of $\beta_2 = 0.086(8)$.

The results for the extracted values of $\delta\langle r^2 \rangle$ are plotted in Fig. 6.7 as a function of neutron number, along with the predictions of the DM (black-dashed lines) for nuclei of constant deformation. The error bars in the Fig 6.7 represent the statistical errors taken from the fits of the spectra, the majority of which are smaller than their respective data points.

Table 6.3: Tabulated data for the measured isotope shifts, $\delta\nu_{A,211}$ and calculated values for $\delta\langle r^2 \rangle_{A,211}$ with statistical errors given in round brackets and the systematic errors in curly braces. The respective $\langle \beta_2^2 \rangle^{1/2}$ parameters, extracted within the framework of the droplet model. The extracted $\langle \beta_2^2 \rangle^{1/2}$ for both the Berdichevsky & Tondeur (BT) [29], and Myers & Schmidt (MS) [112] parameterisations of the droplet model are given.

A	N	I	$\delta\nu_{A,211}$ [MHz]	$\delta\langle r^2 \rangle_{A,211}$ [fm ²]	$\langle \beta_2^2 \rangle^{1/2}$ (BT)	$\langle \beta_2^2 \rangle^{1/2}$ (MS)
195	110	(1/2)	6368(125)	-0.542(11){27}	0.22 ^{+0.01} _{-0.01}	0.18 ^{+0.01} _{-0.01}
		(7/2)	5569(125)	-0.473(11){24}	0.24 ^{+0.01} _{-0.01}	0.19 ^{+0.01} _{-0.01}
196	111	(3)	7404(156)	-0.634(13){32}	0.19 ^{+0.01} _{-0.01}	0.14 ^{+0.02} _{-0.02}
197	112	(1/2)	5916(125)	-0.505(11){25}	0.20 ^{+0.01} _{-0.01}	0.16 ^{+0.01} _{-0.01}
		(9/2)	7784(125)	-0.668(11){33}	0.16 ^{+0.01} _{-0.01}	0.11 ^{+0.02} _{-0.02}
198	113	(10)	7993(125)	-0.687(11){34}	0.14 ^{+0.02} _{-0.02}	0.08 ^{+0.03} _{-0.04}
		(3)	8262(125)	-0.710(11){35}	0.13 ^{+0.02} _{-0.02}	0.06 ^{+0.03} _{-0.06}
199	114	(1/2)	5230(156)	-0.447(13){22}	0.19 ^{+0.01} _{-0.01}	0.15 ^{+0.01} _{-0.01}
		(9/2)	7417(125)	-0.637(11){32}	0.14 ^{+0.02} _{-0.02}	0.08 ^{+0.03} _{-0.04}
200	115	(10)	7321(141)	-0.630(12){31}	0.12 ^{+0.02} _{-0.02}	0.05 ^{+0.04} _{-0.05}
		(3)	7726(125)	-0.665(11){33}	0.10 ^{+0.02} _{-0.03}	0.00 ^{+0.06} _{-0.00}
		(7)	7540(125)	-0.649(11){32}	0.11 ^{+0.02} _{-0.02}	0.02 ^{+0.05} _{-0.02}
201	116	(9/2)	6617(125)	-0.569(11){28}	0.11 ^{+0.02} _{-0.02}	0.05 ^{+0.03} _{-0.05}
202	117	(7)	6648(156)	-0.573(13){29}	0.08 ^{+0.02} _{-0.03}	0.00 ^{+0.05} _{-0.00}
		(3)	6967(156)	-0.600(13){30}	0.07 ^{+0.03} _{-0.05}	0.00 ^{+0.02} _{-0.00}
203	118	9/2	5650(125)	-0.486(11){24}	0.10 ^{+0.02} _{-0.02}	0.03 ^{+0.04} _{-0.03}
204	119	7	5575(125)	-0.481(11){24}	0.06 ^{+0.03} _{-0.05}	0.00 ^{+0.03} _{-0.00}
205	120	9/2	4318(100)	-0.372(9){19}	0.09 ^{+0.02} _{-0.02}	0.05 ^{+0.03} _{-0.05}
206	121	(6)	4201(125)	-0.362(11){18}	0.06 ^{+0.02} _{-0.06}	0.00 ^{+0.04} _{-0.00}
207	122	9/2	2984(125)	-0.257(11){13}	0.08 ^{+0.02} _{-0.02}	0.06 ^{+0.02} _{-0.04}
208	123	6	2517(125)	-0.217(11){11}	0.07 ^{+0.02} _{-0.02}	0.05 ^{+0.03} _{-0.05}
209	124	9/2	1530(125)	-0.137(11){7}	0.08 ^{+0.01} _{-0.02}	0.07 ^{+0.02} _{-0.02}
210	125	(5)	891(125)	-0.077(11){5}	0.08 ^{+0.02} _{-0.02}	0.07 ^{+0.02} _{-0.02}
211	126	9/2	0(0)	0.000(0){0}	0.09 ^{+0.01} _{-0.01}	0.09 ^{+0.01} _{-0.01}
217	132	9/2	-9479(125)	0.822(11){41}	0.21 ^{+0.01} _{-0.01}	0.22 ^{+0.01} _{-0.01}
218	133	(2)	-11363(164)	0.985(14){49}	0.23 ^{+0.01} _{-0.01}	0.24 ^{+0.01} _{-0.01}
219	134	(9/2)	-11769(156)	1.020(13){51}	0.22 ^{+0.01} _{-0.01}	0.24 ^{+0.01} _{-0.01}

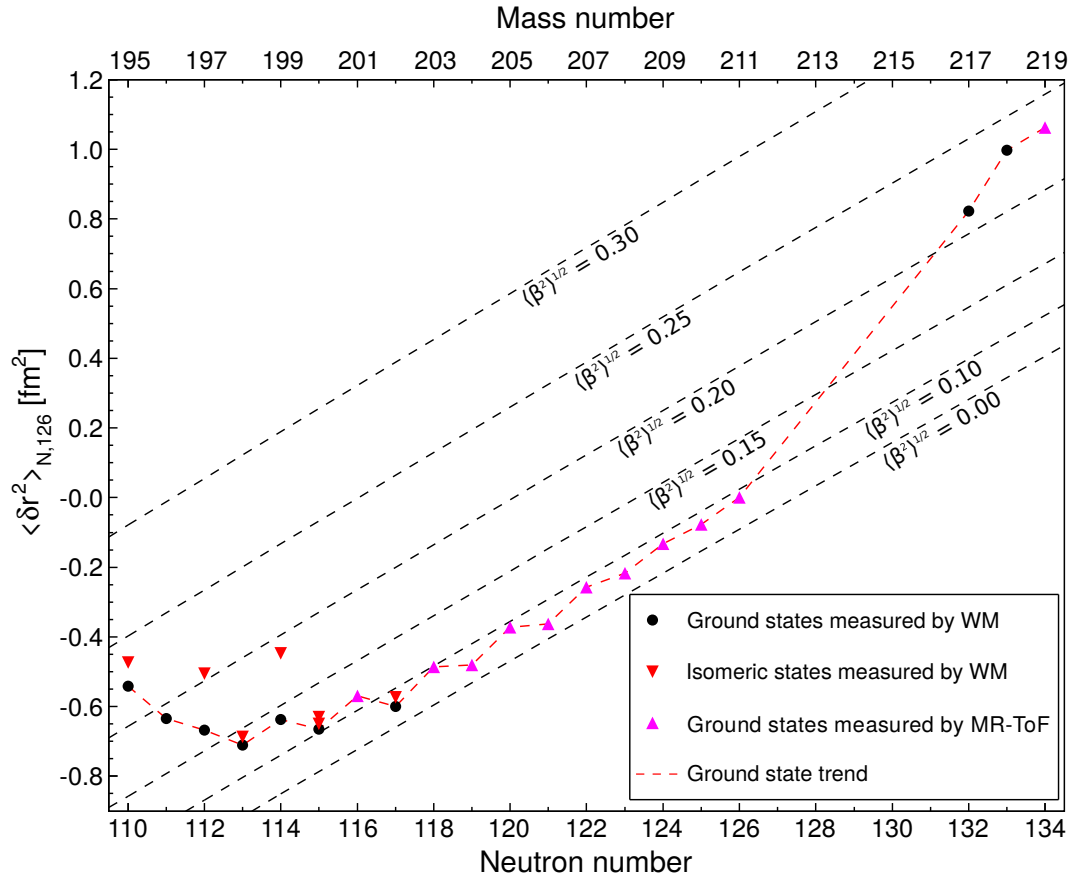


Figure 6.7: Change in mean-square charge radii for the At isotopic chain relative to ^{211}At ($N = 126$), as a function of neutron number. The data for ground states measured using the Windmill (black circles), the MR-ToF (pink, upward triangles), and the isomeric states measured by the Windmill (red, downward pointing triangles) are plotted. To guide the eye, the dashed red line connects the data points belonging to the ground states. The dashed black lines show the change in mean-square charge radius for At isotopes with fixed quadrupole deformation parameter, calculated using the droplet model [29, 112].

6.4.1 The ground states of the neutron-deficient ($N \leq 126$) At isotopes

The data plotted in Fig. 6.7 show that the ground-state charge radii of the neutron deficient At isotopes follow a spherical trend between ^{211}At and ^{208}At ($N = 126$ to $N = 123$). Beyond this point a gradual onset of mean-squared deformation is observed as neutron number decreases down to ^{198}At ($N = 113$), from where an even stronger deviation from sphericity is observed. This trend is reflected in the values of the deformation parameters, plotted in Fig. 6.8, which shows a rapid increase in deformation with decreasing neutron number. The departure of the ground states from

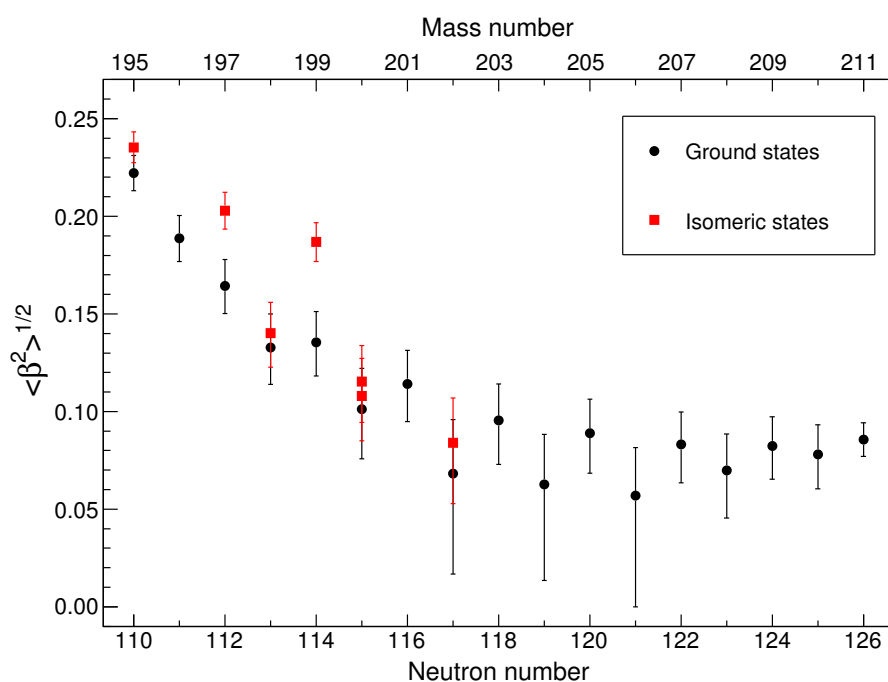


Figure 6.8: Ground (black) and isomeric (red) state quadrupole deformation parameters as a function of neutron number for the light At isotopes, taken from comparing the measured $\delta\langle r^2 \rangle$ values with predictions using the droplet model.

spherical shapes is highlighted further when comparing the results for the At isotopes to those of the Po and Pb isotopic chains, as shown in Fig. 6.9. The comparisons for the odd- and even- N isotopes are made separately in order to remove the effects of the odd-even staggering (OES), whereby odd- N isotopes have a smaller charge radius than the mean of their even- N neighbours. The plot shows the measured $\delta\langle r^2 \rangle_{N,126}$ for the three chains, normalised such that $\delta\langle r^2 \rangle_{N,126} / \delta\langle r^2 \rangle_{124,122}$, in order to remove uncertainty in the respective electronic factors. The data for the Pb and Po chains are taken from Refs. [17, 115, 116, 117], and [14, 19], respectively.

The At isotopes in the vicinity of the $N = 126$ shell closure are seen to follow the same trend as the Pb isotopes, indicating that they are spherical. As the neutron number decreases a deviation from this spherical trend is observed. This deviation is due to an onset of deformation similar to the one seen in the Po isotopes. The departure from sphericity is stronger in the At isotopes, than in the Po chain and appears more dramatic for the even- N isotopes.

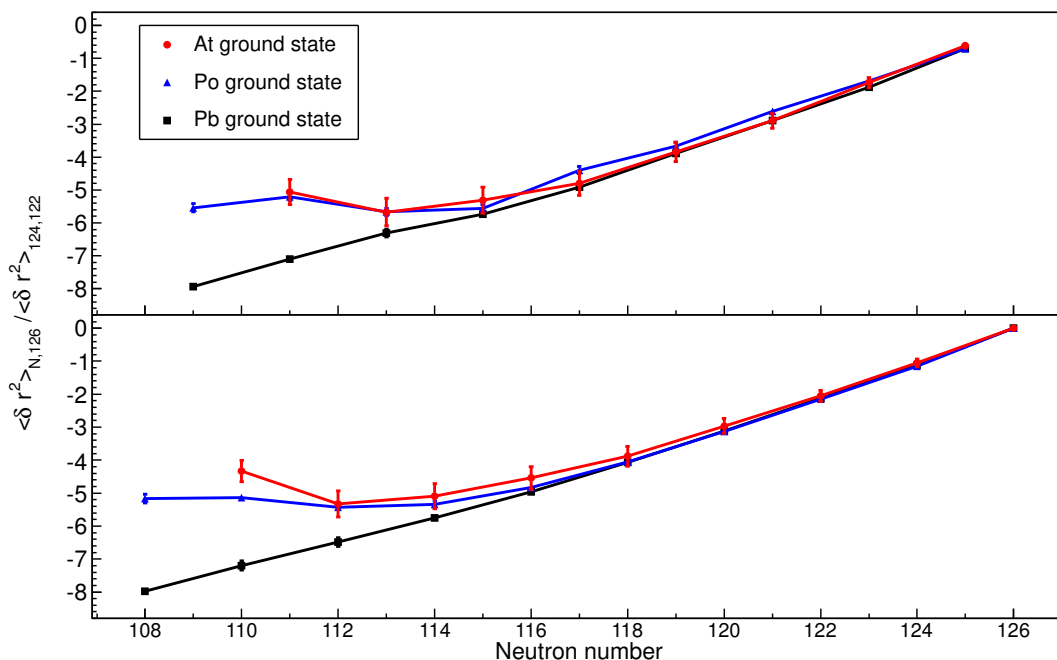


Figure 6.9: Comparison of the change in mean-squared charge radii relative to that of the $N = 126$ isotopes, for the At (red), Po (blue) and Pb (black) isotopic chains.

6.4.2 Cases for shape coexistence in the light At isotopes

As for the isomeric states, the difference in value of $\delta\langle r^2 \rangle$ and $\langle \beta^2 \rangle^{1/2}$ for the even- N isotopes indicates the presence of shape coexistence. This is particularly clear for $^{197,199}\text{At}$ ($N = 112, 114$); in both cases a nearly spherical $I = 9/2$ ground state is accompanied with a deformed $I = 1/2$ isomer. The magnitude of the difference in deformation between the two states reduces with neutron number. This trend can be extended to ^{195}At , where the $I = 7/2$ isomer has a greater deformation than the $I = 1/2$ ground state. The values of $\langle \beta^2 \rangle^{1/2}$ for the two states in ^{195}At are not distinguishable within the limits of their errors stemming mainly from the systematic uncertainty of the atomic F_{795nm} factor. However, their respective $\langle \delta r^2 \rangle$ values are clearly separable, indicating that this too is a case of shape coexistence.

As for the odd- N isotopes, no appreciable difference is seen in the values of $\delta\langle r^2 \rangle$ or $\langle \beta^2 \rangle^{1/2}$ for the ^{198}At and ^{200}At ground and isomeric states. Extraction of the quadrupole moments is required to truly understand whether or not there is any difference in shape of the ground and isomeric states. However, the extracted magnetic-dipole moments (discussed in Section 6.5) suggest that the states measured in the odd- N nuclei do not present cases of shape coexistence.

6.4.3 Odd-even staggering

The OES is a regular behaviour observed in nearly all isotopic chains. The phenomenon is understood to be due to the effect of pairing, which gives rise to enlarged zero-point vibration amplitudes in even- N nuclei, resulting in a wider potential well than that of neighbouring odd- N nuclei. The introduction of an odd neutron effectively blocks these vibrations and in doing so creates a sharper nuclear surface, resulting in a smaller charge radius relative to the neighbouring even- N nuclei.

The OES parameter, γ , provides a metric for the magnitude of the staggering between isotopes, and is defined as

$$\gamma = \frac{2\Delta\langle r^2 \rangle_{A-1,A}}{\Delta\langle r^2 \rangle_{A-1,A+1}}, \quad (6.3)$$

where $\Delta\langle r^2 \rangle_{A-1,A} = \langle r^2 \rangle_A - \langle r^2 \rangle_{A-1}$. For odd- N nuclei with mass number A , values of $\gamma < 1$ are expected. This is due to the blocking effect of unpaired neutrons, which reduces the size of the nuclear charge radius of odd- N isotopes, relative to the even- N neighbours. Values of $\gamma < 1$ are classed as “normal OES”, whereas those of $\gamma > 1$ are classed as “inverse OES”. Inverse OES has been observed in regions of the nuclear chart where octupole deformation is expected (see discussion in Section 6.4.3). As the degree of staggering is due to the ability of pairs to scatter into orbitals near the Fermi surface, it is expected that the value of γ should tend to 1 as the available valence space in a shell reduces.

The values of γ for odd- N isotopes of At, Pb and Po are plotted as a function of neutron number in Fig. 6.10, the dashed horizontal line represents $\gamma = 1$. The dashed vertical lines indicate neutron subshell closures for the spherical shell model.

The plot shows that near the $N = 126$ shell closure, the value of γ is approximately 1 for all three chains, as expected. The magnitude of the staggering is observed to increase with decreasing neutron number more rapidly in the At, than in the Pb and Po isotopes. However, in contrast to the At and Pb data, the Po data are seen to depart from this trend with no obvious systematic for the $N = 115, 117$ and 119 isotopes.

As well as this general trend in staggering strength, large jumps in the values of γ

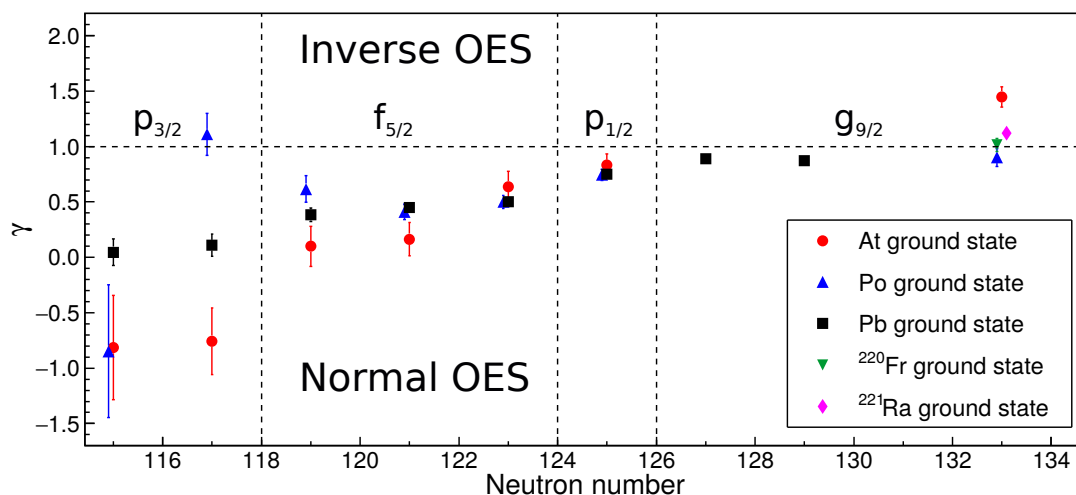


Figure 6.10: Comparison of values of the odd-even staggering parameter, γ , for the odd- N isotopes of the At (red circles), Po (blue triangles) and Pb (black squares) chains. Data points for ^{220}Fr (green downwards triangle) and ^{221}Ra (pink diamond) are also included.

are observed when boundaries between neutron subshells are crossed. This provides evidence that the At isotopes in the vicinity of the $N = 126$ closure can still be well described as spherical-shell model nuclei.

For neutron numbers less than $N = 115$, the value of γ drastically changes, due to the strong onset of deformation. This also indicates an abrupt change in the At nuclei in the $N < 115$ region, going from being well described by the spherical shell model, to having a predominantly collective behaviour.

Cases for octupole deformation in the heavy At isotopes ($N > 126$)

An inversion of the normal OES has been observed in regions where octupole deformation is predicted, such as in the Fr [118, 119, 120], Rn [121] and Ra [51, 122] isotopes, and the $^{153-155}\text{Eu}$ [123] where octupole deformation is also predicted due to the coupling of the $\pi h_{11/2}-\pi d_{5/2}$, and the $\nu i_{13/2}-\nu f_{7/2}$ orbitals. To date there has been no satisfactory quantitative description as to why octupole degrees of freedom have this effect on the OES of nuclear charge radii, it has just been observed that this phenomenon manifests where octupole collectivity is expected. This behaviour was qualitatively explained in [122] as a result of Nilsson orbitals of same Ω but different parity crossing at certain degrees of quadrupole deformation. This introduces an octupole interaction, which lowers the energy of the system with increasingly reflection-assymeric, or octupole geometries. Calculations have shown that the unpaired neutron in odd- N systems polarizes the quadrupole-octupole potential

energy surface, making octupole shapes more stable than in the even- N neighbours. This additional polarisation in odd- N nuclei increases their mean-squared radii, resulting in the observed inversion of the OES.

Nuclei possessing degrees of octupole deformation are not only of interest to the field of nuclear structure physics, but are important for research of physics beyond the standard model. These so-called “pear-shaped” nuclei play a key role in the search for permanent atomic electric-dipole moments (EDM). The existence of an EDM would indicate a violation of either time-reversal or charge-parity symmetry to a level that cannot be currently described by the Standard Model. Nuclear octupole deformation is expected to increase the experimental signal for the presence of an atomic EDM by a factor of 10^2 to 10^3 [124]. As such, identification of nuclei with non-zero β_3 values is of importance to this area of research.

The heavy At isotopes display an inversion of the normal OES, with the odd neutron ^{218}At ($N = 133$) nucleus having a larger charge radius than the average of its two even neutron neighbours, ^{217}At and ^{219}At . In the case of ^{218}At , $\gamma = 1.45(9)$, which can be compared to the γ values of its isotones $\gamma(^{217}\text{Po}) = 0.90(8)$, $\gamma(^{220}\text{Fr}) = 1.02(6)$, $\gamma(^{221}\text{Ra}) = 1.121(2)$. For ^{217}Po the γ value is less than one, as is expected for odd- N isotopes. In contrast the value of γ for ^{218}At is greater than 1, indicating a clear inversion and evidence for the presence of octupole collectivity in the heavy At isotopes.

Compared to the $N = 133$ Fr and Ra isotones the magnitude of the inverse OES in At is much greater. This could suggest that the degree of polarisation of the heavy At nuclei due to octupole collectivity is greater than in the Ra and Fr chains. However, at present there are not enough data available to ascertain whether or not there is a link between the magnitude of the inverted OES and the degree of octupole deformation.

6.5 Magnetic dipole moments

In the framework of the spherical shell model the magnetic moment, μ , of a nucleus is defined by the unpaired nucleons. Thus, the spherical shell model predicts $\mu = 0$ for even-even nuclei. For odd- A nuclei, this single-particle picture defines μ of the nucleus to be equal to that of the unpaired nucleon. The Schmidt values, μ_S , give the predicted values of μ for a single-particle nucleus [125, 126], such that

$$\mu_S = j \left(g_l \pm \frac{g_s - g_l}{2l + 1} \right) \mu_N, \quad (6.4)$$

where μ_N is the nuclear magneton, and $g_l = 1(0)$ is the orbital g -factor, and $g_s = 5.58(-3.82)$ is the spin g -factor for a free proton (neutron). The values of μ_S give the extreme limits to what the value of μ of a nucleus can be.

A better agreement between calculated and experimental values of μ can be found by using effective spin g -factors, approximated as $g_{eff} = 0.6g_s$. This quenching of the spin g -factors accounts for the fact that the proton and neutrons are not free particles when bound within a nucleus. By substituting g_{eff} for g_s in Equation 6.5, the magnetic moments of the quenched system, μ_q can be calculated. When pertinent to the following discussions, the values μ_S and μ_q will be compared to the values of μ extracted from the fits of the HFS.

In odd-odd nuclei, the magnetic moment of the two unpaired nucleons couple. The total magnetic moment of the nucleus can be calculated using the additivity rule [127], such that

$$\mu = \frac{I}{2} \left[g_\pi + g_\nu + (g_\pi - g_\nu) \frac{j_\pi(j_\pi + 1) - j_\nu(j_\nu + 1)}{I(I + 1)} \right], \quad (6.5)$$

where g is the g -factor, related to the magnetic moment of the nucleus by

$$g = \frac{\mu}{I} \quad (6.6)$$

From these relationships, the magnetic moments for spherical shell model nuclei can be predicted by using the g -factors from neighbouring odd- A nuclei for the values of g_ν and g_π . The predicted values can then be compared to those extracted from the experimental data in order to give an insight as to whether the nucleus has a single-particle nature, or a more collective one.

The magnetic moments calculated from the hyperfine parameters, a , taken from fits of the HFS data, are presented in Table 6.4 and plotted as a function of neutron number in Fig. 6.11. The values of μ were evaluated by using the expression

$$\mu_A = \mu_0 \frac{I_A}{I_0} \frac{a_A}{a_0} [1 + \Delta], \quad (6.7)$$

where A and 0 denote the isotope of interest and a reference isotope, respectively. The symbol Δ represents the hyperfine anomaly, a correction that is typically $<1\%$ [47]; the systematic errors for μ in Table 6.4 include a conservative 2% error to account for Δ . The value of μ_0 used was taken from [128], which measured the magnetic g -factor $g = 0.917(16)$ for ^{211}At , giving $\mu_0 = 4.13(7) \mu_N$.

Table 6.4: The hyperfine parameters a , extracted from fitting the HFS, and the respective magnetic moments for the At nuclei.

A	N	I	a [MHz]	μ [μ_N]
195	110	(1/2)	-1287(35)	1.61(6)
		(7/2)	-424(11)	3.71(13)
196	111	(3)	-498(15)	3.74(14)
197	112	(1/2)	-1235(25)	1.55(5)
		(9/2)	-342(8)	3.85(13)
198	113	(10)	-102(3)	2.55(10)
		(3)	-538(12)	4.04(13)
199	114	(1/2)	-1275(45)	1.60(7)
		(9/2)	-351(8)	3.96(12)
200	115	(10)	-108(3)	2.69(10)
		(3)	-570(13)	4.28(14)
		(7)	-271(7)	4.74(17)
201	116	(9/2)	-357(8)	4.03(13)
202	117	(7)	-259(9)	4.54(19)
		(3)	-554(16)	4.16(15)
203	118	9/2	-357(8)	4.02(13)
204	119	7	-276(7)	4.84(17)
205	120	9/2	-365(7)	4.11(13)
206	121	(6)	-295(9)	4.43(17)
207	122	9/2	-368(8)	4.15(13)
208	123	6	-298(10)	4.48(18)
209	124	9/2	-368(8)	4.14(13)
210	125	(5)	-379(10)	4.74(16)
211	126	9/2	-367(8)	4.14(0)
217	132	9/2	-329(8)	3.70(12)
218	133	(2)	-239(13)	1.20(7)
219	134	(9/2)	-311(8)	3.50(12)

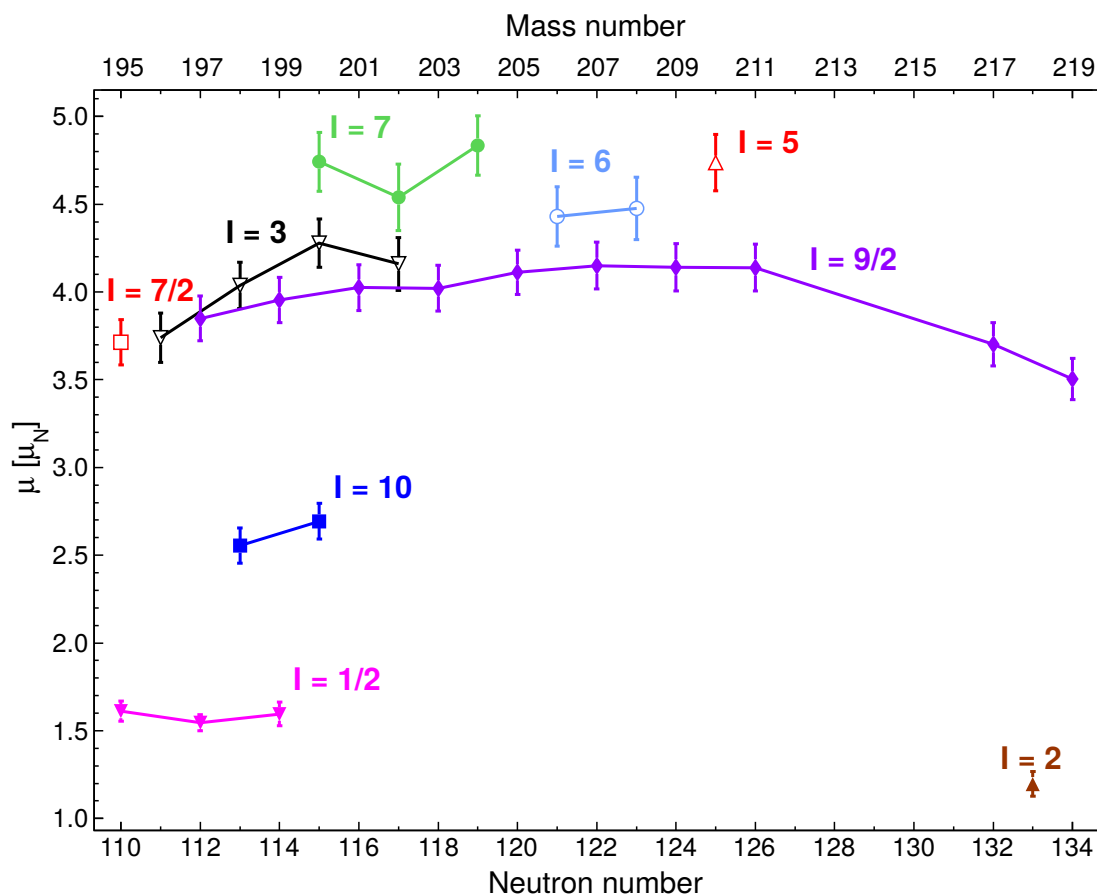


Figure 6.11: The magnetic moments of the different states in the At isotopes, as a function of neutron number.

6.5.1 Even- N isotopes

Figure 6.12 displays the values for μ for the $I = 9/2$ states in the even- N At isotopes, as a function of neutron number, along with those of the $I = 9/2$ states in the Bi isotopic chain. The solid red line represents the value for $\mu(^{209}\text{Bi}) = 4.0810(4) \mu_N$, taken from a measurement of the g -factor of the $I = 9/2$ ground state in ^{209}Bi [129]. The ground state in ^{209}Bi is a single proton in a $\pi 1h_{9/2}$ orbital, coupled to a doubly-magic ^{208}Pb core. Therefore, $\mu(^{209}\text{Bi})$ can be used as a reference value for other nuclei with an unpaired proton occupying a $\pi 1h_{9/2}$ orbit.

The value of $\mu(^{209}\text{Bi})$ differs from that of $\mu_S = 2.62 \mu_N$, and $\mu_q = 3.54 \mu_N$ for a proton in a $h_{9/2}$ orbital. In fact, this is the largest observed difference between a measured value of μ and μ_S , for a nucleus with a single particle outside of a doubly-magic core. Arima and Horie explained this discrepancy as an effect of first-order core polarisation [126, 130], a result of mixing between the 0^+ ground state, and the M1 giant resonance state (GRS) of the ^{208}Pb core. The GRS is made of two states;

$\pi 1h_{9/2} \otimes \pi 1h_{11/2}^{-1}$ proton, and $\nu 1i_{11/2} \otimes \nu 1i_{13/2}^{-1}$ neutron state. These 1p-1h spin-flip excitations are highly collective and involve all the protons in the $\pi 1h_{11/2}$, and all the neutrons in the $\nu 1i_{13/2}$ orbitals. This means that although the admixture between the GRS and ground state of the ^{208}Pb core is small (admixture of GRS ≈ 0.1), a significant modification is made to the values of μ .

The data plotted in Fig. 6.12 shows that the magnetic moments of the At isotopes are in good agreement with those of the Bi nuclei. This indicates that as in the Bi isotopes, there is a strong presence of core polarisation in the $I = 9/2$ ground states of the At isotopes with $N \leq 126$. In these At isotopes, the occupancy of the $\nu 1i_{13/2}$ orbital reduces with neutron number, thus, the number of neutrons involved in the excitation of the core is reduced. This results in the lowering in value μ as neutron number decreases, with a trend away from $\mu(^{209}\text{Bi})$ and towards $\mu_S(\pi 1h_{9/2}) = 2.62 \mu_N$ ($\mu_q(\pi 1h_{9/2}) = 3.54 \mu_N$).

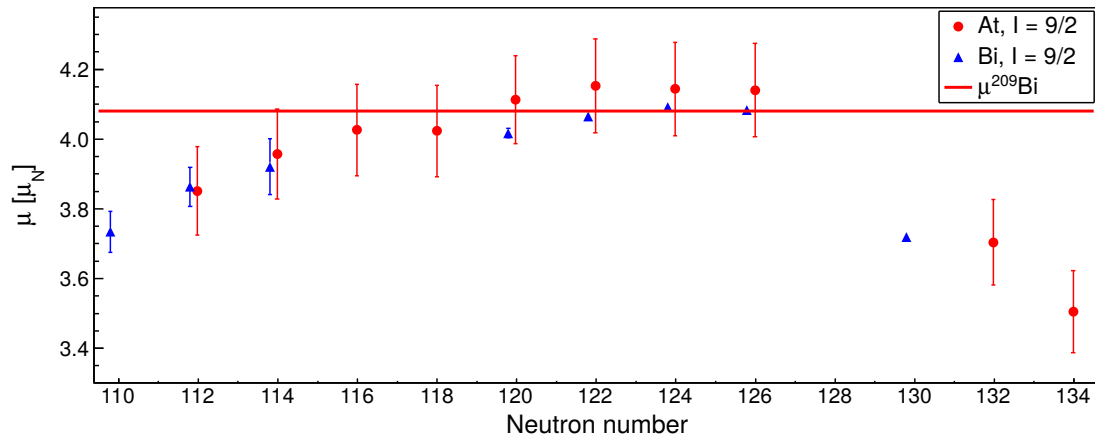


Figure 6.12: The values of μ for the $I = 9/2$ states in the At (red circles), and Bi (blue triangles) [129, 131, 132] isotopic chains. The red horizontal line represents the magnetic moment of ^{209}Bi .

The $I = 7/2$ state in ^{195}At , which possesses a mixed $\pi 1h_{9/2}/\pi 2f_{7/2}$ configuration, has $\mu = 3.71(13) \mu_N$. This value follows the trend of lowering values of μ with decreasing neutron number, in the $I = 9/2$ states of the even- N At isotopes, which possess pure $\pi 1h_{9/2}$ configurations. The experimental result is compatible with a theoretical value of $\mu = 3.2 \mu_N$, for a deformed $7/2^-$ [514] Nilsson orbital with $\beta_2 = -0.2$ [133].

As in the neutron deficient At nuclei, the $I = 9/2$ states in the neutron-rich At isotopes display a departure from $\mu(^{209}\text{Bi})$. This divergence is also related to a reduction in the polarisation of the core. However in this case, it is due to the filling of the $\nu 1i_{11/2}$. Filling of the $\nu 1i_{11/2}$ orbital means there are fewer holes available in to take part in 1p-1h excitations, and so the degree of core polarisation is reduced.

The magnetic moments for the $I = 1/2$ states in $^{195,197,199}\text{At}$ are plotted as a function of neutron number in Fig. 6.13, together with the magnetic moments of the $I = 1/2$ states in the Tl and Bi isotopes. These are the Tl $\pi(0p-1h)$ spherical ground states and possess a $\pi 3s_{1/2}$ configuration. In the Bi isotopes the $I = 1/2$ states are due to $\pi(2p-1h) \pi 3s_{1/2}^{-1} \otimes \pi 1h_{9/2}^2$ intruder configurations. The At data points are in good agreement with the Tl and Bi data sets, indicating that these too are $\pi 3s_{1/2}^{-1}$ intruder configurations due to a $\pi(1p-1h)$ excitations across the $Z = 82$ shell gap.

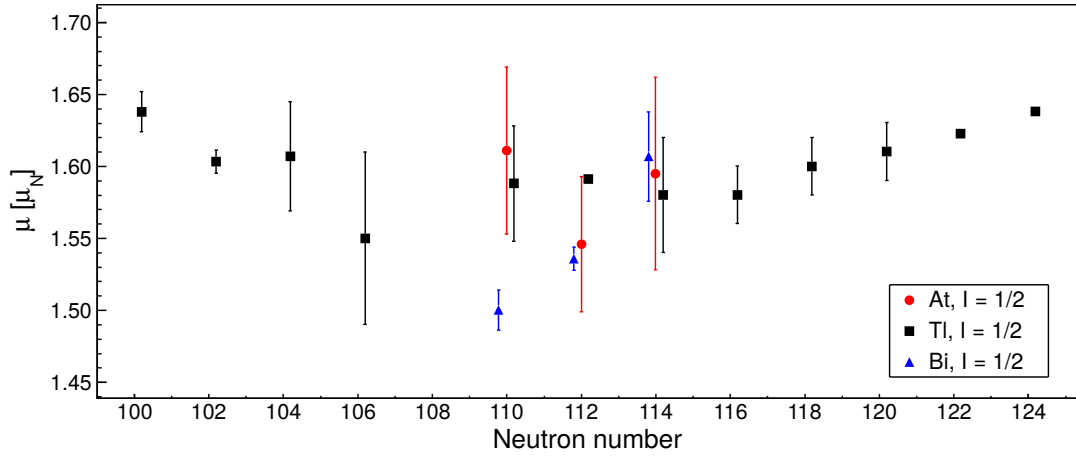


Figure 6.13: Comparison of the magnetic-dipole moment for the $I = 1/2$ states in At (red circles), Tl [21, 134, 135, 136, 137] (black squares), and Bi [132] (blue triangles) isotopic chains.

6.5.2 Odd- N isotopes

The magnetic moments for the odd- N At nuclei are plotted along with those of the Fr and Bi isotopes for the $I = 3, 6, 7$ and 10 states in Fig. 6.14 (a), (b), (c) and (d), respectively. The dashed lines in the figures represent the estimates for the magnetic moments calculated using the additivity rule, μ_{add} . Calculations of μ_{add} were made for a $\pi h_{9/2}$ proton, coupled to a $\nu 3p_{3/2}$, $\nu 3p_{1/2}$, $\nu 2f_{5/2}$, $\nu 2f_{7/2}$ and $\nu 1i_{13/2}$, for the $I = 3, 5, 6, 7$ and 10 states in At, respectively. The values of g_π and g_ν used for the μ_{add} calculations were taken from measurements on neighbouring odd- A nuclei, with known proton and neutron configurations, such that for At_N , $g_\pi = g(\text{At}_{N+1})$ and $g_\nu = g(\text{Po}_N)$.

The data show that the magnetic moments of the At states are in acceptable agreement with those of the same spin in the Fr and Bi isotopes, and the μ_{add} calculations, indicating that these states have well defined configurations. The $I = 5$ state in ^{210}At has $\mu = 4.74(16) \mu_N$, consistent with $\mu_{add}(\pi 1h_{9/2} \otimes \nu 3p_{1/2}) = 4.75 \mu_N$.

From the above, it was possible to assign the states with the configurations shown in Table 6.5.

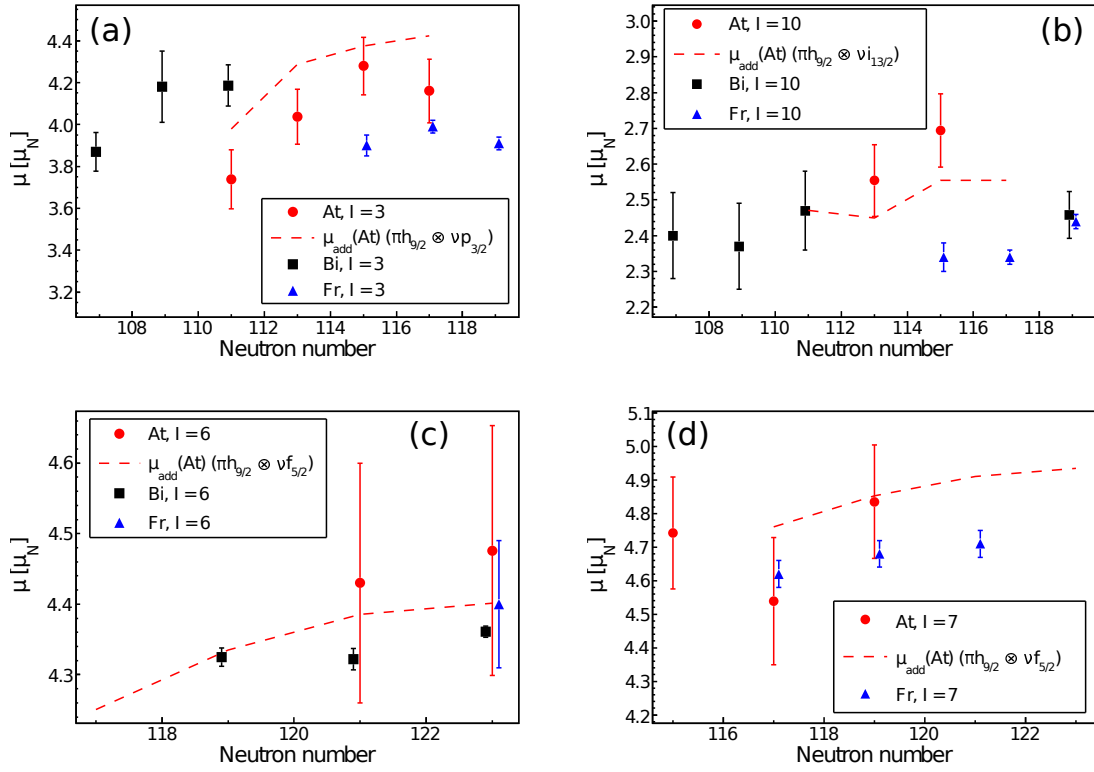


Figure 6.14: Magnetic moments for the (a) $I = 3$, (b) $I = 10$, (c) $I = 6$ and (d) $I = 7$ states in the odd- N At nuclei (red circles) along with their Bi (black squares) and Fr (blue triangles) isotones.

Table 6.5: Configuration assignments for the $I = 3, 6, 7$ and 10 states in the odd- N At isotopes.

I	Configuration
3	$\pi 1 h_{9/2} \otimes \nu 3 p_{3/2}$
5	$\pi 1 h_{9/2} \otimes \nu 3 p_{1/2}$
6	$\pi 1 h_{9/2} \otimes \nu 2 f_{5/2}$
7	$\pi 1 h_{9/2} \otimes \nu 2 f_{5/2}$
10	$\pi 1 h_{9/2} \otimes \nu 1 i_{13/2}$

As for the $I = 2$ state in ^{218}At , a value of $\mu = 1.20(7) \mu_N$ was extracted from the HFS fits. Estimates made with the additivity rule using theoretical μ_S and μ_q values, combined with $\mu(^{219}\text{At})$ are shown in Table 6.6, none of which are in agreement with the experimental value. The closest is that of a $\pi 1h_{9/2} \otimes \nu 3p_{1/2}$ configuration, however, such a state has not been observed in neighbouring nuclei. The disagreement between the extracted and calculated values of $\mu(^{218}\text{At})$ so far remains unexplained. However, this could be another indication for the presence of octupole collectivity in this region of the nuclear chart.

Table 6.6: Possible configurations for $I = 2$ state in ^{218}At .

Configuration	$\mu_S [\mu_N]$	$\mu_q [\mu_N]$
$\pi 1h_{9/2}(^{219}\text{At}) \otimes \nu 2g_{9/2}$	0.35	0.52
$\pi 1h_{9/2}(^{219}\text{At}) \otimes \nu 1i_{11/2}$	0.19	-0.15
$\pi 1h_{9/2}(^{219}\text{At}) \otimes \nu 3p_{1/2}$	0.07	1.60
$\pi 1h_{9/2}(^{219}\text{At}) \otimes \nu 3d_{5/2}$	4.13	3.62

None of the magnetic moments for the states in the odd- N At isotopes are in agreement with additivity estimates involving a $\pi 3s_{1/2}^{-1}$ intruder configurations. Therefore, the valence proton is assigned to a $\pi h_{9/2}$ orbital for all states in the odd- N At isotopes. Due to this, it would be expected that the shapes of the odd- N At nuclei in these states would be similar. The small differences observed in the data (see Figs. 6.7 and 6.8) are due to differing levels of core polarisation from the valence neutron for different orbitals. Thus, based on the extracted values of μ and $\delta\langle r^2 \rangle$, the ground and isomeric states of the odd- N At isotopes measured in this work do not present cases for shape coexistence.

Conclusion

This thesis presents the results from studies of the ^{178}Au nucleus and of the At isotopic chain, performed using the Windmill decay station at the ISOLDE facility.

By combining the ISOL method with the in-source laser ionisation technique, isomerically pure beams of two states in ^{178}Au were achievable. Due to this, it was possible to perform α -decay studies upon the two states, independently of one another.

The results from these studies identified the presence of a low-spin ground, and a high-spin isomeric state. The half-lives and fine-structure α decay of the two states were investigated, and a number of excited states and γ transitions were identified in the ^{174}Ir daughter nucleus. Based on the results from the ISOLDE decay study and the known structures of neighbouring isotopes, tentative configuration assignments were given for $^{178g,m}\text{Au}$.

The presence of two unhindered α decays from the high-spin isomer, followed by highly-converted γ rays, was observed. A tentative explanation for this would be the presence of a triplet of states with different shapes in ^{174}Ir . However, further work and analysis is required to understand these fine-structure decays fully.

The HFS of $^{195-211,217-219}\text{At}$ were measured for the first time and their respective isotope shifts, mean-square charge radii and magnetic moments extracted. The results display a strong onset of deformation as the neutron number decreases away from the $N = 126$ shell closure towards the $N = 104$ midshell. Clear cases for shape coexistence were identified in $^{195,197,199}\text{At}$, with a significant difference in charge radius of the $I = 1/2$ and $I = 9/2$ ($I = 7/2$ in the case of ^{195}At) states in these isotopes. In addition, an inversion of the normal OES was observed in the heavy At isotopes above the $N = 126$ shell closure, providing an indication for the presence of octupole collectivity in the heavy At isotopes.

The magnetic moments of the $I = 9/2$ states in the even- N isotopes have a single-particle like nature, consistent with a $\pi 1h_{9/2}$ configuration. The $I = 1/2$ states in

^{195,197,199}At have magnetic moments consistent with those of the $I = 1/2$ states in the Tl and Bi chains, indicating that they possess $\pi 3s_{1/2}^{-1}$ intruder configurations. It is these intruder states that are responsible for the cases of shape coexistence observed in these nuclei.

The magnetic moments of the odd- N isotopes, excepting the $I = 2$ state in ²¹⁸At, are consistent with those of the same spin in the Bi and Fr isotopic chains. The assigned configurations are all consistent with a $\pi 1h_{9/2}$ proton, with no evidence for a $\pi 3s_{1/2}^{-1}$ intruder configuration observed in any of the investigated states. Due to this absence of intruder-state configurations there is no notable difference between the shapes of the isomers in the odd- N At isotopes.

As for the $I = 2$ state in ²¹⁸At, no coupled proton-neutron configuration could explain the experimentally measured magnetic moment.

7.1 Future work

The final analysis of the decay data for the two states in ¹⁷⁸Au is ongoing, in particular the two 5521-472.1 and 5571-421.4 keV fine-structure decays. An explanation for these two anomalous decay paths has proven difficult and is still under discussion, the final interpretation will be presented in a forthcoming publication [72]. However, preliminary results from the JR121 experiment conducted at JYFL [83] have confirmed the presence of these fine-structure decays. The level of statistics in this data set is much higher than in the ISOLDE data, and so further analysis of the JYFL data may shed more light on the nature of these decays.

A recent α -decay study of ¹⁸²Tl by Van Beveren *et al.* [138] identified a number of new α decays, as well as a number of low-lying states in the α -decay daughter nucleus, ¹⁷⁸Au. However, the α decay of ¹⁸²Tl is complex, and only partial α -decay schemes could be drawn from the results. With the new structural information of ^{178g,m}Au available from the ISOLDE study, it may be possible to revisit ¹⁸²Tl and draw some more conclusions from the data. At present, there are no future plans to perform any further dedicated decay studies on ¹⁷⁸Au.

As for the laser-spectroscopy studies on the At isotopic chain, it would be interesting to observe whether or not the trend in change of deformation for the different states in the light, even- N At isotopes persists. This would require the measurement of the HFS of $I = 1/2$ and $I = 7/2$ states in ¹⁹³At, which possess half-lives of $t_{1/2} = 28(5)$ and $21(5)$ ms respectively, comparable to that of ¹⁹¹Po ($t_{1/2} = 22(1)$ ms) which was measured using the same technique. In addition to this, ¹⁹³At has a low-lying $\pi 1i_{13/2}$ intruder state with a $t_{1/2} = 27(4)$ ms, which is comparable to those of the other two

states. Assuming the production cross section of the $I = 13/2$ state is similar to that of the $I = 1/2$ and $7/2$ states, then it too should be accessible. It would be of interest to see by how much the charge radius of this state would differ to those with $\pi 1h_{9/2}$ and $\pi 3s_{1/2}^{-1}$ configurations.

Such a measurement would require either extended run times, which pose a challenge for the stability of the laser system, or significant ion source development in order to reduce the release times of reaction products from the target matrix. There is an upgrade to the CERN accelerator facility that is planned for 2020, which will raise the energy of the primary proton beam delivered to ISOLDE from 1.4 GeV to 2 GeV, and increase in the proton beam intensity by a factor 2 to 3 [54]. The higher energy alone will increase the cross section of the fragmentation and spallation reactions by a factor between 2 and 10 of the current facility. These upgrades will improve the production yields of more exotic nuclides, making them experimentally accessible at ISOLDE.

Measurements of the HFS of $^{212-216}\text{At}$ and those with $A \geq 220$ would be of interest for the purpose of seeing at what point the inverse OES begins, for how long it persists, and how large its magnitude is. This would also provide further information on the “kink” phenomenon, the observation that the average rate of change in mean-squared charge radius doubles when crossing the $N = 126$ shell closure. Coulex studies made in these isotopes could verify whether or not there is any relationship between inverse staggering and the expected/experimentally measured values of the octupole deformation parameter, β_3 . This investigation could be expanded into a systematic study of the $Z > 82$, $N > 126$ region, using the complimentary laser spectroscopy-Coulex techniques. However, it is impossible to perform laser-spectroscopy studies upon these isotopes within the foreseeable future, due to their nano- to microsecond half-lives.

For the At chain, evaluation of the spectroscopic quadrupole moments is ongoing, but any values extracted would have significant errors due to the low resolution of the in-source laser spectroscopy method. An increase in resolution can be achieved by using the Perpendicularly Illuminated Laser Ion Source Trap (PI-LIST) [139], or a collinear laser-spectroscopy method such as those used by the COLLAPS and CRIS collaborations. The PI-LIST [20] is an upgrade to the Laser Ion Source Trap (LIST) that reduces the resolution of transition lines to 100 MHz. However, there is a sacrifice in the ionisation efficiency by a factor of 100-300.

References

- [1] C. Thibault et al. Direct measurement of the masses of ^{11}Li and $^{26-32}\text{Na}$ with an on-line mass spectrometer. *Physical Review C*, 12(2):644–657, 1975.
- [2] C. Détraz et al. Mapping of the onset of a new region of deformation: The masses of ^{31}Mg and ^{32}Mg . *Nuclear Physics A*, 394(3):378–386, 1983.
- [3] E. K. Warburton et al. Mass systematics for $A = 29-44$ nuclei: The deformed $A \sim 32$ region. *Physical Review C*, 41(3):1147–1166, 1990.
- [4] P. Möller, A. J. Sierk, T. Ichikawa, and H. Sagawa. Nuclear ground-state masses and deformations: FRDM(2012). *Atomic Data and Nuclear Data Tables*, 109-110:1–204, 2016.
- [5] L. P. Gaffney et al. Studies of pear-shaped nuclei using accelerated radioactive beams. *Nature*, 497(7448):199–204, 2013.
- [6] H. Morinaga. Interpretation of some of the excited states of $4n$ self-conjugate nuclei. *Physical Review*, 101(1):254–258, 1956.
- [7] K. Heyde and J. L. Wood. Shape coexistence in atomic nuclei. *Reviews of Modern Physics*, 83(4):1467–1521, 2011.
- [8] D. J. Rowe and J. L. Wood. *Fundamentals of nuclear models: foundational models*. World Scientific Publishing Co. Pte. Ltd., first edition, 2010.
- [9] D.R. Tilley, H.R. Weller, and C.M. Cheves. Energy levels of light nuclei $A = 16-17$. *Nuclear Physics A*, 564(1):1–183, 1993.
- [10] J. L. Wood et al. Electric monopole transitions from low energy excitations in nuclei. *Nuclear Physics A*, 651(4):323–368, 1999.
- [11] A. Siivola. Alpha-active gold isotopes. *Nuclear Physics A*, 109(1):231–235, 1968.

- [12] J. G. Keller et al. Cold fusion in symmetric ^{90}Zr -induced reactions. *Nuclear Physics A*, 452(1):173–204, 1986.
- [13] P. M. Davidson et al. Non-yrast states and shape co-existence in light Pt isotopes. *Nuclear Physics A*, 657(3):219–250, 1999.
- [14] M. D. Seliverstov et al. Charge radii of odd-A $^{191-211}\text{Po}$ isotopes. *Physics Letters, Section B: Nuclear, Elementary Particle and High-Energy Physics*, 719(4-5):362–366, 2013.
- [15] J. Bonn et al. Sudden change in the nuclear charge distribution of very light mercury isotopes. *Physics Letters B*, 38(5):308–311, 1972.
- [16] G. Ulm et al. Isotope shift of ^{182}Hg and an update of nuclear moments and charge radii in the isotope range ^{181}Hg - ^{206}Hg . *Zeitschrift für Physik A Atomic Nuclei*, 325(3):247–259, 1986.
- [17] H. De Witte et al. Nuclear charge radii of neutron-deficient lead isotopes beyond N=104 midshell investigated by in-source laser spectroscopy. *Physical Review Letters*, 98(11):16–19, 2007.
- [18] M. D. Seliverstov et al. Charge radii and magnetic moments of odd-A $^{183-189}\text{Pb}$ isotopes. *The European Physical Journal A*, 41(3):315–321, 2009.
- [19] T. E. Cocolios et al. Early onset of ground state deformation in neutron deficient polonium isotopes. *Physical Review Letters*, 106(5):1–4, 2011.
- [20] D. A. Fink et al. In-Source Laser Spectroscopy with the Laser Ion Source and Trap: First Direct Study of the Ground-State Properties of $^{217,219}\text{Po}$. *Physical Review X*, 5(1):011018, 2015.
- [21] A. E. Barzakh et al. Changes in mean-squared charge radii and magnetic moments of $^{179-184}\text{Tl}$ measured by in-source laser spectroscopy. *Physical Review C*, 95(1):014324, 2017.
- [22] G. Hagen, T. Papenbrock, M. Hjorth-Jensen, and D. J. Dean. Coupled-cluster computations of atomic nuclei. *Reports on Progress in Physics*, 77:096302, 2014.
- [23] V. Somà, A. Cipollone, C. Barbieri, P. Navrátil, and T. Duguet. Chiral two- and three-nucleon forces along medium-mass isotope chains. *Physical Review C - Nuclear Physics*, 89(6):1–5, 2014.
- [24] R. F. Casten. *Nuclear structure from a simple perspective*. Oxford University Press, second edition, 2005.

- [25] O. Benhar. How much nuclear physics do we need, to understand the neutrino nucleus cross section? *Lectures at the 45th Winter School in Theoretical Physics "Neutrino Interactions: from Theory to Monte Carlo Simulations"*, Ladek-Zdroj, Poland, 2009.
- [26] K. Heyde. *Basic ideas and concepts in nuclear physics: an introductory approach*. CRC Press, third edition, 2004.
- [27] William D Myers and W.J Swiatecki. Average nuclear properties. *Annals of Physics*, 55(3):395–505, 1969.
- [28] C. M. Tarbert et al. Neutron Skin of ^{208}Pb from Coherent Pion Photoproduction. *Physical Review Letters*, 112(24):242502, 2014.
- [29] D. Berdichevsky and F. Tondeur. Nuclear core densities, isotope shifts, and the parametrization of the droplet model. *Zeitschrift für Physik A Atoms and Nuclei*, 322(1):141–147, 1985.
- [30] M. Goeppert Mayer. On Closed Shells in Nuclei. II. *Physical Review*, 75(12):1969–1970, 1949.
- [31] O. Haxel, J. H. D. Jensen, and H. E. Suess. On the “Magic Numbers” in Nuclear Structure. *Physical Review*, 75(11):1766–1766, 1949.
- [32] A. Brown. Lecture notes in nuclear structure physics. *Michigan State University*, 2011.
- [33] S.G. Nilsson. Binding states of individual nucleons in strongly deformed nuclei. *Dan. Mat. Fys. Medd.*, 29(16):1–69, 1955.
- [34] R. B. Firestone. *Table of Isotopes*. Wiley-InterScience, eighth edition, 1996.
- [35] Jacek Dobaczewski. Lectures on density functional theory. *TALENT summer school, York*, 2016.
- [36] Jacek Dobaczewski. private communications. 2017.
- [37] S. Hilaire and M. Girod. The AMEDEV nuclear structure database. *International Conference on Nuclear Data for Science and Technology 2007*, 2008.
- [38] S. Hilaire and M. Girod. Hartree-Fock-Bogolioubov result based on the Gogny force. 23/09/2016.
- [39] K. Heyde and other. A shell-model description of 0^+ intruder states in even-even nuclei. *Nuclear Physics, Section A*, 466(2):189–226, 1987.

- [40] K. Heyde, J. Ryckebusch, M. Waroquier, and J. L. Wood. Intruder states in odd-mass and odd-odd nuclei. *Nuclear Physics A*, 484:275 – 294, 1988.
- [41] K Heyde et al. Equivalence of the spherical and deformed shell-model approach to intruder states. *Physics Letters B*, 218(3):287–290, 1989.
- [42] P. Van Duppen and M. Huyse. Shape coexistence around the Z=82 closed shell probed by α -decay. *Hyperfine Interactions*, 129(1):149–161, 2000.
- [43] J. O. Rasmussen. Alpha-decay barrier penetrabilities with an exponential nuclear potential: even-even nuclei. *Physical Review*, 42(6), 1959.
- [44] M. Göppert-Mayer. Über die Wahrscheinlichkeit des Zusammenwirkens zweier Lichtquanten in einem Elementarakt. *Die Naturwissenschaften*, 17(48):932, 1929.
- [45] M. Göppert-Mayer. Über Elementarakte mit zwei Quantensprüngen. *Annalen der Physik*, 401(3):273–294, 1931.
- [46] J. C. Jaeger and H. R. Hulme. On the Production of Electron Pairs. *Proceedings of the Royal Society of London. Series A, Mathematical and Physical Sciences*, 153(879):443–447, 1936.
- [47] P. Campbell, I. D. Moore, and M. R. Pearson. Laser spectroscopy for nuclear structure physics. *Progress in Particle and Nuclear Physics*, 86:127–180, 2016.
- [48] B. Cheal and K. T. Flanagan. Progress in laser spectroscopy at radioactive ion beam facilities. *Journal of Physics G: Nuclear and Particle Physics*, 37(11):113101, 2010.
- [49] W. H. King. *Isotope Shifts in Atomic Spectra*. Plenum, New York, 1984.
- [50] B. Cheal, T. E. Cocolios, and S. Fritzsche. Laser spectroscopy of radioactive isotopes: Role and limitations of accurate isotope-shift calculations. *Physical Review A - Atomic, Molecular, and Optical Physics*, 86(4):042501, 2012.
- [51] E. W. Otten. Nuclear Radii and Moments of Unstable Isotopes. In D. A. Bromley, editor, *Treatise on Heavy Ion Science*, chapter 7, pages 517–638. Springer US, Boston, MA, 1 edition, 1989.
- [52] Cern website: Accelerators and Technology Sector (<https://espace.cern.ch/acc-tec-sector/default.aspx>). 01/09/2016.

- [53] D. G. Jenkins. Recent advances in nuclear physics through on-line isotope separation. *Nature Physics*, 10(12):909—913, 2014.
- [54] M. J. G. Borge. Highlights of the ISOLDE facility and the HIE-ISOLDE project. *Nuclear Instruments and Methods in Physics Research Section B: Beam Interactions with Materials and Atoms*, 376:408 – 412, 2016.
- [55] ISOLDE facility website (<http://isolde.web.cern.ch>). 01/09/2016.
- [56] B. A. Marsh et al. New developments of the in-source spectroscopy method at RILIS/ ISOLDE. *Nuclear Instruments and Methods in Physics Research, Section B: Beam Interactions with Materials and Atoms*, 317(PART B):550–556, 2013.
- [57] E. Kugler. The ISOLDE facility. *Hyperfine Interactions*, 129(1):23–42, 2000.
- [58] G. J. Russell. Spallation Physics - An Overview. *International Collaboration on Advanced Neutron Sources KEK. Tsukuba*, pages 291–299, 1990.
- [59] S. Rothe et al. Laser ion beam production at CERN-ISOLDE: New features - More possibilities. *Nuclear Instruments and Methods in Physics Research, Section B: Beam Interactions with Materials and Atoms*, 376:91–96, 2015.
- [60] T. Day Goodacre et al. Laser ionized ion beams of Li^+ , Ba^+ and Ba^{++} using the ISOLDE-RILIS. *unpublished results*.
- [61] S. Rothe et al. Measurement of the first ionization potential of astatine by laser ionization spectroscopy. *Nature communications*, 4(May):1835, 2013.
- [62] I. Asimov. The natural occurrence of short-lived radioisotopes. *Journal of Chemical Education*, 30(12):616, 1953.
- [63] A. Kramida, Yu. Ralchenko, J. Reader, and and NIST ASD Team. NIST Atomic Spectra Database (ver. 5.3), (<http://physics.nist.gov/asd>). National Institute of Standards and Technology, Gaithersburg, MD., 17/04/2017.
- [64] B. Lommel et al. Improvement of the target durability for heavy-element production. *Nuclear Instruments and Methods in Physics Research Section A: Accelerators, Spectrometers, Detectors and Associated Equipment*, 480(1):16 – 21, 2002.
- [65] X-ray instruments Associates (<http://www.xia.com>). <http://www.xia.com>, 02/09/2016.

- [66] IGOR software package from wavemetrics (<https://www.wavemetrics.com/>). <https://www.wavemetrics.com/>, 19/09/2016.
- [67] S. Rothe et al. Narrow linewidth operation of the RILIS titanium: Sapphire laser at ISOLDE/CERN. *Nuclear Instruments and Methods in Physics Research Section B: Beam Interactions with Materials and Atoms*, 317:561–564, 2013.
- [68] R. N. Wolf et al. A multi-reflection time-of-flight mass separator for isobaric purification of radioactive ion beams. *Hyperfine Interactions*, 199(1-3):115–122, 2011.
- [69] R. N. Wolf et al. ISOLTRAP's multi-reflection time-of-flight mass separator/spectrometer. *International Journal of Mass Spectrometry*, 349-350(1):123–133, 2013.
- [70] R. D. Page et al. Radioactivity of neutron deficient isotopes in the region $N > 82 > Z$. *Physical Review C*, 53(2):660–670, 1996.
- [71] M. Mukherjee et al. ISOLTRAP: An on-line Penning trap for mass spectrometry on short-lived nuclides. *The European Physical Journal A*, 35(1):1–29, 2008.
- [72] J. G. Cubiss et al. In preparation for PLB.
- [73] A. Rytz. Recommended energy and intensity values of alpha particles from radioactive decay. *Atomic Data and Nuclear Data Tables*, 47(2):205–239, 1991.
- [74] M. Huyse et al. Isomers in three doubly odd Fr-At-Bi α -decay chains. *Physical Review C*, 46(4):1209–1217, 1992.
- [75] T. Enqvist et al. Alpha decay properties of $^{200-202}\text{Fr}$. *Zeitschrift für Physik A: Hadrons and Nuclei*, 354(1):1–2, 1996.
- [76] J. Uusitalo et al. α Decay Studies of Very Neutron-Deficient Francium and Radium Isotopes. *Physical Review C - Nuclear Physics*, 71(2):1–9, 2005.
- [77] J. E. Gaiser. Charmonium spectroscopy from radiative decays of the j/ψ and ψ -prime. *Ph.D. Thesis, SLAC-R-255*, 1982.
- [78] M. J. Oreglia. A study of the reactions ψ prime \rightarrow gamma gamma ψ . *Ph.D. Thesis, SLAC-R-236*, 1980.
- [79] T. Skwarnicki. A study of the radiative cascade transitions between the ψ -prime and ψ resonances. *Ph.D Thesis, DESY F31-86-02*, 1986.

- [80] Y. A. Akovali. Review of Alpha-Decay Data from Doubly-Even Nuclei. *Nuclear Data Sheets*, 84(1):1–114, 1998.
- [81] A. N. Andreyev et al. Decay of the $9/2^-$ isomer in ^{181}Tl and mass determination of low-lying states in ^{181}Tl , ^{177}Au , and ^{173}Ir . *Physical Review C - Nuclear Physics*, 80(2):1–8, 2009.
- [82] M. Venhart et al. Shape coexistence in odd-mass Au isotopes: Determination of the excitation energy of the lowest intruder state in ^{179}Au . *Physics Letters, Section B: Nuclear, Elementary Particle and High-Energy Physics*, 695(1-4):82–87, 2011.
- [83] A. N. Andreyev. JR121 experiment, JYFL. 2015.
- [84] H. J. Li et al. Recoil-decay tagging spectroscopy of $^{162}_{74}\text{W}_{88}$. *Physical Review C*, 92(1):014326, 2015.
- [85] M. Leino et al. Gas-filled recoil separator for studies of heavy elements. *Nuclear Instruments and Methods in Physics Research Section B: Beam Interactions with Materials and Atoms*, 99(1-4):653–656, 1995.
- [86] R. D. Page et al. The GREAT spectrometer. *Nuclear Instruments and Methods in Physics Research Section B: Beam Interactions with Materials and Atoms*, 204:634–637, 2003.
- [87] K.-H. Schmidt et al. Gamma-Spectroscopic investigations in the radiative fusion reaction $^{90}\text{Zr} + ^{90}\text{Zr}$. *Physics Letters B*, 168(1-2):39–42, 1986.
- [88] T. Kibédi et al. Evaluation of theoretical conversion coefficients using BrIcc. *Nuclear Instruments and Methods in Physics Research, Section A: Accelerators, Spectrometers, Detectors and Associated Equipment*, 589(2):202–229, 2008.
- [89] S. Agostinelli et al. GEANT4 - A simulation toolkit. *Nuclear Instruments and Methods in Physics Research, Section A: Accelerators, Spectrometers, Detectors and Associated Equipment*, 506(3):250–303, 2003.
- [90] J. Allison et al. Geant4 developments and applications. *IEEE Transactions on Nuclear Science*, 53(1):270–278, 2006.
- [91] E. Browne. Nuclear Data Sheets Update for $A = 178$. *Nuclear Data Sheets*, 72(2):221–296, 1994.

- [92] E. F. Zganjar. Conversion electron spectroscopy and its role in identifying shape coexisting structures in nuclei via E0 transitions. *Journal of Physics G: Nuclear and Particle Physics*, 43(2):024013, 2016.
- [93] C. J. Gallagher and S. A. Moszkowski. Coupling of Angular Momenta in Odd-Odd Nuclei. *Physical Review*, 111(5):1282–1290, 1958.
- [94] A. N. Andreyev et al. α decay of ^{176}Au . *Physical Review C*, 90(4):044312, 2014.
- [95] H. Kettunen et al. Investigations into the alpha-decay of ^{195}At . *European Physical Journal A*, 16(4):457–467, 2003.
- [96] H. Kettunen et al. Alpha-decay studies of the new isotopes ^{191}At and ^{193}At . *European Physical Journal A*, 17(4):537–558, 2003.
- [97] A. N. Andreyev et al. α -decay spectroscopy of the new isotope ^{192}At . *Physical Review C*, 73(2):024317, 2006.
- [98] A. N. Andreyev et al. α -decay of ^{194}At . *Physical Review C*, 79(6):064320, 2009.
- [99] K. Auranen et al. Experimental study of $1/2^+$ isomers in $^{199,201}\text{At}$. *Physical Review C*, 90(2):024310, 2014.
- [100] V. L. Truesdale et al. β -delayed fission and α decay of ^{196}At . *Physical Review C*, 94(3):034308, 2016.
- [101] P. A. Butler and W. Nazarewicz. Intrinsic reflection asymmetry in atomic nuclei. *Reviews of Modern Physics*, 68(2):349–421, 1996.
- [102] T. E. Cocolios et al. The Collinear Resonance Ionization Spectroscopy (CRIS) experimental setup at CERN-ISOLDE. *Nuclear Instruments and Methods in Physics Research Section B: Beam Interactions with Materials and Atoms*, 317(PART B):565–569, 2013.
- [103] W. Treytl and K. Valli. Alpha decay of neutron deficient astatine isotopes. *Nuclear Physics A*, 97(2):405–416, 1967.
- [104] M. B. Smith et al. Isomeric state in the doubly odd ^{196}At nucleus. *Journal of Physics G: Nuclear and Particle Physics*, 26:787, 2000.
- [105] M. B. Smith et al. First observation of excited states in ^{197}At : the onset of deformation in neutron-deficient astatine nuclei. *European Physical Journal A*, 47:43–47, 1999.

- [106] E. Coenen et al. First identification of a $1/2^+$ intruder state in the ^{197}At isotope. *Zeitschrift für Physik A Atomic Nuclei*, 324(4):485–486, 1986.
- [107] A. Rytz. Catalogue of recommended alpha energy and intensity values. *Atomic Data and Nuclear Data Tables*, 12(5):479–498, 1973.
- [108] G. Bastin and C. F. Liang. Spectres α d’isotopes d’astate deficientes en neutrons produits et separees en ligne. Technical report, 1975.
- [109] U. Jakobsson et al. Spectroscopy of the proton drip-line nucleus ^{203}Fr . *Physical Review C - Nuclear Physics*, 87(5):1–9, 2013.
- [110] S. S. Penner. *Quantitative molecular spectroscopy and gas emissivities*. Addison-Wesley Pub. Co., second edition, 1959.
- [111] B. Cheal, T. E. Cocolios, and S. Fritzsche. Laser spectroscopy of radioactive isotopes: Role and limitations of accurate isotope-shift calculations. *Physical Review A*, 86(4):042501, 2012.
- [112] W. D. Myers and K. H. Schmidt. An update on droplet-model charge distributions. *Nuclear Physics, Section A*, 410(1):61–73, 1983.
- [113] L. Grodzins. The uniform behaviour of electric quadrupole transition probabilities from first 2^+ states in even-even nuclei. *Physics Letters*, 2(2):88–91, 1962.
- [114] S. Raman, C. W. Nestor, and P. Tikkanen. Transition probability from the ground to the first-excited 2^+ state of even-even nuclides. *Atomic Data and Nuclear Data Tables*, 78(1):1–128, 2001.
- [115] M. Anselment et al. The odd-even staggering of the nuclear charge radii of Pb isotopes. *Nuclear Physics A*, 451(3):471–480, 1986.
- [116] U. Dinger et al. Nuclear moments and change in the charge-radii of neutron deficient lead isotopes. *Zeitschrift für Physik A Atomic Nuclei*, 328(2):253–254, 1987.
- [117] S. B. Dutta et al. Measurement of isotope shift and hyperfine splitting of $^{190,191,193,197}\text{Pb}$ isotopes by collinear laser spectroscopy. *Zeitschrift für Physik A Hadrons and Nuclei*, 341(1):39–45, 1991.
- [118] A. Coc et al. Isotope shifts, spins and hyperfine structures of $^{118,146}\text{Cs}$ and of some francium isotopes. *Nuclear Physics, Section A*, 468(1):1–10, 1987.

- [119] I. Budinčević et al. Laser spectroscopy of francium isotopes at the borders of the region of reflection asymmetry. *Physical Review C*, 90(1):014317, 2014.
- [120] K. M. Lynch et al. Decay-Assisted Laser Spectroscopy of Neutron-Deficient Francium. *Physical Review X*, 4(1):011055, 2014.
- [121] W. Borchers et al. Hyperfine structure and isotope shift investigations in $^{202-222}\text{Rn}$ for the study of nuclear structure beyond $Z=82$. *Hyperfine Interactions*, 34(1-4):25–29, 1987.
- [122] S. A. Ahmad et al. Mean square charge radii of radium isotopes and octupole deformation in the $^{220-228}\text{Ra}$ region. *Nuclear Physics A*, 483(2):244–268, 1988.
- [123] G. D. Alkhazov et al. Odd-even staggering in nuclear charge radii of neutron-rich europium isotopes. *Zeitschrift für Physik A Atomic Nuclei*, 337(3):257–259, 1990.
- [124] J. Dobaczewski and J. Engel. Nuclear time-reversal violation and the schiff moment of ^{225}Ra . *Physical Review Letters*, 94(23):1–4, 2005.
- [125] Th. Schmidt. Über die magnetischen Momente der Atomkerne. *Zeitschrift für Physik*, 106(5-6):358–361, 1937.
- [126] A. Arima. A short history of nuclear magnetic moments and GT transitions. *Science China Physics, Mechanics and Astronomy*, 54(2):188–193, 2011.
- [127] C. Ekström, G. Wannberg, and Y. S. Shishodia. Hyperfine structure and nuclear magnetic moments of some neutron-deficient thallium isotopes. *Hyperfine Interactions*, 1(1):437–458, 1975.
- [128] H. Ingwersen et al. Nuclear g factors of the $21/2^-$ and the $29/2^+$ states in ^{211}At . *Physical Review C*, 11(1):243–252, 1975.
- [129] Y. Ting and D. Williams. Nuclear Gyromagnetic Ratios. IV. *Physical Review*, 89(3):595–596, 1953.
- [130] A. Arima and H. Horie. Configuration Mixing and Magnetic Moments of Odd Nuclei. *Progress of Theoretical Physics*, 12(5):623–641, 1954.
- [131] M. R. Pearson et al. Nuclear moments and charge radii of bismuth isotopes. *Journal of Physics G: Nuclear and Particle Physics*, 26(12):1829–1848, 2000.
- [132] A. E. Barzakh et al. Laser spectroscopy studies of intruder states in $^{193,195,197}\text{Bi}$. *Physical Review C*, 94(2):024334, 2016.

- [133] A. B. Barzakh. private communications. 2017.
- [134] J. A. Bounds et al. Nuclear structure of light thallium isotopes as deduced from laser spectroscopy on a fast atom beam. *Physical Review C*, 36(6):2560–2568, 1987.
- [135] R. Menges et al. Nuclear moments and the change in the mean square charge radius of neutron deficient thallium isotopes. *Zeitschrift für Physik A Hadrons and Nuclei*, 341(4):475–479, 1992.
- [136] H. A. Schuessler et al. Nuclear moments of the neutron-deficient thallium isotopes. *Hyperfine Interactions*, 74(1-4):13–21, 1992.
- [137] A. E. Barzakh et al. Changes in the mean-square charge radii and magnetic moments of neutron-deficient Tl isotopes. *Physical Review C - Nuclear Physics*, 88(2):1–10, 2013.
- [138] C. Van Beveren et al. α -decay study of $^{182,184}\text{Tl}$. *Journal of Physics G: Nuclear and Particle Physics*, 43(2):025102, 2016.
- [139] R. Heinke et al. High-resolution in-source laser spectroscopy in perpendicular geometry. *Hyperfine Interactions*, 238(1):6, 2017.